DEVELOPMENT OF ELECTROOSMOTIC SAMPLING FOR THE INVESTIGATION OF GALANIN-DEGRADING ECTOPEPTIDASE ACTIVITY IN THE HIPPOCAMPUS

by

Amy Elisabeth Rupert

B.S. Chemistry, Indiana University of Pennsylvania, 2006

Submitted to the Graduate Faculty of

The Kenneth P. Dietrich School of Arts and Sciences

in partial fulfillment of the requirements for the degree of

Doctor of Philosophy

University of Pittsburgh

2012

UNIVERSITY OF PITTSBURGH

DIETRICH SCHOOL OF ARTS AND SCIENCES

This dissertation was presented

by

Amy Elisabeth Rupert

It was defended on

October 5, 2012

and approved by

Adrian C. Michael, Professor, Chemistry Department

Renã Robinson, Professor, Chemistry Department

Mats Sandberg, Professor, Institute of Biomedicine, Gothenberg University, Sweden

Dissertation Advisor: Stephen G. Weber, Professor, Chemistry Department

DEVELOPMENT OF ELECTROOSMOTIC SAMPLING FOR THE INVESTIGATION OF GALANIN-DEGRADING ECTOPEPTIDASE ACTIVITY IN THE HIPPOCAMPUS

Amy Elisabeth Rupert, PhD

University of Pittsburgh, 2012

There are currently no methods that have been successfully used to sample the extracellular component of brain slice preparations with the precision developed for *in vivo* sampling methods. We developed a slice-compatible method that removes fluid by electroosmosis. Two designs were investigated: one utilizing a single capillary where flow originates below the tissue and fluid pulled upwards and one using two capillaries where flow is between the two capillary lumens. The two-capillary approach is analogous to push-pull perfusion wherein a source 'push' capillary with a tapered tip is inserted into the tissue and a collection 'pull' capillary is positioned at the surface in close proximity to the source capillary. Voltage is applied across proximal capillary ends, which invoked fluid flow from source capillary into the tissue then to the collection capillary. Damage studies addressed minimization of perturbation of tissue by electric fields in both single and push-pull models. Flow rates were quantified for the two-capillary model using HPLC analysis of collected fluid. Numerical simulations aided understanding of electric field distribution and fluid flow within the tissue.

We then investigated the hydrolysis of exogenous galanin in the extracellular space after ischemic pre-conditioning, a method in which mild, short ischemia creates resistance in the brain against a longer duration of ischemia 24-48 hours later. The efficacy of many neuropeptides, including galanin, is controlled by hydrolysis of active peptide into smaller active and inactive fragments by ectopeptidases. We used push-pull electroosmotic sampling and MALDI mass spectrometry to identify hydrolysis products created after passing exogenous galanin through tissue. We then quantified the hydrolysis of galanin after ischemic pre-conditioning. We showed that pre-conditioned cultures have decreased galanin

hydrolysis in the CA1 and DG areas, but not the CA3. Finally, we treated cultures with inhibitors for metallo- and aminopeptidases and quantified the resulting relative changes in galanin hydrolysis. Results indicate that metallopeptidases, particularly those that use zinc, are likely responsible for galanin degradation in the CA1 region of the hippocampus. Neuron specific aminopeptidase may also be hydrolyzing galanin. The distribution of hydrolysis products determined with MALDI-MS also indicate aminopeptidase activity.

TABLE OF CONTENTS

LIST OF TABLES

LIST OF FIGURES

1.0 INTRODUCTION

The brain is a complex organ, relying on hundreds of types of neurotransmitters and receptors to transduce chemical signal into action and function – the arrival of these signaling molecules at their target cell are responsible for everything from large muscle movement to the timing of the release of hormones. Signaling can be synaptic, or 'wired' or through volume transmission. In wired transmission, chemical messengers affect receptors within the synapse. They are released pre-synaptically and travel a very short distance to bind to receptors on the post-synaptic terminal. This mode of transmission was considered the primary mode in which neuronal signaling is carried out, however, it is now known that molecules often leave the synaptic cleft or are released directly in the extracellular space and diffuse to their target cell to create a response. Thus, this extracellular component of the brain holds important chemical information, if it is accessible to analysis. Developing sampling methods to remove extracellular fluid began in the 1960s with push-pull perfusion[1] followed by the development of microdialysis in the 1980s[2]. Currently, these two methods are the most prominently used for sampling the extracellular space of living tissue.

1.1 MICRODIALYSIS, PUSH-PULL PERFUSION, AND DIRECT SAMPLING

The push-pull perfusion probe is composed of two cannulae, which are inserted into the tissue to be sampled. The cannulae are either connected by outer tubing in a side-by-side fashion or concentrically with a smaller cannula nestled inside a bigger cannula. Perfusion fluid (usually a buffer of physiological pH) is pushed through one cannula into the tissue and a negative pressure applied to a second cannula recovers the perfusate, along with some extracellular fluid. The first versions of push-pull perfusion used flow rates on the order of 200 μL/min and were constructed

in large needles for ease of insertion into the brain. These models suffered from blockage of the pull cannula by dislodged tissue, likely from the force of perfusate flow. This pressure also caused substantial damage to the tissue. The first improvement on push-pull perfusion came in 1977[3] with the addition of a pressure control and monitoring of the pull line. This decreased incidence of clogs allowed for slower flow rates of 0.6 – 1.7 μL/min to be used without detriment to clog detection. In turn, lower flow rates caused less damage, both by minimizing mechanical force and minimizing loss of fluid due to imbalance between the push and pull flow rates. Additionally, probe size decreased, using a 23-gauge (640 μm) needle for construction. However, the physical damage from mechanical motion of fluid against sensitive cells was still substantial[3, 4].

The first dialysis probe was invented by covering the end of the push-pull probe with a semi-permeable membrane[5, 6]. Fluid moved through one cannula and was collected into the other but only through a push mechanism and had no direct contact with the extracellular space. Molecules in the extracellular space diffused through the membrane into the dialysate to be collected. The size of the dialysis probe was similar to the push-pull perfusion probe.

For two decades, push-pull perfusion was mostly forgotten with the exception of a few reductions in probe size and flow rate[7, 8]. Major efforts were placed on improving the dialysis method. Construction transitioned from using needles to capillary probes with outer diameters ranging from 150 to 500 μm, giving the method its now used name, microdialysis[2]. With the use of stereotaxic surgery, microdialysis allowed reproducible sampling of any brain region and rapidly became useful for sampling in live animals[9]. There are several microdialysis designs, depending on the tissue to be sampled; typically the cylindrical probe is used for brain, consisting of two concentric cannulae 15 mm long with membrane at the end 1-4 mm in length[10]. Paradoxically, the semi-porous membrane proved the biggest weakness of microdialysis when compared to push-pull perfusion. Collection of analyte relies on diffusion through the membrane so flow rates must be decreased to increase recovery of analyte in the dialysate. Typically, 20-30 minutes of collection was required to obtain 20-30 μL of sample[11]. When using microdialysis to detect neurochemical changes that often occur on second time scales, this is quite poor time resolution. Recovery rates are typically measured by sampling a solution of known concentration is defined as the percent recovered in the probe compared to that known concentration. Recovery rates depend highly on analyte size, charge, hydrophobicity, and concentration in the

extracellular space but calibration of the probe makes quantification of extracellular concentrations possible[12-14]. Microdialysis models of the 1990's and early 2000's could be routinely used for collection of small analytes such as amino acids and monoamine neurotransmitters[15-17], however, microdialysis membranes available at that time typically had a 30 kDa molecular weight cut off (MWCO)[18] and were incompatible with larger peptides and protein collection at a time when the analysis of peptides and proteins was becoming prevalent. Push-pull perfusion had better recovery rates than microdialysis even for small analytes [19] and became the preferred method for larger neuropeptide collection. Additionally, directly sampling the extracellular space is tremendously advantageous for low concentration analytes.

In 2002, Shippy at the University of Illinois revisited and revamped the push-pull technique with emphasis on reducing damage caused by high flow rates[20]. Be redesigning the concentrically arranged probe to flow from the outer tube to the inner tube and using a 27 gauge (410 μm) needle, flow rates could be dropped to 1-10 μL/minute reducing tissue damage. This low-flow push-pull perfusion method achieved recovery rates of 70-80% when collecting glutamate from the rat striatum *in vivo*. This group was able to further use this method to study amino acids at the vitreoretinal interface[21], which would have been difficult with the microdialysis probe, as well as monitor glutamate in freely-moving animals during feeding[22]. Coupled to online CE analysis, glutamate was measured at 11.5-second time resolution with a calculated spatial resolution of 0.023 mm^2. Nitrate levels were analyzed in the eye with 46-71% recovery rates compared to 12-16% in similar microdialysis experiments[23].

In 2002, Kennedy briefly pursued the direct sampling method[12]. This method utilized the 'pull' component of push-pull without the 'push'. The sampling probes were 90 μm wide and utilized a flow rate of 1-50 nL/min to sample monoamine neurotransmitters. An important realization of this study was that higher removal rates (>10 nL/min) depleted the analyte in the sampling zone faster than it could be replenished. A 90 second time resolution of fluctuating levels of glutamate and aspartate with application of potassium was achieved. Most notably, direct sampling had a 500-fold better spatial resolution than microdialysis of amino acids and was on par with the soon-to-be realized improvements on push-pull perfusion.

In the mid 2000s, improvements to microdialysis focused on improving recovery rates of large molecules, peptides and proteins. One solution involved putting affinity agents in the perfusate, such as cyclodextrins or antibodies in order to make transport across the membrane

more thermodynamically favorable[24]. In 2008, cyclodextrins were included in the perfusate and improved recovery of enkephalins 1.5-1.8 fold[25]. In 2009, heparin was included in the dialysate to increase recoveries of cytokines[26]. Another way to increase recovery is to use membranes with larger pore sizes, such as 100 kDa. However, one major drawback of larger pores is fluid loss from the microdialysis probe[7, 18], which can be partially remedied by the addition of osmotic agents such as bovine serum albumin[8]. Roy, et al., utilizing the idea of larger pores, fabricated a new microdialysis design using a 1000 kDa MWCO membrane[27]. Instead of the traditional push-only mechanism of fluid flow, Roy employed the push-pull mechanism to minimize the negative pressure on the membrane and inserted a spring in the microdialysis tip to keep the rigid structure of the membrane. With less negative pressure on the membrane, fluid loss was minimized, and larger molecules could freely diffuse through the larger pores of the membrane. Larger pores allowed for higher flow rates and greater recovery rates. Recovery rates of Leu-enkephalin, vasopressin (1 kDa), bovine serum albumin (66.5 kDa), and ovalbumin (45 kDa) were nearly 100%.

This push-pull variation of microdialysis suffered similar pressure control problems as the initial push-pull probe. Similar to the 1977 study, a vent was incorporated into the pull line adjusting the pressure to maintain constant flow[28]. This tweaked design collected 38-43-amino acid peptides produced from amyloid precursor protein cleaved by β- and γ-secretases. Recoveries of αβ1-40 (4 kDa) increased from <2% with a 50 kDa MWCO membrane to almost 20% using a 100-kDa membrane and from 11% to 26% of IL-6 (26 kDa) using a 1000 kDa MWCO membrane.

One of the most significant improvements in both microdialysis and push-pull perfusion in the last decade is the transport of sample from the probe to the detector by [10]segmented flow. Small plugs of aqueous sample (5-30 nL) are sandwiched between plugs of oil, preventing mixing and minimizing Taylor dispersion of sample before detection[29]. In this way, analytes remain concentrated in each plug and retain temporal resolution even when using low flow rates to maximize sample recovery across the microdialysis membrane. Low-flow push-pull perfusion probes routinely used by the Kennedy lab today are constructed in 27 gauge needles (140 μm) with an estimated 0.016 mm^2 spatial resolution[30]. Flow rates are 10-50 nL/min. Temporal resolution depend highly on the analyte and detection method, but when using segmented flow after collection, samples of L-glutamate were able to be collected every 7 seconds[30]. Low Flow

push-pull perfusion recoveries are 100%[10]. Direct sampling of l-glutamate, using just the 'pull' aspect of push-pull perfusion, have achieved 200 ms temporal resolution[30]. Microdialysis uses probes of similar size to push-pull perfusion, perfusing at a rate of 0.3-5 μL/min[31]. Typically, samples are typically collected anywhere from 1-20 minutes when using HPLC as the detection method, however segmented flow and coupling to CE and sensors have allowed samples to be collected in seconds[29, 32-34]. Most traditional membranes are 20-60 kDa MWCO[10] and 1-4 mm in length. The size of the membrane influences spatial resolution, as the area sampled is at least the size of the membrane, if not bigger. However, surprisingly, it was also found to influence the temporal resolution, as decreasing the membrane size also decreased response time to changed analyte concentrations at the probe membrane[29]. Microdialysis recoveries are dependent on analyte and membrane characteristics. For small molecules, for example exogenously applied cocaine, using 20-60 MWCO membranes with a flow rate of 0.5 – 2 μL/min, recoveries are 10-40%, but this can be increased to nearly 100% if a flow rate of 100 nL/min is used[35].

Efforts are still ongoing to decrease probe size, moving recently to micro fabrication to further decrease probe size and exploring construction of microdialysis probes with smaller membranes (0.5 mm)[32]. With the development of segmented flow allowing incredibly low flow rates, the temporal resolution and small molecule analyte recoveries are similar between microdialysis and push-pull perfusion in 2012. Spatial resolution is the primary aspect in which push-pull perfusion is superior to microdialysis, due to the membrane size. However, some argue that the membrane is a critical barrier to maintain a clean sample, as required by many detection methods. Push-pull perfusion is also easier to use for peptides and protein studies, but that will likely change with continued development of high MWCO microdialysis probes.

1.2 SAMPLING *IN VITRO*

The hippocampus, part of the limbic system, is one of the more structurally distinct and identifiable structures of the brain. Its internal structure is likewise distinct, with a laminar structure that is visible even to the naked eye. The *in vitro* organotypic preparation of the hippocampus, developed in 1991 by Stoppini [36], can be kept viable for up to 2 months. It retains

most of the structural characteristics and neurocircuitry, developing similarly to its *in vivo* counterpart, with the exception of a few afferents to other brain regions[37, 38]. The hippocampus is involved in a multitude of neuronal functions and thus has become a popular route for studying mechanisms of neurogenesis[39, 40], synaptic plasticity[38, 41], neurotoxicity[42-44], stroke/ischemia[45-47], and neuroprotection and repair[48-50]. The interface organotypic hippocampal slice culture (OHSC) is prepared by culturing septotemporally-sliced cross-sections of an immature post-natal rat hippocampus (post-natal 5 days to 9 days (p5-p9)). OHSC studies are directly relevant to *in vivo* developmentally, but also lend greater accessibility and easier manipulation when compared to the live animal model.

Despite routine use of the OHSC model in the laboratory, techniques for sampling the extracellular space of slice-type samples are limited. Microdialysis was designed to extract extracellular components from whole brain samples and the probe size proves incompatible with use in an OHSC, which is only 150 μm thick and 2 mm wide. One approach frequently utilized in tissue slice analysis is to simply submerge the tissue in solution and collect that solution for analysis. This method has poor spatial resolution and dilutes analytes, often in very small concentrations in the brain. Around the time that the OHSC preparation method was in development, the use of micropipettes to simply touch the surface of the tissue, drawing up any liquid on the surface by capillary action was explored[51] but never caught on. A research group from Yale modified the microdialysis probe in 1991 such that the porous membrane lay across the surface of a tissue slice instead of perpendicular insertion[52]. However, *in vitro* microdialysis has not been used since, and even with the improvements of the *in vivo* technique. An ideal method for sampling small tissue samples like the OHSC would have very small collection probes for enhanced spatial resolution and employ very small flow rates to minimize tissue disturbance and replenish removed extracellular fluid. A major source of damage is the insertion of the probes into tissue, so miniaturization of inserted probes would improve this aspect of sampling, particularly when the cultures are quite small themselves. Push-pull perfusion and DS, while developed for *in vivo* use, show the most promise for application in smaller samples such as the slice culture as they possess the needed spatial resolution for the heterogeneity of the OHSC. However, push-pull perfusion is more advantageous than DS as the mechanics of DS will deplete the small volume of extracellular fluid over time. The push-pull design also allows for introduction of material into the sample space. To improve upon the push-pull design, it may

also be helpful to have more control over the spatial resolution simply by changing placement of the push and pull cannulae with respect to each other. Low-flow push-pull perfusion is a starting point for which we develop a new technique based on electroosmotic rather than pressure-driven flow. This technique achieves flow rates much less than 50 nL/min, and the area sampled can be limited to a single structural region in the hippocampus through separate placement of push and pull probes. In one sampling design, we have altogether negated the need to insert any probe into the tissue eliminating penetration injury. In a second design, we miniaturize the inserted capillary to 30 μm, which results in no detectable penetration injury.

1.3 ELECTROOSMOTIC SAMPLING

1.3.1 Electroosmosis

Applying electric potential across a porous material, capillary tube, micro-channel or any other fluid conduit with charged walls creates bulk fluid movement known as electroosmotic flow. This phenomenon is illustrated in Figure 1.

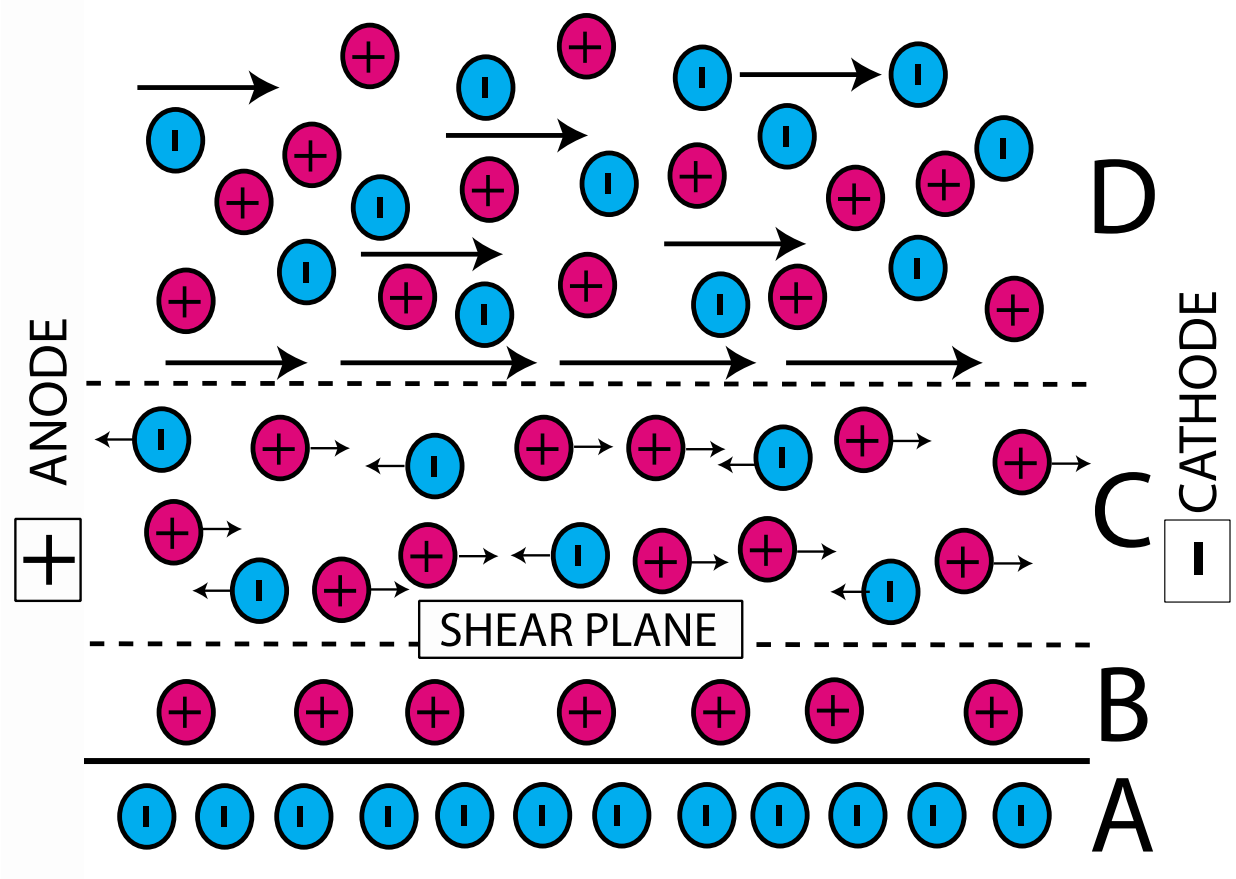

Figure 1. Electroosmosis in a fused-silica capillary

This phenomenon occurs in any small space that has charged walls through the existence of four layers. Figure 1 above shows an electrolyte (positive ions pink, negative ions blue) next to a capillary wall. Only one wall is shown. (A) is the stationary layer of charges on the capillary wall. On the wall, a stationary layer of counterions (B) builds up. Further from the wall, a more diffuse layer of counter ions forms (C). This layer has a net charge and moves according to an applied electric field. The stationary layer (B) and the diffuse layer (C) are divided by the shear plane where mobile charges move against stationary and create electrochemical potential, called the zeta potential (ζ). At the center of the capillary is the bulk solution (D), which is electrochemically neutral. However, due to the moving diffuse layer, this layer will move as well, creating what is known as electroosmotic flow.

The chemical equilibrium between a charged surface and an electrolyte results in a net fixed layer of counter ions on the wall followed by a layer of more diffuse mobile counter ions. This mobile portion of the double layer will move in an electric field according to the Coulomb force induced upon it. This creates bulk movement in the electrochemically neutral bulk fluid in the center of the capillary, with the overall flow phenomenon of electroosmotic flow. The speed

of this flow is dictated by the potential difference, or zeta potential (ζ), between the mobile and static components of the double layer. A greater ζ corresponds to a higher concentration of counter ions in the diffuse layer, and thus electroosmotic flow will be faster. Electroosmosis has a plug flow profile, in contrast to parabolic profile induced by pressure-driven flow, such as in microdialysis and push-pull perfusion. In terms of sampling, plug flow is advantageous because it creates less Taylor dispersion, preserving temporal resolution of the sample to a greater extent. Furthermore, since only an electric field is required for Electroosmotic flow, pumps, valves and other bulky equipment is not necessary. The OHSC is porous, with the walls of the extracellular space composed of the external surface of cell membranes. The charged wall and, consequently, a ζ-potential arise from surface functional groups, such as proteins, carbohydrates, and phospholipids. We have shown that electroosmotic flow can be induced in the OHSC and calculated a ζ–potential of the OHSC as -22.4 mV[53]. It is thus possible to harness this ability to move extracellular fluid for collection.

A sample of extracellular fluid can be collected by arranging a fused-silica capillary (ζ = -50 mV) in direct contact with the tissue and applying a potential across the tissue-capillary interface. Electroosmotic flow requires no pressure. Thus, damage seen in push-pull perfusion caused by external pressure exerted on fragile tissue is eliminated (though considerations should be and were made for the effects of an electric field on the tissue). Replacement of removed extracellular fluid was accomplished by placing the ground electrode in a source of electrolyte in contact with the tissue (i.e. situating the tissue over a buffer bath), drawing this fluid into the tissue as electroosmotic flow draws fluid out[54]. This method was used to study the kinetics of peptidases in the extracellular space by putting a peptide in the buffer bath fluid and drawing it up into the tissue then into the capillary for HPLC analysis. This illustrated usability of electroosmosis for the driving force behind sampling. However, spatial resolution was poor and introduction of material into the tissue by putting it into the bath solution is inefficient, particularly if the material is expensive.

In a more refined electroosmotic sampling designed inspired by push-pull perfusion, ground is applied to the non-tissue end of the ‘push’ segment and a potential to the non-tissue end of the ‘pull’ segment, creating the same fluid movement as in push-pull perfusion, but driven by electroosmosis. The ‘push’ source probe was a capillary pulled to a small tip (15-30 μm), and was inserted into the tissue, but created no penetration damage. The ‘pull’ collection capillary sat

at the tissue surface nearby. One advantage of push-pull electroosmotic sampling is that electroosmotic flow is maintained in the tissue *between* pull and push probes, which does not occur in traditional push-pull perfusion. Thus, push-pull electroosmotic sampling is more versatile and flow is more definable. First, the two probes can be placed further apart as flow is by the electric field maintained between the two probes in the tissue. Collection efficiencies are based on contributions of diffusion and electrokinetics to the flow from one probe to the other and the spatial resolution of push-pull electroosmotic sampling is defined by how close the probes are to one another and also the diffusion/electrokinetic fluid movement within the tissue. Push-pull electroosmotic sampling becomes a more versatile method when considering the ability to model and calculate the fluid flow dynamics within the tissue, such as flow rate, as they are dictated simply by the electric fields within the tissue. Because of the ability to calculate the path and time it takes a molecule to move from push to pull probe, this method holds the potential to be utilized in quantitative kinetic studies.

1.3.2 Damage Considerations

A primary concern arising from the logistics of this sampling design is the effects of an electric field on living tissue. A pyramidal neuron in the hippocampus has a resting potential of approximately -65 mV[55], with the extracellular fluid being more negative than the cytosolic fluid. When placing a cell in an electric field, the portion of the cell's membrane facing the cathode will be depolarized; the opposite side will be hyperpolarized. While hyperpolarization causes no known adverse effects to a cell, depolarization of the cell membrane from its resting potential can evoke an action potential. A key component to normal signaling, this action potential quickly spreads to other cells through voltage-gated channel. Triggering of an action potential causes the membrane potential to rapidly spike from -65 mV up to anywhere between 40 - 100 mV then rapidly fall back below resting potential (hyperpolarize) and return then to resting potential in the course of 4 ms. This will cause the release of neurotransmitters into the extracellular space and/or synaptic cleft, which go on to affect other cells. Because the electric fields created by electroosmotic sampling have the capacity to depolarize neurons, there is a concern that electroosmotic sampling may evoke unnatural signaling, and thus skew the chemical nature of the sampling site. After an action potential event, a cell needs to rest before

another depolarizing event occurs. Prolonged depolarization, repeated depolarization or depolarization past a neuron's normal peak of 40-100 mV may cause irreversible damage.

Electroosmotic sampling relies on an applied potential to move fluid for sampling. Fluid velocity is directly proportional to current, and thus applied voltage. Low flow rates were better in microdialysis and push-pull perfusion because collection was diffusion driven, however in electroosmotic sampling, we move the extracellular fluid to be collected. Thus, a higher sample volume will be best achieved at high flow rates and thus high voltages/currents. This, however, is damaging to the tissue. This document outlines the development of two different sampling models wherein we seek to minimize damage and perturbation to the tissue, understand and control flow dynamics, and utilize the method to study enzyme kinetics in the extracellular space.

2.0 THE ORGANOTYPIC HIPPOCAMPAL SLICE CULTURE

As previously noted, the OHSC is a popular method for investigating a wide variety of neuronal mechanisms due to its distinctive organization, its retention of *in vivo*-like characteristics, and the added accessibility and simplicity over the *in vivo* model. We used the OHSC to develop electroosmotic sampling and to investigate hydrolysis of peptides in the hippocampus, using only viable, healthy cultures. The ability to identify portions of the hippocampal formation is an indication of culture viability. The hippocampal formation (and the OHSC) is comprised of several structural areas of interest and two primary neuronal types. Smaller close packed granule cells comprise the two blades of the dentate gyrus (DG). Pyramidal cells are larger, less densely packed neurons, which comprise the remaining Cornu Ammonis region 3 (CA3) and CA1 regions. The cell arrangement in the hippocampus is laminar in nature, with the soma lined up projecting axons and dendrites in opposite directions and lined up with each other. Figure 2 illustrates these structural areas in a micrograph.

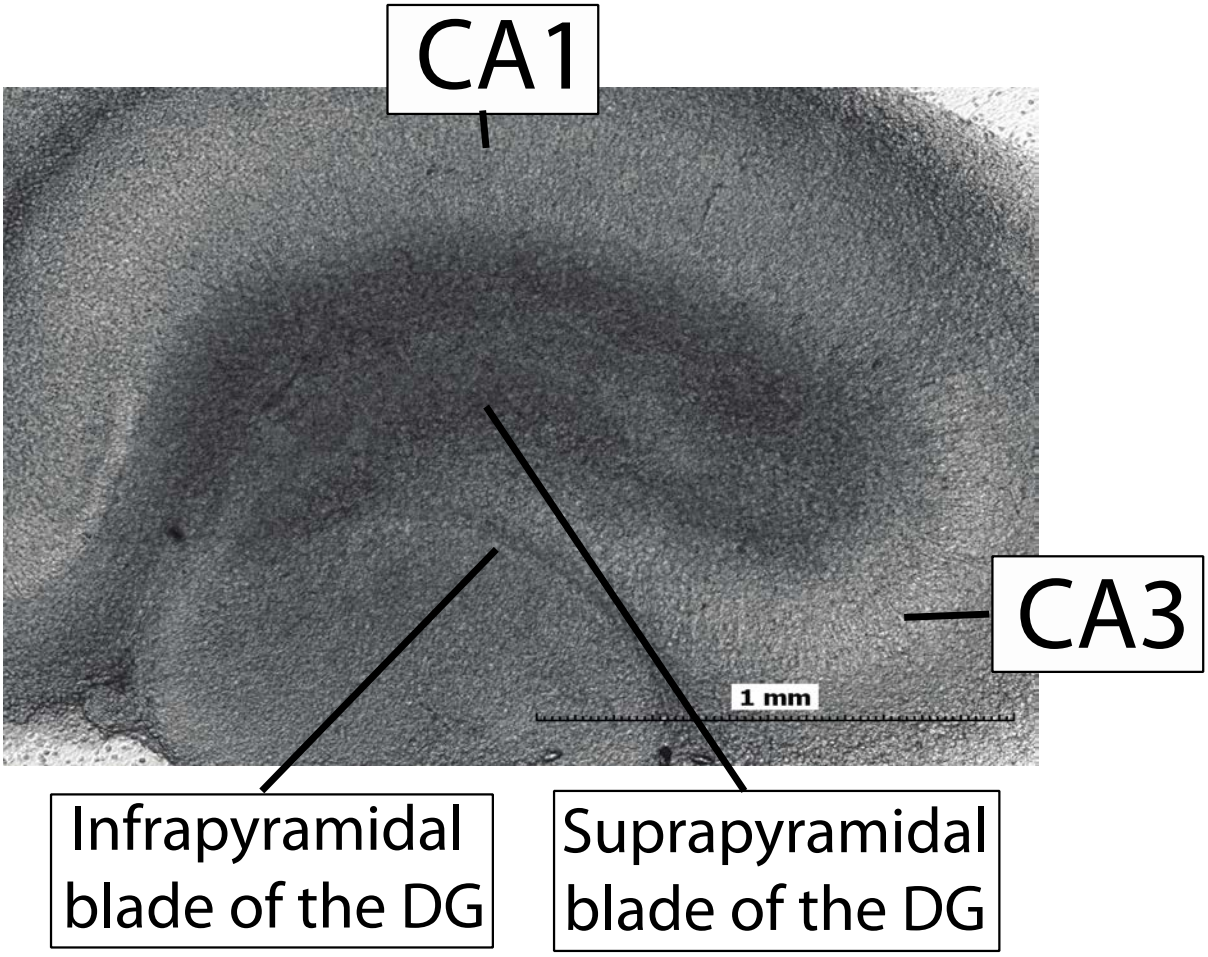

Figure 2. A micrograph of the organotypic hippocampal slice culture (OHSC)

The DG is comprised of two blades – the suprapyramidal (or buried blade) and the infrapyramidal (or exposed blade). The cell bodies and dendritic branches, particularly the pyramidal cells of the CA3 and CA1 seem lighter here, where the axons extend in to areas of white matter, which seem darker. Additionally, the pyramidal cell layer can be identified specifically by the fibrous appearance, when the tissue is at low magnifications (4x here).

Over the course of this work, the protocol for dissecting and maintaining the slice culture samples was modified following a long period inadequate culture development. Despite attempts at prolonged culture, the viability of the majority of our cultures cultured in the early part of this work declined in viability after 8-10 days in culture. Additionally, neurons in the CA1 and the suprapyramidal blade of the dentate gyrus (DG-SP) died before the rest of the tissue seemingly without cause. Our dissatisfaction with culture reliability led to a full and comprehensive

examination of all aspects of the dissection and culturing process. Through this process, we discovered quite a bit about the OHSC, and feel that a separate chapter on our findings may be helpful to others experiencing problems as well. We outline here our findings, other attempts we have made to characterize the OHSC, including culture thickness and the thickness of the glial cell layer that blankets the top of the tissue as it develops.

2.1 EXPERIMENTAL

2.1.1 Solutions and Reagents

Culture and Dissection Media: At the start of our studies, prior to culture deterioration, we were using what will be referred to as culture medium 'A'. Culture medium 'A' was composed of 50% basal medium eagle (BME), 25% Earle's balanced salt solution (EBSS), 23% heat inactivated horse serum, 25 U/mL penicillin-streptomycin (PEST), 1 mM L-glutamine, 41.6 mM D-(+)-glucose, all from Sigma-Aldrich (St. Louis, MO, USA). We used Gey's balance salt solution (Sigma) supplemented with 0.5 % D-(+)-Glucose and 2.7 mM $MgSO_4$ as a dissection solution. Culture medium 'B', which was used after our studies on tissue viability, was antibiotic-free and was comprised of 50% opti-MEM, 25% horse serum, 25% Hank's balance salt solution with phenol red (all from Life Science Technologies, Carlsbad, CA, USA), supplemented with 1% D-(+)-glucose (Sigma), and filtered through a Nalgene filter of either 0.45 μm or 0.1 μm pore size (Fisher Scientific, Waltham, MA). Dissection solution was serum-free culture medium, replacing the serum component with opti-MEM, also filtered through a Nalgene filter unit. In some cases, a B-27 supplement (Invitrogen) was added to culture medium.

Fixing and Staining Reagents: A Hank's balanced salt solution (HBSS, Life Technologies, Carlsbad, CA, USA) was used in all rinsing. A fixative 4% paraformaldehyde aqueous solution was supplemented with NaCl (134 mM), KCl (5.40 mM), $MgSO_4$ (1.20 mM), NaH_2PO_4 (1.38 mM), and $CaCl_2$ (2.65 mM). Other reagents used in fixing/staining include Triton-X-100, normal goat serum, anti-glial fibrillary acidic protein (GFAP) produced in rabbit, Alexa-Fluor 488 conjugated goat anti-rabbit IgG (H+L), anti-neurofilament-M+H produced in mouse, Alexa

Fluor 405 conjugated goat anti-mouse IgG (H+L), and Alexa Fluor 647 conjugated goat anti-chicken mouse IgG (H+L), all obtained from Life Technologies, and anti-integrin alpha-M produced in chicken (Aves Lab, Inc., Tigard, OR, USA). Cultures were mounted on slides using fluoro-gel medium made with tris buffer (Electron Microscopy Sciences, Hatfield, PA, USA).

2.1.2 Dissection

For experiments before viability studies, we used dissection protocol 'A'. In this protocol, we used Doyen abdominal surgical scissors (Fisher Scientific) to decapitate an immature Sprague Dawley rat pup (post-natal 7 days, p7). The scalp and skull were opened and removed by standard dissection scissors (Fisher Scientific). The brain was removed by microspatulas and placed upside down on a drop of GBSS in a petri dish on a stage cooled with dry ice. The hippocampus was removed and transferred to the stage of a tissue chopper (McIlwain, model TC752) by microspatula. Cultures were chopped along the septotemporal axis at a thickness of 400 μm. After chopping, cultures were immediately submerged in GBSS (4°C), and separated using microspatulas. Two tissue slices were plated onto each transparent porous (0.4 μm) PTFE insert membrane surface (Millipore, Bedford, MA, USA) by transferring them in a wide bore pipette, fabricated by chopping off the end of a glass pipette and blowing the glass to ensure smooth edges, with dissection solution. A disposable glass pipette was used to remove any excess liquid from the tissue. Cultures were cultured in a 6-well plate (Sarstedt, Newton, NC, USA) over 1.2 mL of culture medium A, incubated in 5 % CO_2 and 95 % air at 36.5°C for 5-9 days before experimental use.

When tissue viability began to decline, we focused on dissection and culturing technique. We carried out a full factorial design experiment. We investigated the role of rat pup age (p7 versus p9), chopper blade strength (low versus high), initial slice thickness (300 μm versus 500 μm), medium composition, and the addition of a B-27 supplement to the medium. The slice thickness and the B-27 supplement were examined as we speculated that thicker tissue might prevent medium and/or oxygen from diffusing to the thicker portion of the tissue (the CA1 and the infrapyramidal blade of the DG). Literature showed that the age of the pup prior to dissection, to some extent, has an impact on the overall viability of the cultures[37, 56, 57]. The chopper blade thickness was examined to create a gentler chopping process. The medium was

altered from ‘A’ to culture medium ‘B’ as other protocols for the interface method utilized different recipes[43]. Detailed results will be discussed later, but this study ameliorated some problems, but not all.

Approximately two years after the viability studies, a change in dissection protocol was introduced after reading a protocol by Gogolla[58], which we will refer to as dissection protocol ‘B’. In this protocol, after decapitation, the head was submerged for a few seconds in 70% ethanol (30% water). Removal of scalp and skull were identical as the first protocol and the brain was laid upside down on filter paper (Whatman) wetted with dissection medium. Approximately 1 mL of cold dissection medium (4°C) is pipetted to the top of the upside down brain. Isolation of the hippocampus occurred identically as the first protocol, but was transferred to chopper stage by removal in dissection solution by wide-bore glass pipette. Excess dissection solution was removed from chopper stage by glass pipette. Chopping occurred identically at a thickness of 350 μm. Cultures were removed from the stage by pipetting dissection medium onto freshly chopped slices and removing all contents by wide bore pipette. Cultures were placed in a small dish of cold dissection medium. The medium was aspirated gently several times to separate cultures that may be stuck together. Then, cultures were incubated at 4°C for 30-90 minutes. After incubation, cultures were plated identically as the first protocol. The medium was exchanged every 2-3 days during incubation.

2.1.3 Cell Death Analysis

Prior to any experiments involving the OHSC, the cultures were examined for overall structural integrity and stained with propidium iodide (PI), a fluorescing DNA-intercalating agent that can only gain access to the nucleus through a compromised cell membrane. PI is routinely used to assess neuronal PI fluorescence was imaged using an inverted fluorescence microscope (IX-71 with U-MGIW2 cube from Olympus, Melville, NY) with image acquisition software (Simple PCI). Increased red fluorescence indicated a greater density of dead cells.

2.1.4 Tissue Thickness

Stoppini initially stated the thickness of the OHSC to be roughly 150 μm after two to three weeks in culture [36]. As the thickness of the tissue will prove pertinent to electroosmotic sampling, we verified the OHSC thickness for days 6-8 in culture by measuring the position of a metal probe when it is in contact with the top surface of the tissue, and comparing that to the position of the same probe when it is in contact with the insert membrane nearby. Positions were determined by noting the readings on an electronic micromanipulator (MP-285, with ROE-200 controller and MPC-200, Sutter, Novato, CA). Contact of the conducting probe with the tissue/insert membrane surface was determined by using an ohmmeter (Fluke Corporation, Everett, WA) connected to the conducting probe held by the micromanipulator and a second probe in the medium.

2.1.5 Fixing, Staining, and Imaging

As OHSCs develop in culture, they develop a blanket of glial cells on the surface serving to protect the delicate neurons from the outside environment[59]. One of the electroosmotic sampling designs requires a probe to be inserted into the tissue; it is thus important to know how thick the glial cell layer is to determine a probe depth required to create a sampling site that is primarily neurons. Tissues were fixed and stained to identify the glial cell layer. To begin the process, cultures were rinsed 3 times with warmed (37ºC) HBSS solution and then fixed for 4 hours at 4ºC in the paraformaldehyde aqueous salt solution. Cultures were then rinsed 3 more times with room temperature HBSS. Cultures were then incubated for 2-3 hours in a blocking solution (1% goat serum, 0.1% Triton X-100, followed by 3 more rinses with HBSS solution. Cultures were then cut out of remainder of the solid insert membrane support. These cultures were carefully transported to a plastic petri dish and incubated for 48-90 hours in the first antibody solution (0.2% of anti- antibodies directed at GFAP (astrocytes), integrin alpha-M (microglia) and neurofilament (neurons) proteins). Typically cells are incubated for a shorter time and this lengthened incubation time was chosen to be sure the antibody penetrated deep into the tissue. The cultures were then rinsed 3 times with HBSS and then chopped perpendicular to the hippocampal formation at a cross-sectional thickness of 150 μm. Small tissue sections still

attached to the insert membrane were then transferred to the secondary antibody solution, containing 2% of each of three Alexa Fluor – conjugated secondary antibodies and were incubated at room temperature for 2-4 hours. Before mounting on slides, cultures were rinsed 3 times with HBSS by moving the cross-sections into new wells with fresh HBSS. Cross-sections and their attached insert membranes were carefully laid on their side on a glass slide and a fluoro-gel mounting medium was added drop wise to the top of the cross-sections. After a few minutes, cover slips were put on top. A few drops of water were placed on the slide before imaging. Cultures cross-sections were imaged on a confocal Leica DM6000CFS using a 20x water immersion objective. The Alexa Fluor 405-, Alexa-flour 488- and the Alexa Flour 647-conjugted secondary antibodies were excited with a 405 nm, a 489 nm, and a 633 nm laser respectively.

2.2 RESULTS

2.2.1 Tissue Viability

In early 2008, the cultures cultured with medium ‘A’ and dissected according to protocol’ A’ began to deteriorate in quality. Figure 3, panel A, shows a micrograph of a healthy, viable OHSC. Panel B shows a fluorescence image of the same tissue treated with propidium iodide, a cell death marker. There is slight cell death in panel B, but it is minimal. Panel C, D, and E show the quality of the cultures that were obtained during the period of deterioration. The tissue in panel C is grainy in overall appearance, possibly due to an overgrowth of unorganized cells. The central part of the tissue, the DG-SP and CA1 areas, in panel D is dark in color, and in panel E, the propidium iodide treatment reveals extensive cell death of these structural regions.

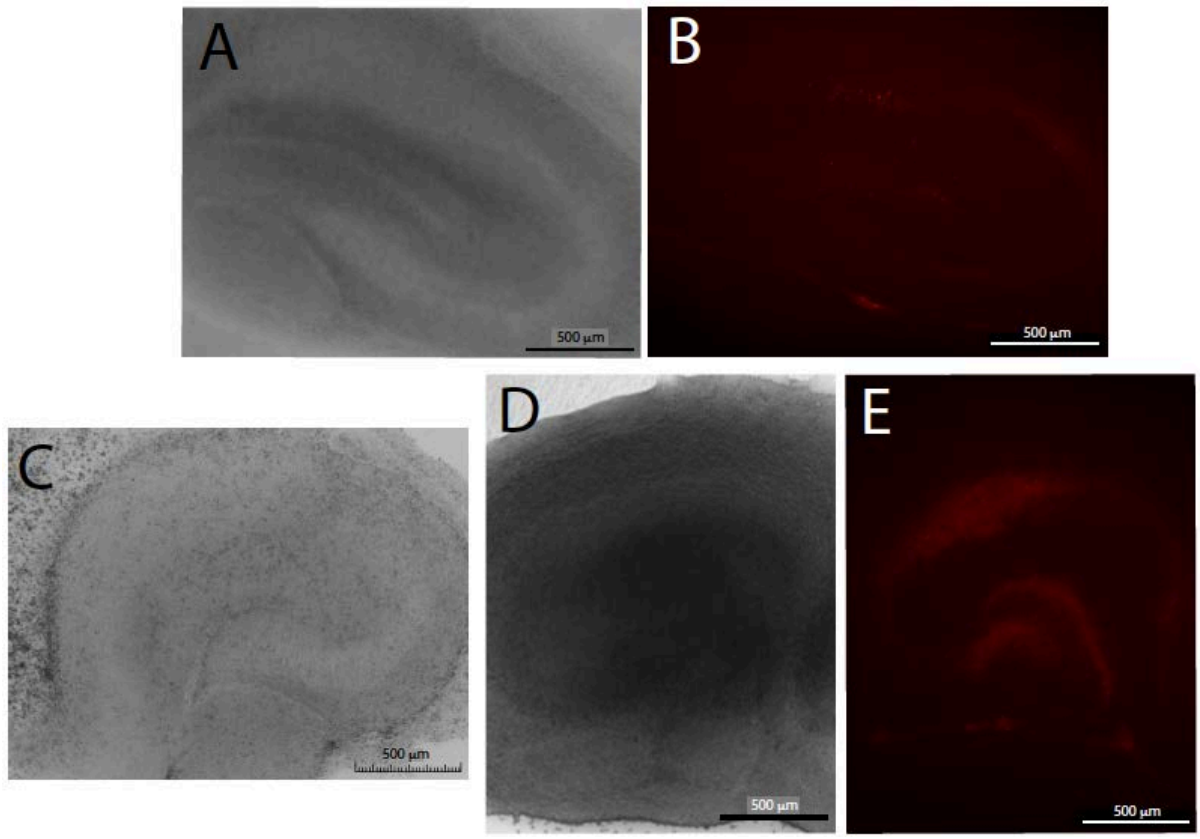

Figure 3. Bright field and fluorescence images of OHSCs stained with propidium iodide

These cultures were treated with propidium iodide to detect cell death (see Figure 20 for image of 100% dead tissue stained with PI for reference). Panels A and B are the same tissue imaged in bright field and for PI fluorescence respectively at 6 days in culture and represent healthy viable cultures. Panel C shows a tissue of the same culture time as A and B, showed no significant cell death (not shown), but does not exhibit proper development. The grainy appearance indicates a possible overgrowth of cells, perhaps glia. Additionally, the margins around the tissue, particularly on the left side adjacent to the CA1 area are a mosaic of darker and lighter cells. This phenomenon is not seen in the margins of healthy cultures (panel A, right side also adjacent to CA1 area). Panel D and E are the same cultures. While the margins of tissue D are smooth like panel A, the center of the tissue is opaque and the structure of the DG is not clear. As seen in panel E, this dark area co-localizes with areas of extreme cell death in both the CA1, the suprapyramidal blade of the DG and even the CA4 (the area between the CA3 and the blades of the DG)

We investigated rat pup age, chopper blade strength, slice thickness, medium composition and addition of B-27 supplement to the medium. To avoid bias, three individual people carried out surgical dissections and culturing while a fourth rated the viability of each tissue. Slices obtained from 7 days post-natal rat pups resulted in slightly healthier cultures than those obtained from p9 rat pups. The chopper blade strength seemed to have no effect on culture

viability, nor did the B-27 supplement. Cultures chopped at 300 μm initial thickness resulted in healthier cultures than those chopped at 500 μm. Culture medium 'B' led to healthier cultures than medium 'A'. After this study, we switched to routine use of medium 'B', p7 rats, and cultures of initial thickness of 350 μm, since 300 μm were difficult to separate. Chapter 3 utilizes cultures from before this study and after this study. However, viability of cultures via PI imaging was checked before all experiments, ensuring all results are reliable.

These changes, implemented in mid-2009 improved the structural integrity of the cultures and slightly decreased the occurrence of spontaneous neuronal degeneration of the CA1 and DG areas. About 40-60% of cultures survived with an acceptable viability for use in experiment. Bacterial contamination was a recurring issue, but the lack of antibiotics made it easy to diagnose and discard contaminated samples.

In early 2010, the discovery of a protocol published by Gogolla[58] prompted further examination of the surgical protocol and routine disuse of dissection protocol 'A' in favor of dissection protocol 'B'. These alterations eliminated bacterial contamination and routinely led to cultures that were viable for at least one month. The gentler treatment of the cultures dramatically decreased the spontaneous death of CA1 and DG neurons. In hindsight, these latter alterations likely impacted viability more than the earlier change in medium composition and initial slice thickness, however, since all cultures were pre-screened for viability before use, the culturing and surgical procedures, for all intents and purposes, had no meaningful effect on the final data. Thus, culturing and surgical procedures will not be mentioned when noting the sampling parameters used to obtain each data set.

2.2.2 Culture Thickness

The thicknesses of the cultures depended greatly on the medium used in culture. For those cultured in the initial media comprised primarily of BME and EBSS, and an initial chopping thickness of 500 μm, the mean thickness for these cultures was 192 ± 3 μm (n = 30 OHSCs). For those cultured in the media comprised primarily of opti-MEM and HBSS, and chopped initially at either 400 μm or 500 μm, the mean height is 158 ± 4 μm (n=61 OHSCs). The measurement for each tissue in all instances relied on four height measurements for the tissue and 4 height measurements for the insert membrane, and the latter set of data revealed that the final thickness

does not depend on initial chopper settings. Thus, even though not measured, we have assumed that the OHSC thickness from the BME/EBSS medium, with an initial tissue chopper setting of 400 μm, is also 148 ± 8 μm. The results of this study have been published in detail[60].

2.2.3 Glial Cell Layer Thickness

Three cell types were identified through immunoflourescent staining: neurons, astrocytes, and several types of microglia (oligodendrocytes, ependymal cells, and satellite cells). Figure 4 shows representative images, which are all full projections of a confocal stack. The glial cell layer varied from tissue to tissue, with a mean thickness of 29.5 mm ± 5.6 (n=15).

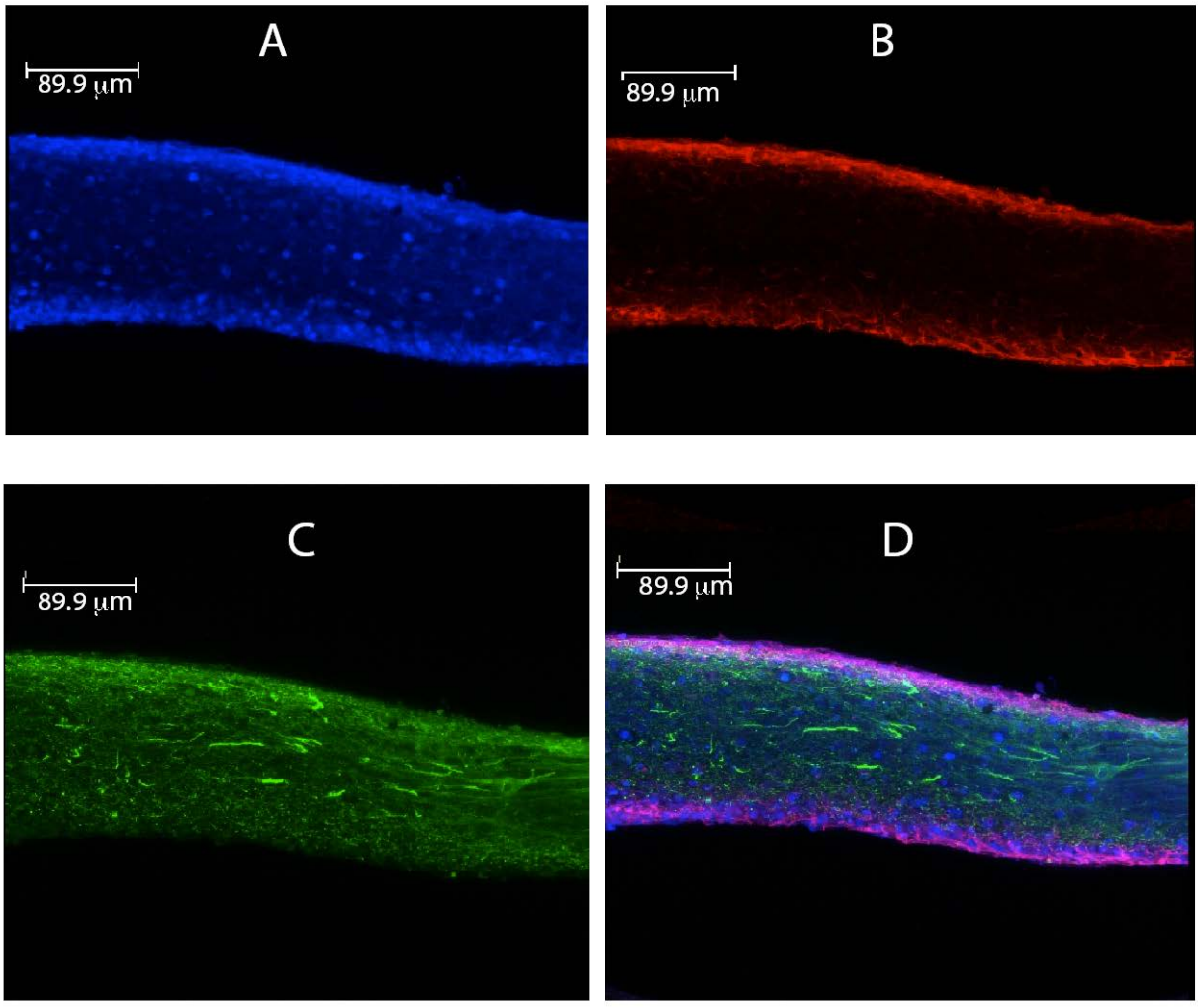

Figure 4. Immunoflourescent images of OHSC cross-sections

(A) OHSC cross-section treated with anti-integrin alpha-M produced in chicken and Alexa Fluor 647 conjugated goat anti-chicken mouse IgG (H+L) (B) OHSC cross-section treated with anti-glial fibrillary acidic protein (GFAP) produced in rabbit and Alexa-Fluor 488 conjugated goat anti-rabbit IgG (H+L) (C) OHSC cross section treated with anti-neurofilament-M+H produced in mouse and Alexa Fluor 405 conjugated goat anti-mouse IgG (H+L). (D) An overlay of images (A), (B), and (C).

3.0 SINGLE CAPILLARY ELECTROOSMOTIC SAMPLING

3.1 INTRODUCTION

Electroosmotic sampling is possible because the extracellular space of the OHSC has surface charge, a zeta potential (~ -22 mV), and thus supports electroosmotic flow[53, 61]. When exposed to an electric field, extracellular fluid moves according to that field, and can be drawn into a capillary, which also has a zeta potential and supports electroosmotic flow, in contact with the tissue surface.

The first sampling model developed uses a single fused silica capillary placed perpendicularly to and in contact with the OHSC surface. The tissue sits over an electrolyte solution. Potential is applied to the tissue and capillary such that fluid moves from the electrolyte, into the tissue, and into the collection capillary above the tissue. Figure 5 shows the apparatus used to induce electroosmosis. We call this design single capillary electroosmotic sampling.

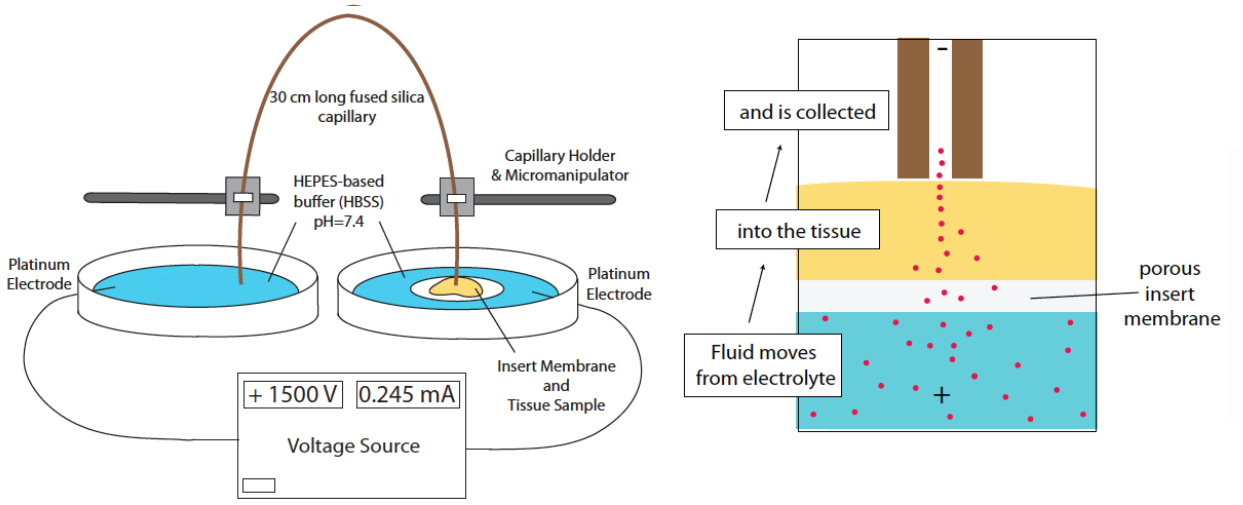

Figure 5. Single capillary electroosmotic sampling design

A 30 cm long buffer-filled fused-silica capillary held in place by two micromanipulators connects a buffer filled reservoir with the surface of an OHSC cultured on a PTFE Biopore membrane. Two platinum electrodes connect each buffer reservoir to a voltage source. When voltage is switched on with the indicated polarity, electroosmotic flow in the OHSC and the capillary will pull fluid from the tissue into the capillary.

In any sampling procedure applied to tissue, there is a tradeoff between conditions supporting simple, accurate and rapid analysis of the sample, and conditions that perturb the tissue minimally. For example, acquiring more sample volume at higher flow rates in push-pull perfusion leads to fewer difficulties in sample handling and analysis, but more damage. In electroosmotic sampling, we anticipate that the same sort of considerations will lead to optimum conditions. Higher electric fields in the tissue created by increasing the applied voltage or current, or positioning the capillary closer to the tissue surface create a higher flow rate and larger sample volumes in a given time. We anticipated that higher electric fields would at the same time induce more damage in the sampled tissue. Additionally, larger capillary inner diameters (i.d.) afford larger sample volume but also induce a larger current through the tissue. As a result of these considerations, we examined a range of capillary diameters and applied voltages that encompassed what we believe to be suitable for sampling[54]. Our goal was twofold: to find conditions that caused minimal damage in the tissue culture during electroosmotic sampling and to find a single parameter in which all sampling geometries could be applied under which there was a single threshold that would result in minimal damage. As experiments were

conducted, it was clear that simply applied voltage or current was insufficient to achieve this second goal. Thus, mathematical modeling of various electrical distributions within the tissue during electroosmotic sampling was conducted using COMSOL Multiphysics. Since my primary goal was simply to assess damage and dictate 'safe' conditions, a technical point should be made. In this chapter, unless otherwise specified, sampling refers simply to the placement of the collection capillary and application of electric field. No sample was actually collected when studying the effects of 'sampling' on damage.

3.2 EXPERIMENTAL

3.2.1 Solution and Reagents

Culture medium 'A' and 'B' were both used to culture cultures used here. We used Gey's balance salt solution (Sigma) supplemented with 0.5 % D-(+)-Glucose and 2.7 mM $MgSO_4$ as a dissection solution and as a rinsing solution. Two buffer solutions were utilized during sampling. The first was a HEPES-based buffer prepared in-house by dissolving NaCl (134 mM), KCl (5.40 mM), $MgSO_4$ (1.20 mM), NaH_2PO_4 (1.38 mM), $CaCl_2$ (2.65 mM), HEPES (5.00 mM, all from Sigma) and β-D-glucose (10.0 mM, from MP Biomedicals, LLC; Solon, OH, USA) in purified Millipore water (Synthesis A10). The pH of the buffer solution was adjusted to 7.40 with NaOH solution then vacuum filtered through a 0.45 μm PTFE membrane and frozen until the day of use. For convenience, later experiments used Hank's balance salt solution (HBSS), purchased from Life Science Technologies. These have slightly different conductivities, which are taken into account in mathematical modeling of electroosmotic sampling, but serve to buffer the tissue from pH changes when outside the CO_2 incubator. Both will be referred to as HBSS buffer. Propidium iodide (PI) solutions were prepared by dissolving solid PI (Sigma) in HBSS at a final concentration of 0.35 mM and frozen until use.

3.2.2 Assessment of Viability

To assess culture viability prior to performing experiments, PI (7 μM) was added to culture medium 16-24 hours prior to the desired sampling time. For each experimental cycle, a pair of cultures on one insert was intentionally damaged irreversibly by treating them with methanol. A few hundred microliters of methanol were pipetted onto the top of two cultures. After at least 5 minutes of exposure, excess methanol was then aspirated away. The next day, medium was replaced with warmed (37°C) GBSS and cultures were imaged using an inverted fluorescence microscope (IX-71 with U-MGIW2 cube from Olympus, Melville, NY) with image acquisition software (Simple PCI). The exposure time used for assessing PI fluorescence in experimental OHSCs was set to the auto-exposure time for the methanol-treated OHSC. Any OHSC showing extensive cell death was noted and not used for sampling. GBSS was then replaced with fresh medium and the cultures were returned to the incubator until sampling.

3.2.3 General Sampling Procedure: Single Capillary

One 6-well plate of cultures (12 cultures) was removed at a time from the incubator for experiments. Electroosmotic flow was induced in viable OHSCs before the plate was returned to the incubator (OHSCs remained outside the incubator for approximately 1.5 hours).

A fused silica ‘collection’ capillary (Polymicro Technologies, L.L.C., Phoenix, AZ), 30 cm long, ranging from 75 to 280 μm i.d. were cut with a Shortix capillary cutter (Scientific Instrument Services, Ringoes, NJ, USA) with diamond blade to ensure a clean, straight cut to the end. The capillary was filled with HBSS and ends were submerged in HBSS-filled dishes. The electrodes were 0.3 mm diameter platinum wire and were held in place contacting the buffer solution through slits cut in the sides of the plastic dishes. The voltage source was a high voltage power supply, model PS350 from Stanford Research Systems (Sunnyvale, CA, USA). A manual manipulator held the collection capillary in place in the dish absent of tissue while the electronic micromanipulator held the end of the capillary above the tissue surface.

Positioning of the collection capillary relative to the tissue surface was performed in one of three ways. Each method was an improvement on the reliability and reproducibility of the previous. The first relied on an established tissue thickness, measured to be 148 ± 8 μm at 6-8 days in culture at the time of the experiments[61]. In this method, a dry, empty capillary was slowly

lowered perpendicularly to the surface of the insert membrane near the tissue edge. Movement of the capillary was carefully determined visually through a Stereomaster Zoom microscope (Fisher). Once the capillary tip contacted the surface of the insert membrane, the position was noted and the tip was raised 200 μm. The capillary was then moved laterally to the desired area of the tissue. This position was noted, the capillary raised and filled with an HBSS buffer solution with syringe such that a droplet of buffer formed on the end of the capillary but did not fall off. The capillary was then returned to the previously saved position, which was approximately 50 μm above the tissue. Contact between capillary and tissue occurred via the droplet of buffer, which spread out upon contact with the tissue surface. Sampling then commenced by switching on the voltage.

Method 2 is a refinement of Method 1 to remove variability from the natural variation in OHSC thickness. In Method 2, the dry capillary was slowly lowered directly to the surface of the OHSC (not the insert membrane), until it made contact. The capillary was then raised the desired distance (capillary-to-tissue distance or 'CTD') or kept at this location if the desired capillary-to-tissue distance is '0 μm'. Similar to method 1, this position was saved, the capillary raised and filled with HBSS buffer leaving a droplet to hang off the end, then returned to the sampling site. Sampling then commenced.

While these methods ensure accuracy and precision of the capillary-to-tissue distance and thus the electric field in the tissue, they proved impractical for routine sampling. Method 3 arose out of Method 2 and is identical in all but one aspect – the capillary starts out filled with HBSS buffer solution. It was identically lowered to the surface until contact was made then raised the desired capillary-to-tissue distance. All three methods were investigated to determine safe sampling conditions.

To apply potential across the tissue, a specified voltage was applied across the Pt electrodes (Figure 5); current was monitored during this time. It has been estimated that an electric field of 67 V/cm (2000 V applied over 30 cm) will electroporate cells[62]. The goal is to sample only extracellular space, and so only voltages lower than 2000 V were used. Voltage was turned on for 5 minutes, and the applied voltage ranged from 1000 to 1700 V. Following each sampling period, the capillary was raised, buffer replaced with fresh solution, and then repositioned on the next tissue to be sampled. Since the goal of these experiments was simply to investigate parameters that were safe to the tissue, no samples were actually collected. Both

cultures on an insert membrane were sampled and returned to their original position in the 6-well plate. At least 2 cultures (one insert membrane) were reserved for negative controls and were not exposed to any electric field. An additional 2 cultures were reserved for positive controls wherein 24-48 μL of methanol were added to the top of each tissue to ensure 100% cell death. The use of methanol here as a positive control was chosen because the use of NMDA, which is routinely used to induce excitotoxic neuronal death, resulted in a positive control that was less fluorescent than some sampled cultures. It was clear that glia were also being damaged and thus an agent that killed all cells was required.

3.2.4 Quantifying Tissue Damage

Once the electric field was applied to all desired OHSCs, medium under each insert membrane was replaced with fresh PI-containing medium (7 μM) and incubated 16-24 hours overnight. The next day, the medium was removed and replaced with HBSS. All OHSCs were imaged using the IX-71 inverted fluorescence microscope with an exposure time determined by the auto-exposure time of the methanol treated cultures.

For each tissue that was used for electroosmotic sampling, a positive control (PC) and negative control (NC) was also required to quantify the damage sustained during sampling. Figure 6 shows representative fluorescence images of these tissue types stained with propidium iodide.

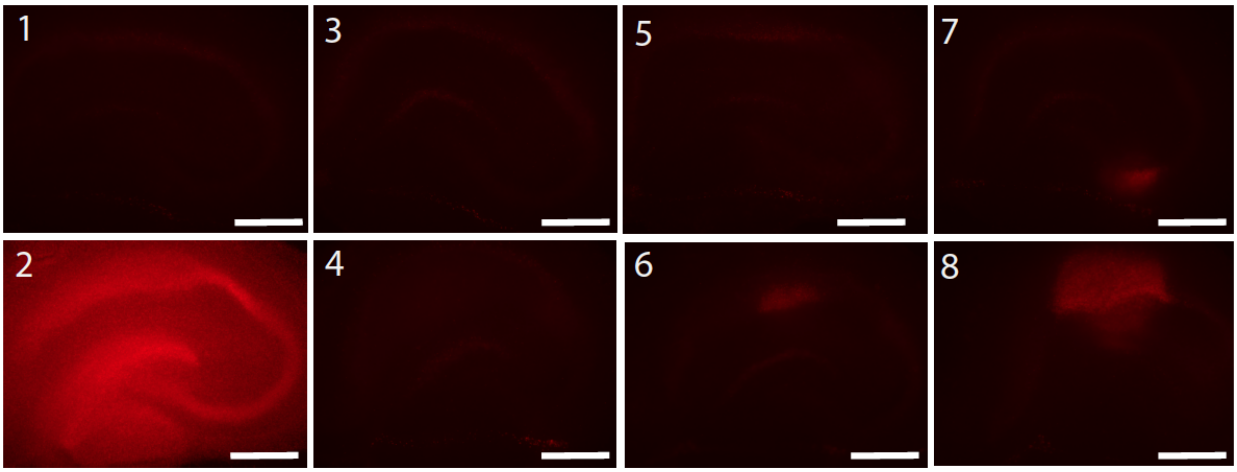

Figure 6. PI-stained cultures following electroosmotic sampling

Scale bars = 0.5 mm. (1) Live control. (2) MeOH-treated (100% dead) control. (3) and (4) 1300 V applied to CA3 and CA1, respectively, little to no cell death incurred. (5) and (6) 1400 V applied to CA3 and CA1 respectively; no cell death to CA3 but CA1 appears damaged. (7) and (8) 1700 V applied to CA3 and CA1 respectively; significant cell death to both areas, but CA1 cell death is more widespread. Overall, the CA1 is more susceptible to damage arising from the applied electric field than the CA3. Scale bars = 0.5 mm

To quantify the damage induced by electroosmotic sampling in any given tissue, propidium iodide fluorescence was measured using the SimplePCI software. Regions of interest were drawn around any visible damage as well as each hippocampal region in both positive and negative controls, as shown in Figure 7. The mean fluorescence intensity (average red intensity for all the pixels in the region of interest) and area of each region of interest is found. Modifying the image's histogram to get the most contrast facilitated the visualization of the perimeter of these areas in the negative controls. This process did not alter the data used for quantifying cell death in the image.

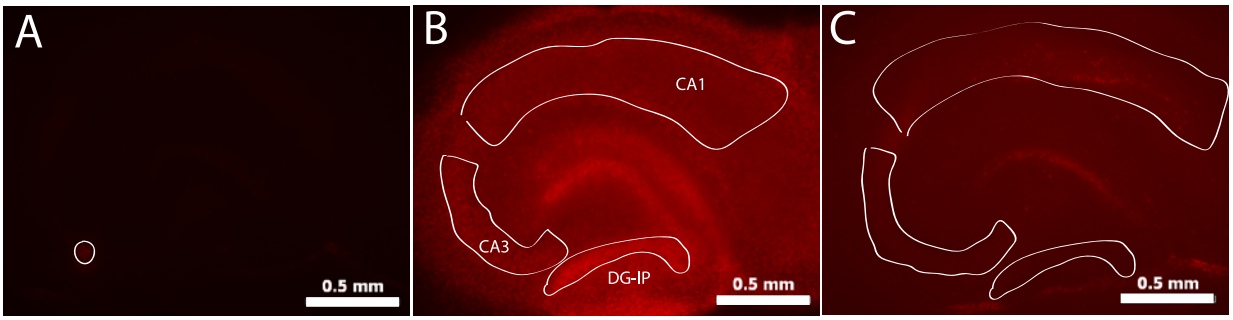

Figure 7. Example regions of interest for determining tissue damage

Scale bar = 0.5 mm. (A) "Local" region of interest drawn around the PI fluorescence seen by sampling site in the sampled tissue. (B) MeOH-treated positive control tissue with regional regions of interest drawn around the CA1, CA3, and DG-IP (C) Negative control tissue with regional region of interests drawn around the CA1, CA3, and DG-IP. The contrast in (C) has been increased to facilitate visualization of the hippocampal structure.

The total damage in the region sampled (i.e. CA3) is calculated using Equation 1 where I is fluorescence intensity, and subscripts S, NC, and PC refer to sample, negative control, and positive control, respectively and A_R is the area of the particular region where sampling occurred.

$$total\ damage\ sampled\ tissue = (I_S - I_{NC}) \times A_S \quad (1)$$

This represents a background subtracted total damage from sampling. The mean fluorescence intensity for the positive controls corrected for negative controls across all experiments is relatively constant, as is the area of the hippocampal region. Thus we calculate a similar total damage for positive controls for each region (CA1, CA3, DG), shown in Equation 2. This total damage represents the maximum damage that could have been incurred from sampling in the structural region (i.e. CA3).

$$total\ damage\ positive\ control = (I_{PC} - I_{NC}) \times A_R \quad (2)$$

3.2.5 Finite Element Modeling

We simulated single capillary electroosmotic sampling in COMSOL Multiphysics 4.3 to calculate voltage drops, electric field distributions, and power dissipated within the tissue during electroosmotic sampling. The model is drawn in 3D. Numerical solutions of the Laplace

equation were used to calculate the electric field distributions and voltage values within the model. Figure 8 shows a sketch with important boundary and subdomain conditions specified and a working 3D model as seen on the COMSOL desktop.

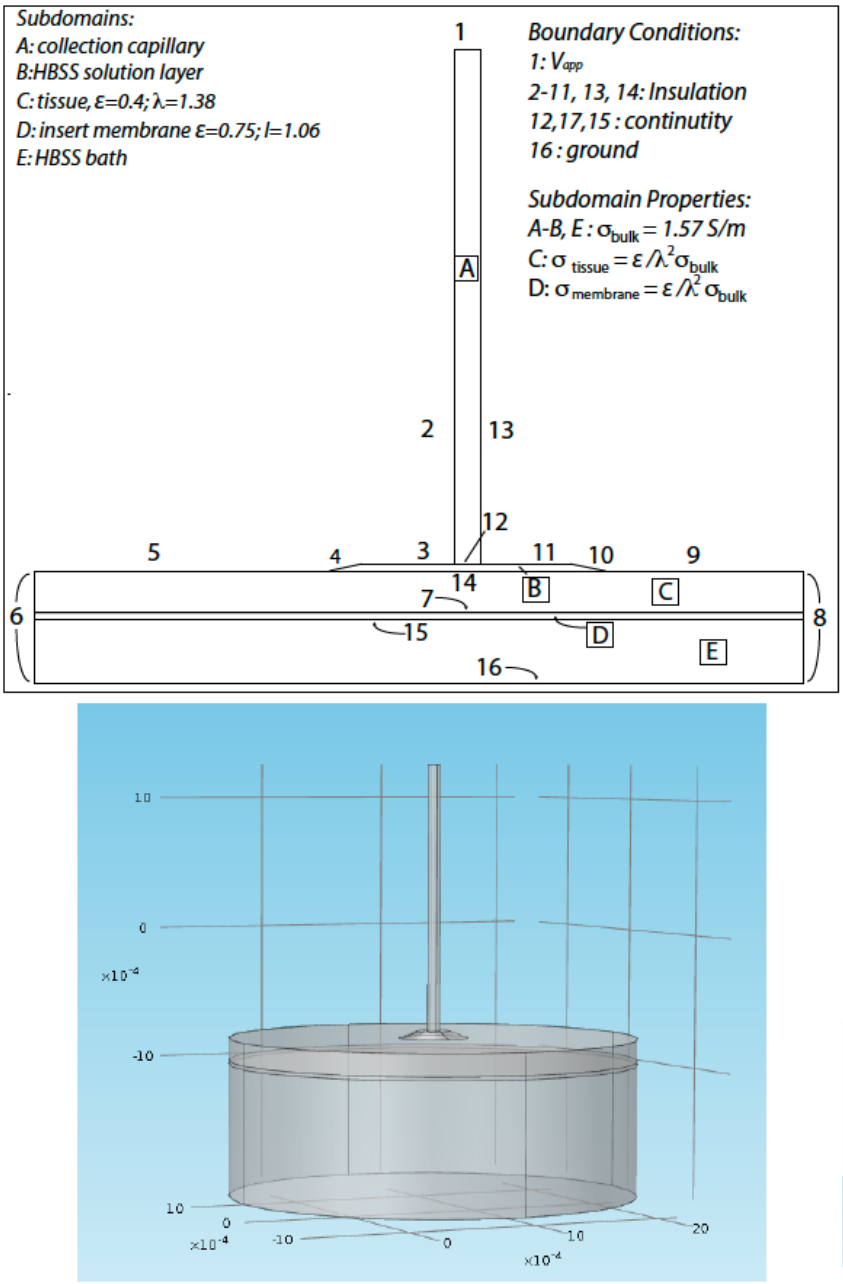

Figure 8. COMSOL model for single capillary electroosmotic sampling

(TOP) In each experiment, there is a layer of HBSS (subdomain B) with a thickness equal to the capillary-to-tissue distance between the capillary (subdomain A) and the tissue (subdomain C). The tissue is 160 μm thick. Subdomain D corresponds to the insert membrane below the tissue, which is 28 μm thick. Subdomain E corresponds to the buffer solution in which the insert membrane sits. Its thickness in the top panel is not drawn to size, and is 1 mm. The 30 cm capillary (A) is shortened to 1 mm in the COMSOL model. The applied voltage, V_{app}, in the model is set to 0.33% of the experimental voltage to simulate the effects of the full 30 cm length.

Subdomain B represents a layer of buffer between the tissue surface and the lumen of the capillary. Experimentally, this HBSS layer keeps the collection capillary in contact with the tissue, as raising the capillary off the tissue minimizes damage (to be discussed). The thickness of subdomain B is the capillary-to-tissue distance. The role of this buffer layer in damage control will be addressed later. The conductive media DC module solves the differential equation, $-\nabla(\sigma\nabla V) = Q$, where V is the electric potential, σ is the conductivity of the subdomain and Q is gradient of current density. The bulk conductivity of the HEPES buffer in the capillary and under the tissue is 1.57 S/m. The average conductance in the tissue and insert membrane is corrected with a formation factor, $\frac{\varepsilon}{\lambda^2}$, where ε is porosity and λ is a geometric tortuosity. The immature rat brain has a volume fraction of 0.41 μm[63] and the porosity of the insert membrane is estimated to be 0.75. There are no reported values of purely geometric tortuosity of OHSCs, however, the diffusion of TMA was measured in acute p5-p7 cultures and the tortuosity was found to be 1.39[63]. This is the best estimation to date. One review lists a series of equations relating tortuosity to porosity for a variety of situations[64]. Using the relationship $\lambda^2 = \frac{(3-\epsilon)}{2}$, the tortuosity of the insert membrane is set at 1.06. Because the tissue comprises < 0.05% of the total 'resistance length', the boundary condition at the top of the capillary (boundary 2) is set to the total applied voltage divided by the total length of the capillary, 30 cm, then multiplied by 1 mm (capillary length in COMSOL model).

3.3 RESULTS AND DISCUSSION

3.3.1 Damage

Using Equation 2, we find a total maximum damage value for the CA3 of 23.3 ± 1.2 and 43.6 ± 4.0 for the CA1. Most data presented here is in the CA3, with the exception of Figure 6, which shows the damage caused in each region in the hippocampus from sampling in those same regions using two different collection capillary diameters. Data could be scaled to % of maximum, but in this particular case it does not change overall trends.

Our goal is to define a trend in which we can relate cell death directly to a sampling parameter (i.e. current, electric field, voltage drop, etc.). We recognize damage as assessed by PI does not include all forms of tissue perturbation or dictate the requirement of all experiments. Some experiments may be uninfluenced by more damage, and some experiments may be perturbed by the electric field even if there is no resulting cell death 24 h after the experiment.

We plotted damage versus a variety of experimental parameters, including electric field, current, and power dissipated in the tissue. We found the best correlation to damage is found when comparing power dissipated in the tissue. Figure 9 shows this correlation. The other parameters did not result in as crisp a relationship. Figures A-1, and A-2 in Appendix A show damage with respect to applied electric field and current, respectively.

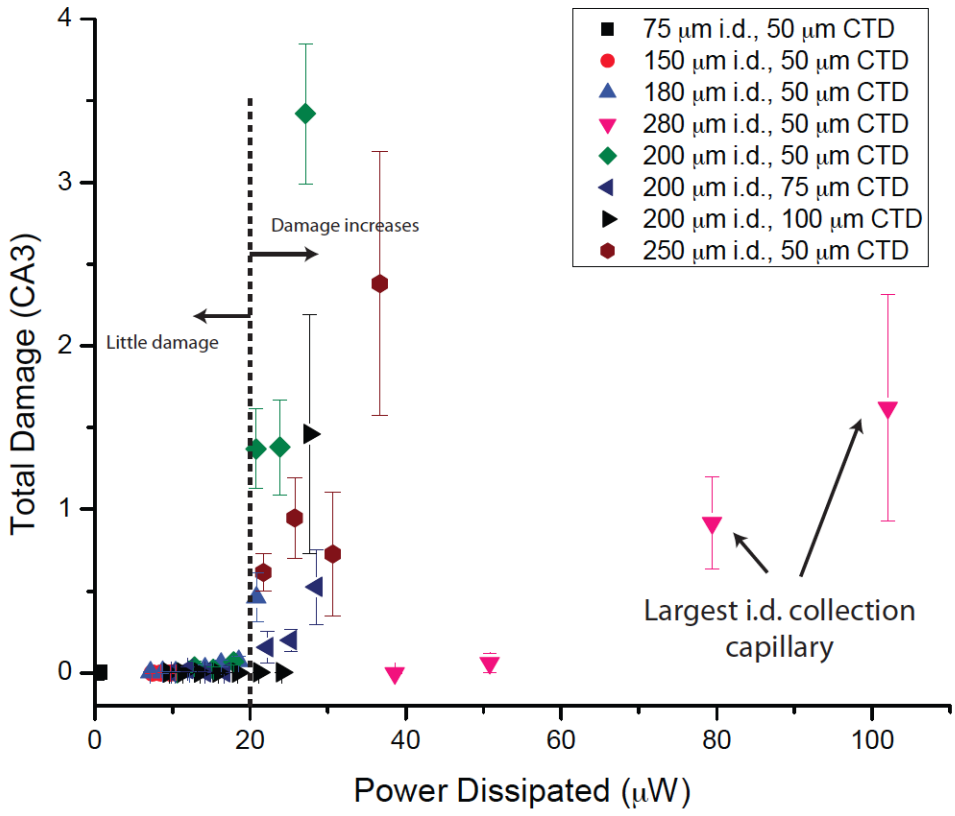

Figure 9. Total damage in CA3 after push-pull electroosmotic sampling of OHSC

A wide variety of applied fields and capillary dimensions were used to test effects on damage. Power was calculated by COMSOL by integrating the square of the electric field over the tissue and multiplying by the conductivity.

Dissipated power was calculated by COMSOL, integrating the electric field over the entire tissue and multiplying by the conductivity. There is an obvious increase in damage at 20 μW for all but the largest collection capillary i.d. We compared damage incurred from sampling in the CA1 to sampling in the CA3, shown in Figure 10, plotted with respect to power.

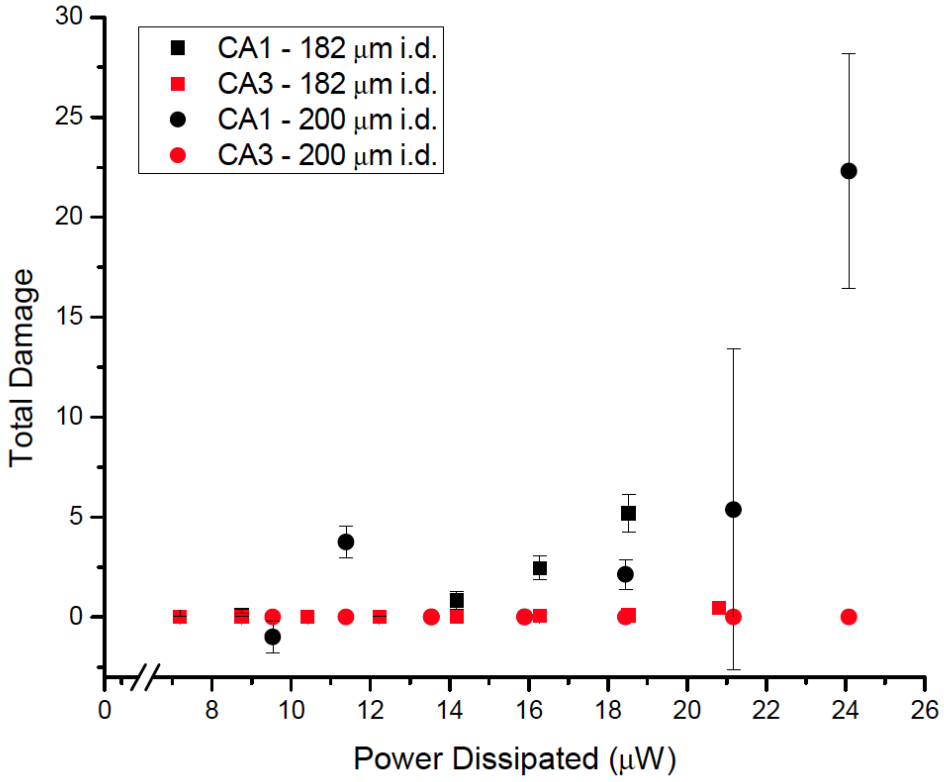

Figure 10. Damage after sampling the CA3 and CA1 regions of an OHSC

Two different collection capillary i.d.s were investigated, and similar trends were found for both. Overall, the CA1 is damaged more a greater power values than the CA3.

The CA1 is more vulnerable to excitotoxic and ischemic damage than the CA3 or other regions of the hippocampus[65]. This trend holds true for electroosmotic sampling, as seen in Figure 10, which shows data obtained from sampling. For larger power values, the CA1 becomes more vulnerable than the CA3.

Placing the collection capillary directly on the surface of the tissue results in extensive damage. To minimize this damage, the capillary was raised off the surface and the effects were

studied. The results are shown in Figure 12. Distances of 50 μm, 75 μm, and 100 μm were investigated; 0 μm is also shown. Applied fields ranged from 33 V/cm (~10 μW) to 54 V/cm (~35 μW), using a 200 μm i.d. collection capillary. Shorter distances between the capillary tip and tissue surface tend to cause more cell death.

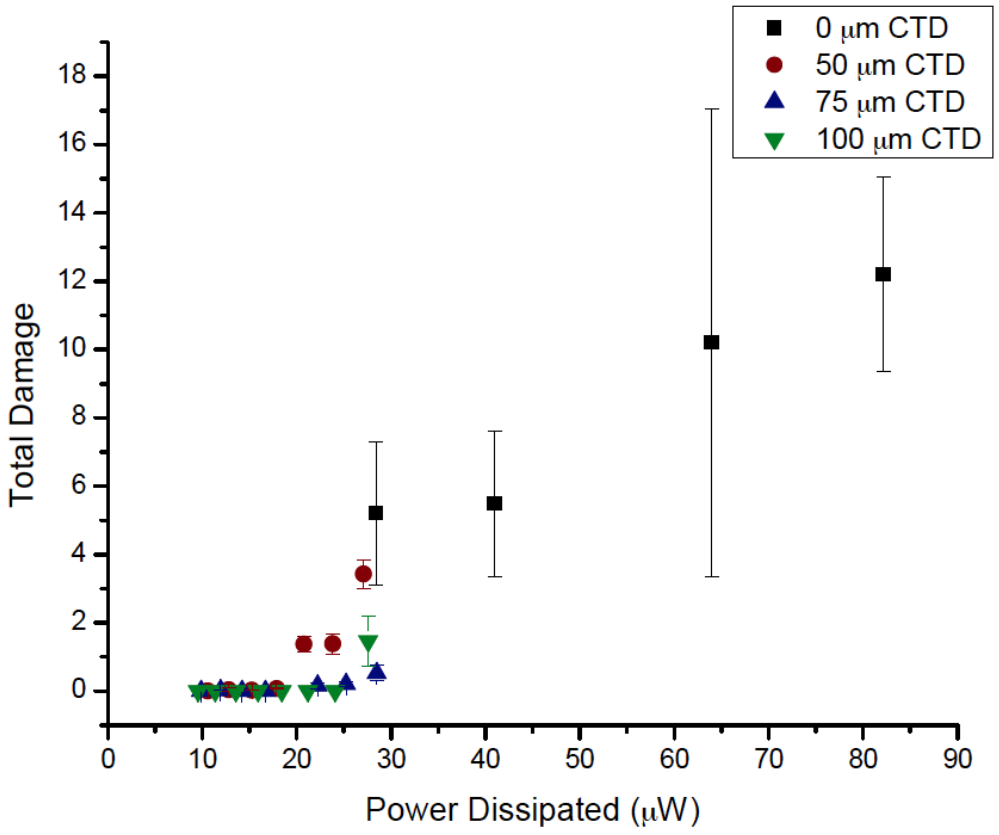

Figure 11. Damage to CA3 when sampling at various capillary-to-tissue distances

Cell death incurred in the CA3 from electroosmotic sampling of the CA3 region of an OHSC at various capillary-to-tissue distances. Data is obtained from sampling with a 200 μm collection capillary i.d. As a general trend, cell death is greater when the capillary-to-tissue distance is shorter. All mean values for damage at similar power values above 20 μW are significantly different from each other ($p<0.05$).

There is excessive damage when the collection capillary is in direct contact with the tissue surface, and Figure 11 reveals that it is likely due to increased power dissipated within the tissue. The electric field strength decays rapidly outside the capillary, and when the capillary is raised off the tissue, most of this decay occurs in the HBSS layer. However, when directly in

contact, the tissue experiences the strong electric field at the capillary lumen. There is a drastic decrease in damage between 0 and 50 μm capillary-to-tissue distance with diminishing effects as the capillary-to-tissue distance is increased further. This fact shows that raising the collection capillary off the tissue, even if just a little bit, is instrumental in preventing damage.

This damage may also be due pressure effects. A mismatch between the zeta potential of the tissue (~ -22 mV)[53, 61] and the capillary (-50 mV) induces some pressure-driven flow. At the capillary lumen, the pressure is slightly negative and according to COMSOL results, exerts physical force on the surface of the tissue when the capillary-to-tissue distance is 0 μm. Thus the HBSS layer between the capillary and tissue is not only is a physiological buffer, but could serve as a physical buffer preventing the tissue from experiencing the electric field at the collection capillary lumen and increased pressure at the lumen of the collection capillary.

The trends presented here serve as guidelines for experimental design. The capillary-to-tissue distance values tested were quite large. In the interest of efficient and reproducible sampling, it is more convenient to sample at a shorter distance to avoid dilution of collected sample. Capillary placement via method 3 (barely touching the surface then retracting to the proper capillary-to-tissue distance) is also most efficient. Keeping in mind the trend that less than 20 μW dissipated results in minimal damage, a colleague attempted to sample (collect extracellular fluid in the capillary and analyze contents) using conditions that I predicted to be minimally damaging[54]. A 150 μm i.d. capillary was positioned using method 3 with a capillary-to-tissue distance of 15 μm. The power model shows that sampling under these conditions at applied fields of 46.6 and 50 V/cm should be safe with powers of 11.1 and 12.7 μW. The damage incurred when sampling at these conditions was $9.41 \times 10^{-4} \pm 7.89 \times 10^{-4}$ (SEM) and $1.32 \times 10^{-3} \pm 3.69 \times 10^{-4}$ respectively. These conditions were identical to those used by a colleague[54] to transport Leu-enkephalin (YGGFL) from the HBSS bath under the tissue up through the tissue where it is exposed to and hydrolyzed by outward facing ectopeptidases in the extracellular space. Intact YGGFL and hydrolysis product GGFL are sampled into the collection capillary, and contents were analyzed offline via HPLC. Figure 12 shows a sample chromatogram illustrating that YGGFL was passed through tissue when potential was applied, as no hydrolysis products are seen when sampling occurs simply through the insert membrane adjacent to the tissue.

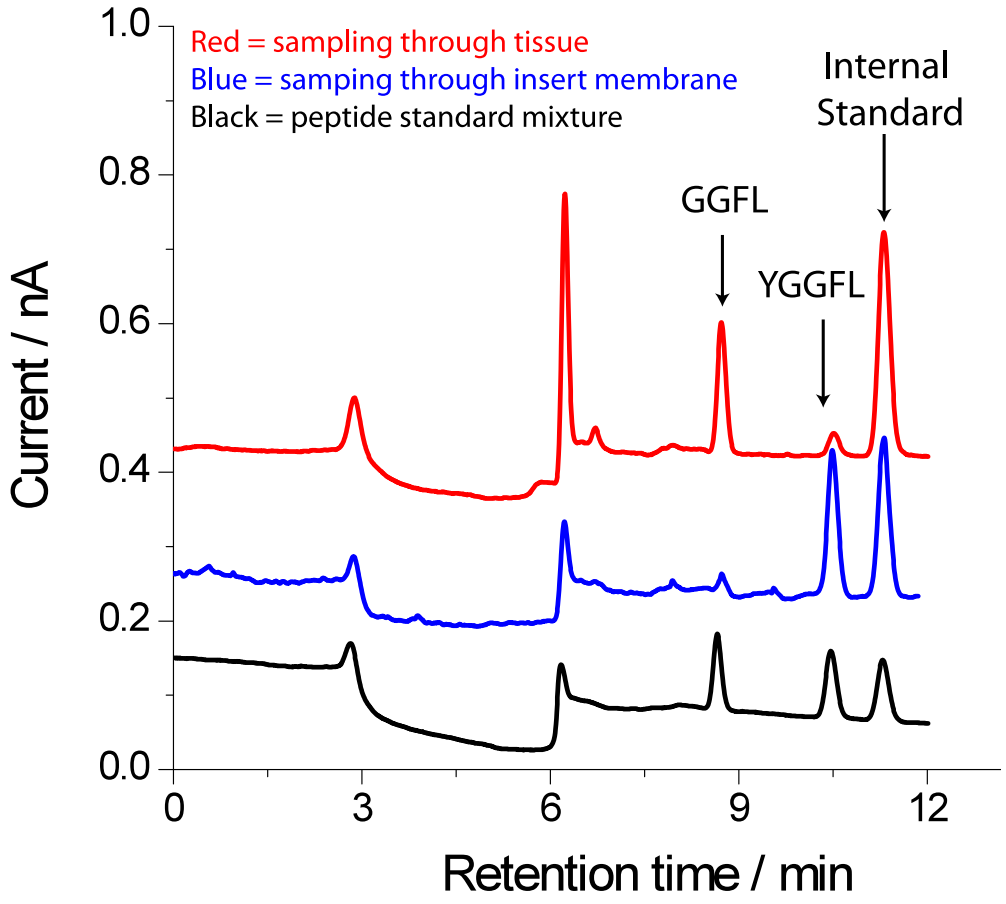

Figure 12. Chromatogram of samples obtained through single capillary electroosmotic sampling. YGGFL is dissolved in HBSS below the tissue. When sampling through the tissue (red trace), the concentration of YGGFL in the collected sample is decreased and the concentration of the hydrolysis product, GGFL, is increased, illustrating that sample went through the tissue was exposed to enzymes in the extracellular space. When sampling through the insert membrane (blue trace), this conversion does not happen. The black trace is a standard peptide mixture of YGGFL, GGFL, and an internal standard for flow rate variability.

Thus, with the help of the power model, conditions appropriate for minimizing cell death in a particular sampling experiment were established with the possibility of extending for additional parameters with additional experiments.

While power has emerged as the best descriptor of the cell death incurred from electroosmotic sampling, power is not directly controlled by experimental means. Since applied voltage is directly controlled in all experiments, it is more useful to dictate the conditions for

minimizing cell death in terms of this variable. A low capillary-to-tissue distance is desirable for sample collection. A larger capillary i.d. is desirable for larger sample volumes. We can call the damage that occurs when dissipated power is below 20 μW in Figure 9 as negligible, as it is very close to ‘0’.

3.3.2 Neuroprotective Side Effect of Small Electric Fields

As noted in 'Tissue Viability', Chapter 2, the cultures utilized in the earlier portion of this work suffered unexplainable neuronal degeneration of the CA1 and suprapyramidal blade of the DG (DG-SP). In some cases, this occurred prior to experimental use and the affected cultures were discarded as non-viable. However, there were instances where all cultures were deemed viable to sample, but PI staining revealed that the CA1 and DG areas of negative control cultures (no voltage applied) were quite damaged the next day. Interestingly, the CA1 and DG were not damaged in tissues that were sampled in the CA3. This trend is seen in Figure 13.

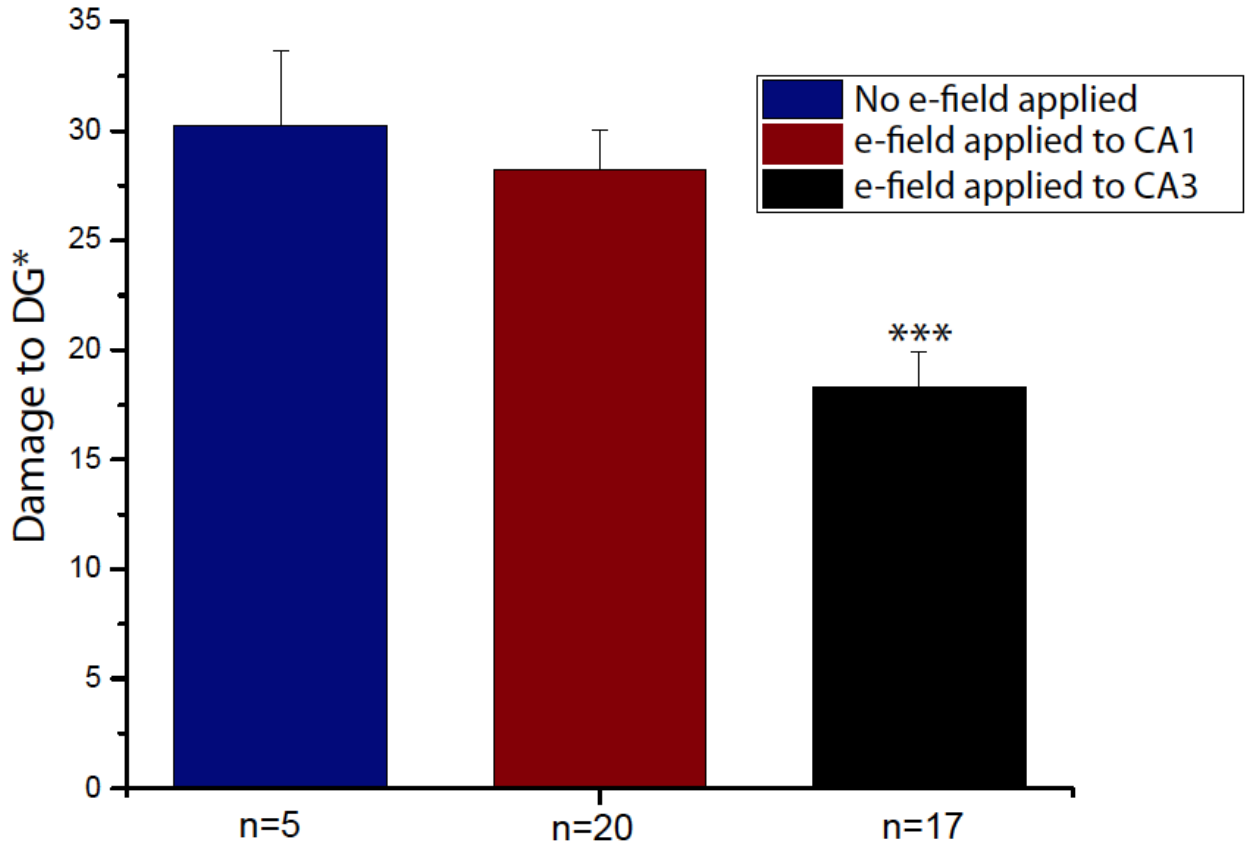

Figure 13. Decreased spontaneous cell death to the DG-SP after electroosmotic sampling

Damage was calculated in experimental tissues where sampling was performed in CA3, where it was performed in CA1, and in controls where the suprapyramidal blade of the DG had degenerated. All three groups had experienced spontaneous degeneration of the DG. Negative controls for all three groups were cultures that had not degenerated, from other batches of cultures and positive controls were MeOH-treated cultures.

Studies show that mild depolarizing electric fields may be neuroprotective to brain tissue[66], and we may be seeing evidence of that fact here as well. Figure 13 shows damage to the DG-SP for experimental tissues where sampling was performed in CA3, where it was performed in CA1, and in negative controls where the DG had degenerated. The fluorescence intensity ($I_{DGSP)}$ for the DG-SP each tissue type was found by drawing 5 equally sized regions of interests in the DG blade. The fluorescence intensity was found for negative controls in non-degenerated cultures, in other batches (I_{NC}) and in positive, MeOH treated tissues (I_{PC}). Damage was calculated according to Equation 3.

$$\frac{I_{DGSP}-I_{NC}}{I_{PC}-I_{NC}} \times 100 \quad (3)$$

The DG damage in control cultures that did suffer damage (30.23±3.45%) was compared to those where voltage was applied to the CA1 area (28.22±1.83%) and where voltage was applied to the CA3 area (18.23±1.62%). Damage was significantly prevented in the DG-SP when voltage was applied to the CA3, but not the CA1.

3.4 CONCLUSION

We successfully established a power threshold in the CA1 and CA3 regions in an OHSC for single capillary electroosmotic sampling. This information was intended to have predictive power for conditions not actually tested as well as future electroosmotic sampling designs. The definition of 'safe' ultimately comes down to the nature of the experiment. When measuring the chemical properties of the extracellular space (e.g., the determination of ectoenzyme activity, binding of antibodies to extracellular epitopes, chemical reactions with elements of the extracellular matrix, etc.), the fact that a cell is dead the following day may not be important. On the other hand, if a culture is to survive and be used again in the future for subsequent studies, minimizing damage is critical.

The single capillary electroosmotic sampling approach in its current form could be used for *in vivo* sampling near the surface of the brain, but not for deeper structures. However, it is an important first step towards developing a sophisticated sampling method for acute and cultured cultures. While applicability to other cultures remains to be established, it is very likely that all cultures have a negative ζ-potential, and therefore this sampling technique would be useful for acquiring samples from them. The key finding is that electrokinetic flow in brain tissue can be used to sample the extracellular space, and that cell death can be immeasurably small.

4.0 PUSH-PULL ELECTROOSMOTIC SAMPLING

4.1 INTRODUCTION

The previous chapter illustrated the use of single capillary electroosmotic sampling for both the extraction of extracellular fluid from living brain tissue as well as using it as a method for studying various reactions catalyzed by membrane-bound, outward-facing enzymes (ectoenzymes) in the brain[54, 67]. However, the spatial resolution is poor and introducing material to the tissue by the bath under the tissue is inefficient and wasteful, particularly if the material is expensive. We created an improved model based on push-pull perfusion. We contrast single capillary electroosmotic sampling in Figure 14, panel A, to push-pull electroosmotic sampling, in panel B. Panel B shows a close up of the fluid flow dynamics at the push-pull sampling site while panel C shows the full experimental design. A 'push' source capillary with a tapered tip (i.d. 15-30 μm) is inserted into the tissue and a 'pull' collection capillary (i.d. 50-150 μm) is in contact with surface of the tissue close by. Applying a voltage across the capillaries and tissue drives fluid from the source capillary into the tissue and then into the collection capillary. The sampling site is essentially limited to the area between the two capillaries. The electric field/current is the primary concern when minimizing damage to the tissue. No damage is seen from insertion of the source capillary into the tissue without application of field. The push-pull design adds versatility over the single capillary model, as material can be introduced into the tissue by the source capillary rather than by the bath underneath.

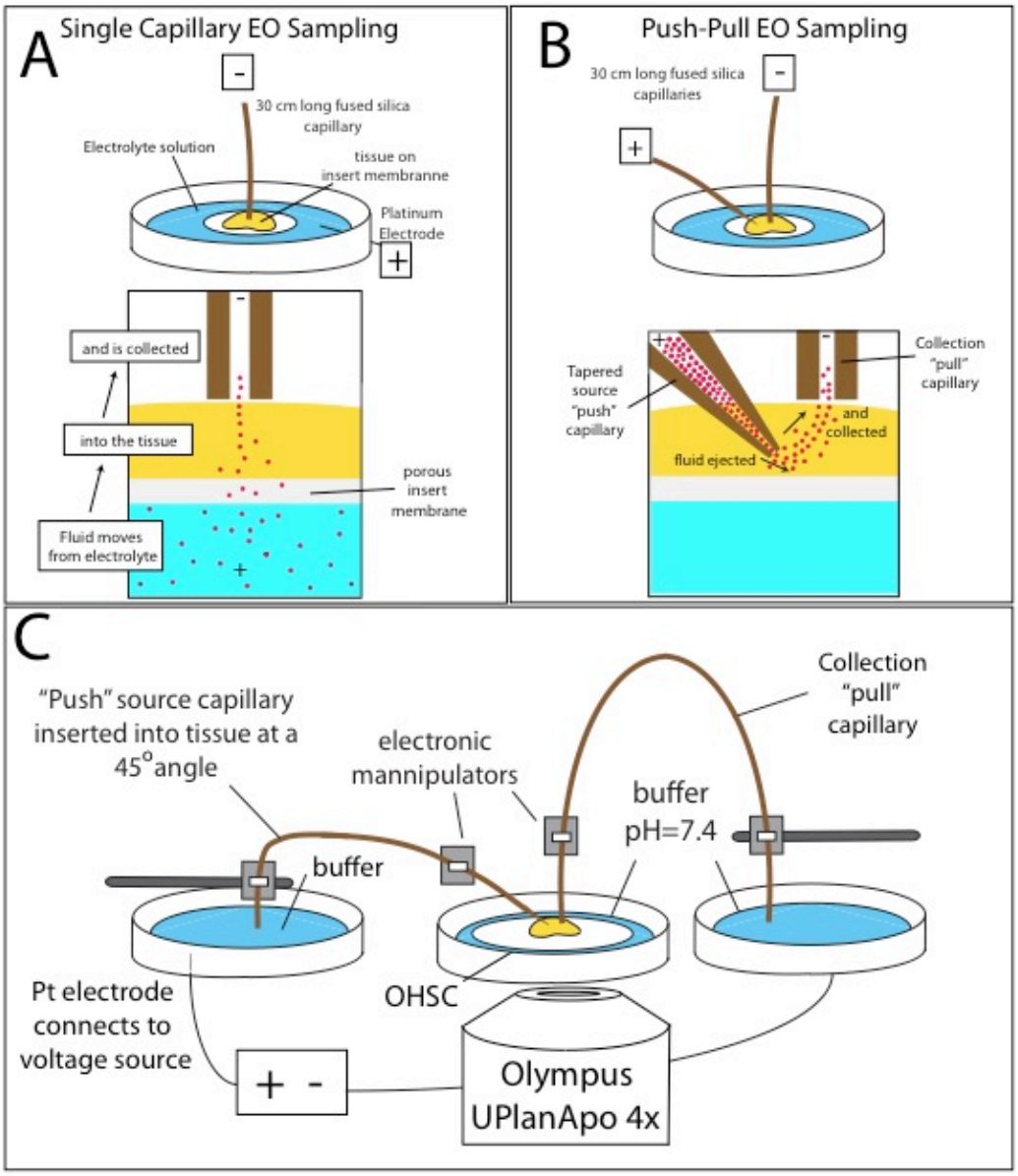

Figure 14. Push-pull electroosmotic sampling

A potential difference is applied to a pair of electrodes causing current flow and electroosmotic flow. (A) In single capillary electroosmotic sampling, electroosmotic flow originates in the buffer under the membrane to the capillary. (B) In push-pull electroosmotic sampling, electroosmotic flow (and current) pass from the tapered source capillary to the collection capillary. (C) Shows the entire push-pull electroosmotic sampling design. A 30 cm long fused-silica capillary held in place by two micromanipulators connects a buffer filled reservoir with the surface of an OHSC cultured on a PTFE Biopore membrane (0.45 μm pore size). A pulled fused-silica capillary at is also held at a 45° angle by two micromanipulators connecting a buffer filled reservoir to the OHSC. Two platinum electrodes connect each buffer reservoir to a voltage source. When voltage is switched on with the indicated polarity, electroosmotic flow will flow from the source to the collection capillary.

All sampling techniques are capable of damaging the sampled tissue[20, 68]. In the last chapter, we assessed the damage caused by the single capillary technique using propidium iodide (PI). We found that the diameter of the capillary and the applied voltage both influenced the extent of damage. We carried out similar experiments for push-pull electroosmotic sampling, examining a variety of sampling parameters to find those suitable for minimizing damage. As neurons respond to electric fields, we also sought to minimize depolarization of transmembrane potential, with attention to preventing action potential. We calculated flow rates by HPLC quantification of a peptide internal standard that passed from source to collection capillary during push-pull electroosmotic sampling.

4.2 EXPERIMENTAL

4.2.1 Solution and Reagents

Culturing medium and solutions used in dissections are the same as used previously in 'Solutions and Reagents', Chapter 2. Texas red dextran conjugate, 3 kDa (TR3) solutions were prepared by dissolving solid TR3 (Sigma-Aldrich, St. Louis, MO, USA) in Hank's balanced salt solution (HBSS, Sigma-Aldrich) at a final concentration of 1-3 μM. Solutions are filtered through a 0.45 mm PTFE syringe filter and frozen until use. The sampling internal standard, $^{D}Y^{D}AG^{D}F^{D}L$, was prepared with D-amino acids by the Peptide Synthesis Core at the University of Pittsburgh (Pittsburgh, PA, USA). Solutions of internal standard were prepared by dissolving solid peptide in HBSS at a final concentration of 8-12 mM and frozen until use. An HPLC-injection standard, GGFL, was prepared by dissolving solid GGFL in 0.1% TFA at a final concentration of 3.8 mM. Fresh solutions were prepared from this stock solution by further diluting in 0.1% TFA for a final concentration of 2-15 μM. HPLC mobile phases were prepared with acetonitrile (Sigma) and HPLC-grade water (Sigma) with 0.05% TFA (Sigma). HPLC samples were diluted in an aqueous solution containing 0.1% TFA and GGFL.

4.2.2 General Sampling Procedure

Here, as was the case when studying single capillary electroosmotic sampling, when the focus of the experiment is on studying damage to the tissue, no actual sample was collected. Sampling – collecting extracellular fluid followed by analysis – was only performed when measuring flow rates by HPLC.

In order to prepare to begin sampling, the source and collection capillaries must be prepared, mounted, filled, and positioned.

Preparation and Mounting: Both capillaries were made of fused silica. The collection capillary, with i.d. varying from 50-150 μm was cut to with a clean, straight end to 30 cm using the Shortix capillary cutter. The source capillary was prepared by pulling capillaries of 200 μm i.d. to a bee-stinger-type tip using a capillary puller (Model P-2000, Sutter Instruments, Inc., Novato, CA). A razor blade was used to trim off the bee-stinger tip to create the desired tip diameter (15-30 μm). This process was monitored by visualization under bright field with an IX-71 inverted microscope from Olympus with a 4x objective, using SimplePCI acquisition software. Figure 15 shows a bee-stinger capillary prior to and after the trimming procedure.

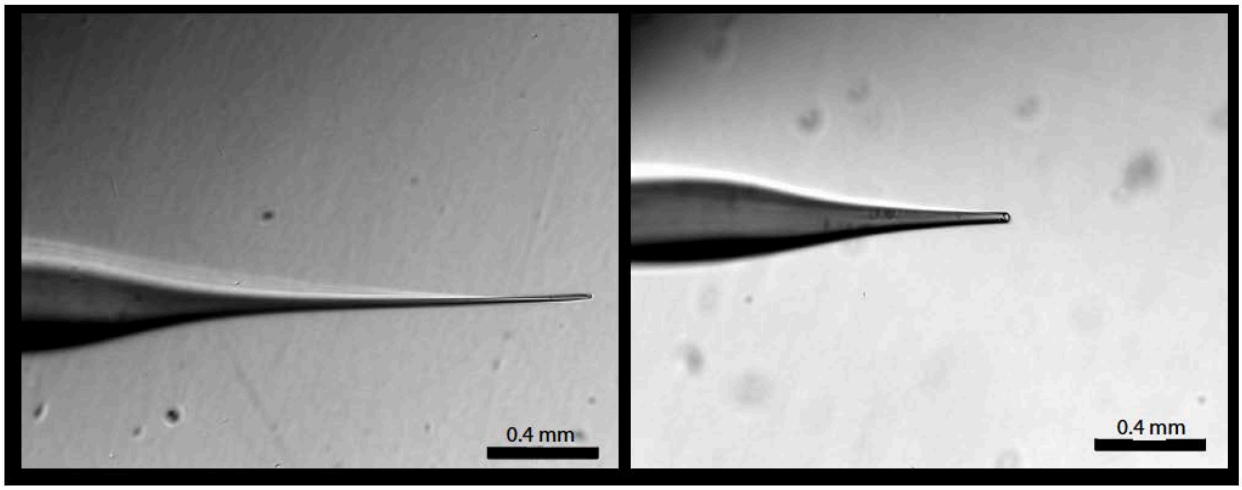

Figure 15. Pulled fused silica capillary before and after trimming procedure

Both collection and source capillaries were mounted on a microscope stage on electronic micromanipulators (Model MP-285, Sutter Instruments, Inc.). These manipulators allowed precise control of the sampling and source lumen in and around the tissue surface. A manual

manipulator held the opposite ends of each capillary in two HBSS-filled dishes. The collection capillary was mounted perpendicular to and the source capillary at a 45º angle to the microscope stage.

Filling: The collection capillary was filled with HBSS from the proximal end with a syringe. The source capillary is most effectively filled by applying a negative pressure to the non-tapered end while the pulled tip is submerged in filtered HBSS.

Positioning: Each capillary cast a shadow on the tissue which were used to guid the placement of the capillaries. The shadows of each capillary were monitored using bright field (xenon lamp) illumination.

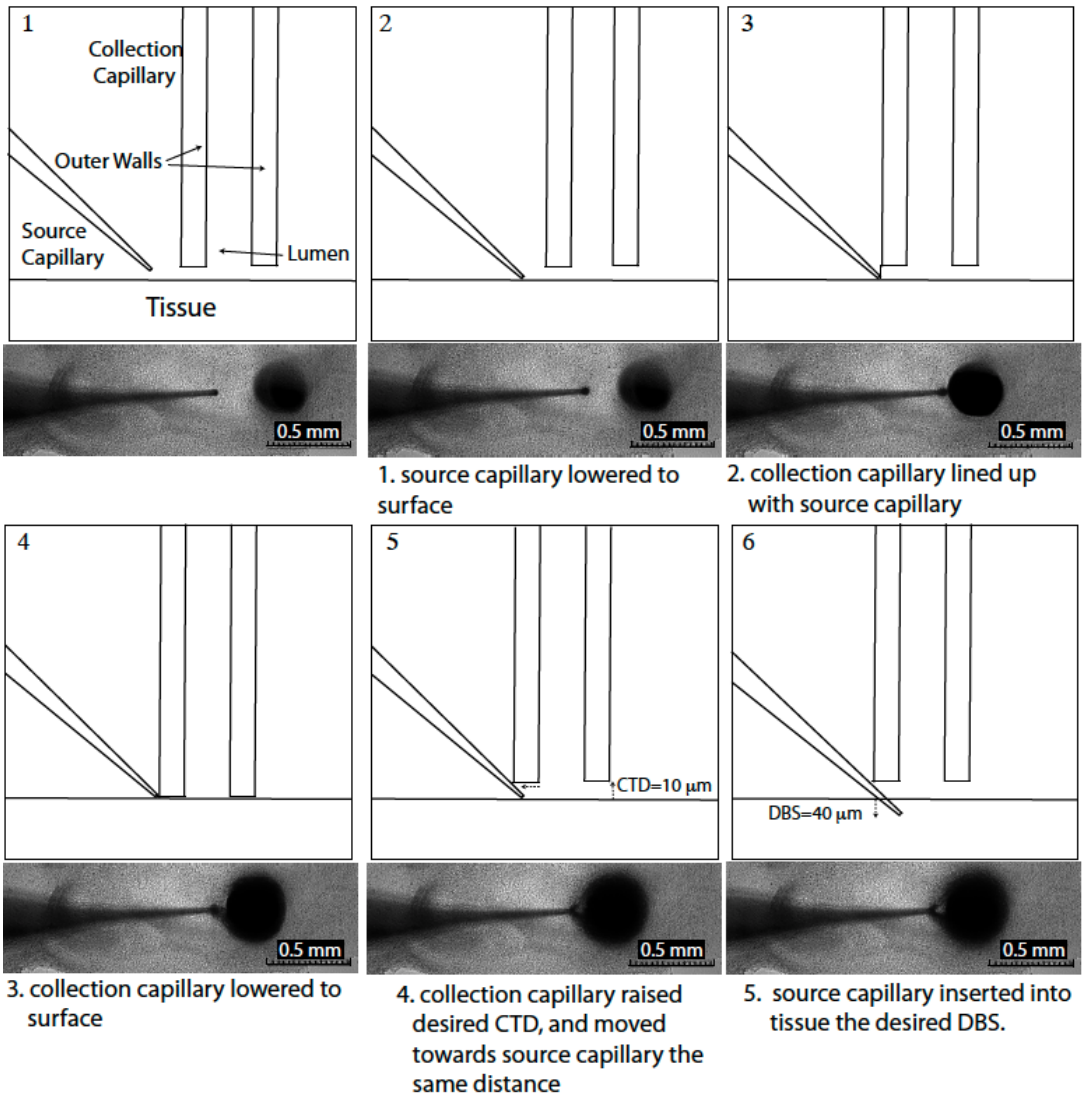

Figure 16. Positioning source and collection capillaries

Capillary positioning with sketches of the view from the side (top portion of each panel) and micrographs of what is seen as capillaries are positioned (bottom portion of each pane (1) Capillaries trimmed, filled, above the surface. (2) The source capillary was lowered on a 45° angle to the surface of the tissue until it just touched the tissue. (3) The collection capillary is lowered to the point where its circular shadow has crisp edges. The edge of the middle of shadow was lined up and abuts the source capillary lumen where it had touched the tissue surface. (4) The collection capillary was lowered until it just barely touched the surface. At this point, the edge of the tapered tip and the center of the outside edge of the collection capillary lumen are just barely touching each other and the surface of the tissue. (5) The collection capillary is raised a desired distance (the capillary-to-tissue distance, CTD) and then moved towards the source capillary that same distance (this latter move was first designed to keep the capillaries as close as possible, and retained for all sampling to keep a standard procedure.) (6) The source capillary is inserted into the tissue a desired distance (distance beneath surface, DBS).

The distance between the capillaries can be calculated geometrically, according to Figure 17.

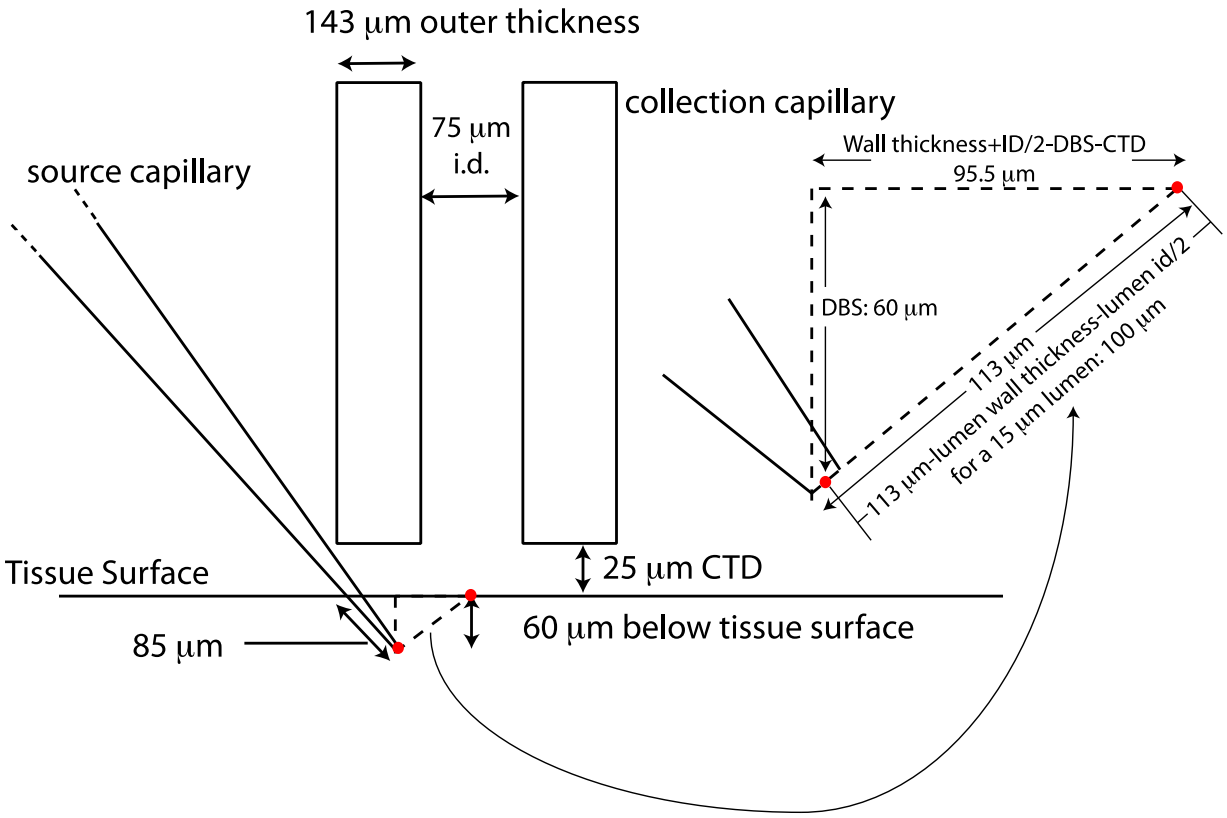

Figure 17. Geometry of capillary placement in push-pull electroosmotic sampling

The source capillary (barrel i.d. 200 μm) is inserted at a 45° angle with the tip 60 μm below the tissue surface. The collection capillary (75 μm i.d.) is situated 25 μm above the tissue surface (CTD). The central axis of the source capillary is at a 45° angle from the tissue surface. The distance between the middle of the source tip and the middle of the tissue surface under the center of the collection lumen (indicated by red dots) can be calculated by the calculations shown in the enlarged triangle. The lumen wall thickness is assumed to be in the same proportions of the barrel i.d. to the barrel wall thickness.

Platinum electrodes connect each HBSS-filled dish at each capillary distal end to a high voltage source (model PS350 from Stanford Research Systems (Sunnyvale, CA, USA)). Once the capillaries were positioned, the voltage was turned on and sampling commenced.

4.2.3 Quantifying Flow Rate

Two molecules were used to track electroosmotic flow between capillaries. The source capillary was filled with a solution containing a 3 kDa Texas Red dextran conjugate (TR3) and 27.25 mM

^{D}Y^{D}AG^{D}F^{D}L internal standard. Capillaries were positioned as described above. The SimplePCI acquisition software was programmed to capture one image every second. After 5-10 frames were captured, the voltage was switched on to begin sampling. TR3 was detected using the same cube/filter settings as those used to detect PI fluorescence. Exposure times were optimized after the first few sampling runs to minimize over exposure of the images captured.

4.2.3.1 Visualizing fluid movement

As sampling proceeds, TR3 leaves the source, moves through the tissue and is collected. Figure 18 shows a series of images illustrating the movement of TR3 from source to collection capillary. As the lumen of the collection capillary fills with TR3, its location becomes apparent.

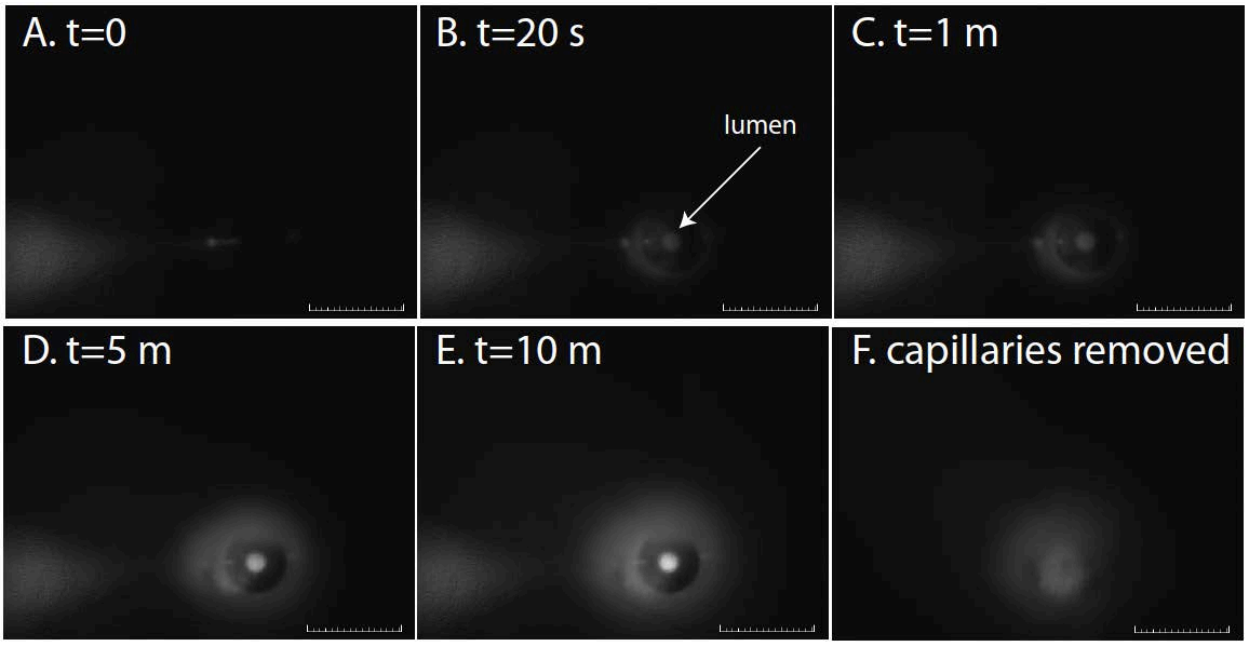

Figure 18. Time-lapsed images of TR3 fluorescence of sampling

Capillary arrangement is identical to that seen in Figure 16. The applied field is 6.66 V/cm with an induced current of 13 μA. Each panel A-E shows TR3 accumulating in the collection capillary lumen as sampling proceeds. After capillaries are removed from tissue (F), some fluorescence remains, but that in the lumen is no longer visible, indicating TR3 was collected in the capillary. Scale bars = 0.5 mm.

SimplePCI was used to draw a region of interest around collection capillary lumen to measure ‘mean grey’ which is a measure of fluorescence intensity in the region of interest to measure of TR3 accumulation in the capillary versus time.

4.2.3.2 Quantifying electroosmotic flow with a peptide internal standard

Two to three insert membranes (4-6 tissues) were removed at a time for sampling. Tissues remained outside of the incubator for no longer than forty minutes before sampling. After 10 minutes of sampling, the contents of the collection capillary were pushed by an air-filled syringe into a vial containing 10 μL 0.1% TFA and 9.5 μM GGFL. Samples were injected onto an HPLC (Ultimate 3000 Nano LC system, Thermo Fisher Scientific) within 5 minutes of the end of sampling. In the process of optimizing the system for efficient and effective analysis, two programs were used. Earlier experiments used a microliter pick-up program, where 3 μL of sample was injected and pre-concentrated on a trap column (75 μm x 2 cm, C18, 3 μm, 100 Å) for 5 minutes at 5 μL/min with a 1% acetonitrile/0.05% TFA. Samples were separated on an analytical column (75 μm x 15 cm, C18, 2 μm, 100 Å) using a gradient elution at a flow rate of 300 nL/min. Later separations were accomplished through injection of 1 μL of sample onto the trap column, which was directly inline with the analytical column. Samples were separated by gradient elution at 300 nL/min. $^{D}Y^{D}AG^{D}F^{D}L$ calibration standards were prepared by diluting 10 μL of the source capillary fill solution (27.25 mM $^{D}Y^{D}AG^{D}F^{D}L$ + TR3) to 1 mL in 0.1% TFA and then further diluting down with 0.1% TFA to make standards ranging from 1 μM to 30 μM $Y^{D}AG^{D}F^{D}L$. Each standard also contained 6.65 μM GGFL to account for variability in auto sampler injection volume (this will be discussed shortly).

Each chromatogram contained two peaks of interest when quantifying flow rate. Figure 19 shows a typical chromatogram with GGFL and internal standard peaks identified. All fill solutions contained a third peptide (galanin, unmarked in), which will be discussed and become relevant in Chapter 5.

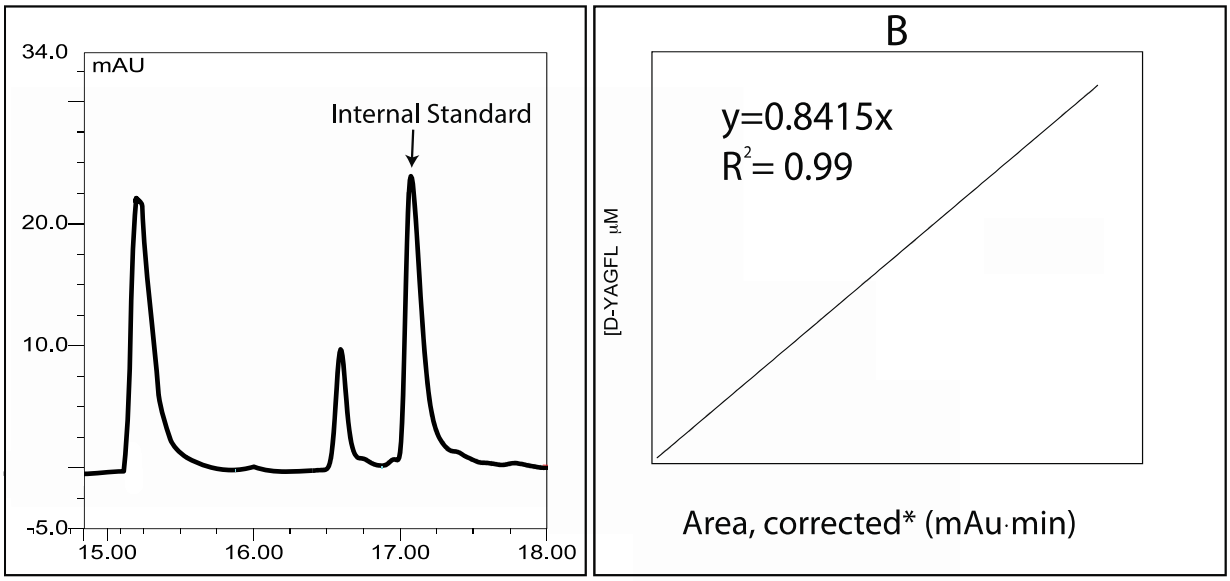

Figure 19. Chromatogram of $^{D}Y^{D}AG^{D}F^{D}L$ internal standard and GGFL separation

(A) GGFL was used as an injection standard and was included in the solution into which the sample was put. An all D-amino acid internal standard was used as a marker for flow rate, as enzymes in the tissue cannot hydrolyze this peptide. The unmarked peak is galanin, and will be addressed in Chapter 5. (B) Calibration curve for the internal standard.

GGFL eluted first followed by the internal standard. The internal standard peak area was corrected for variability in injection volumes by multiplying the peak area of internal standard (A_{IS}) by the average peak area of GGFL ($A_{GGFL,\ AVG}$) from all runs and dividing by the GGFL peak area in the run of interest (A_{GGFL}), according to Equation 4.

$$Area_{corrected} = A_{IS}\frac{A_{GGFL,AVG}}{A_{GGFL}} \quad (4)$$

All peaks in all chromatograms, both sample and calibration standards, were treated in this way. Calibration curves for galanin and internal standard were constructed by plotting the peak area versus the concentration of analyte in the standard and fitting a linear regression to the data, shown in the inset of Figure 19. All fitted lines were forced to go through the origin. The internal standard concentration in each injected sample ($[IS]_{sample}$) was determined by the regression equation. These values were then divided by the total sample volume (10 μL diluent ($V_{diluent}$) + 2.36 μL in a 100 μm i.d. collection capillary ($V_{capillary}$)) to find number of moles of analyte collected in the capillary ($moles_{IS}$). Equation 5 shows this calculation.

$$Moles_{IS} = [IS]_{sample} \times \left(V_{capillary} + V_{diluent}\right) \quad (5)$$

The volume of $^{D}Y^{D}AG^{D}F^{D}L$ internal standard collected (V_{IS}) was calculated by dividing the number of moles of internal standard collected by the initial concentration in the source capillary ($[IS]_{source}$) and the time sampled (t_s), shown in Equation 6.

$$V_{IS} = \frac{moles_{IS}}{[IS]_{source}} \quad (6)$$

Because the internal standard, $^{D}Y^{D}AG^{D}F^{D}L$, is small, neutral, and does not degrade in the extracellular space, the concentration of internal standard in the sample was used to calculate electroosmotic flow rate from source to collection capillary. Equation 6 calculates the volume of source fill solution that traveled to and was captured by the collection capillary in a certain amount of sampling time.

4.2.4 Minimizing Tissue Damage

The viability of all cultures was checked prior to sampling identically to procedures outlined in 'Assessment of Viability', Chapter 3. After imaging, all cultures were then returned to the incubator during further preparation for sampling.

Two or three insert membranes (4-6 tissues) were removed at a time from the incubator for experiments. All viable OHSCs were sampled before the plate was returned to the incubator. OHSCs remained outside the incubator for approximately 1.5 hours. In any given 6-well plate, at least two cultures were not sampled to serve as live (negative) controls. Two other cultures were also not sampled and were treated with MeOH to serve as positive controls. Capillary-to-tissue distance values ranged from 15-50 μm and the source capillary was inserted into the tissue either 40 or 60 μm. With these parameters, the distance between the center of the source lumen to the tissue surface under the center of the sampling lumen ranged from 100-150 μm. Applied voltage ranged from 100-900 V and was applied for 5 minutes. After sampling one location in a tissue, the voltage was shut off, the capillaries were removed, and sampling proceeded to the next tissue. After sampling all the desired cultures in a 6-well plate, all sampled tissue, two negative controls, and two positive controls (MeOH-treated) were treated with PI overnight. The next day, medium was exchanged for HBSS buffer solution for imaging. Imaging was done in the same fashion as screening prior to sampling, using the IX-71 inverted fluorescence microscope with a 4x objective, setting the exposure time to the lowest of the auto exposure times of the two

MeOH-treated cultures. Figure 20 shows representative fluorescence images of these tissue types stained with propidium iodide.

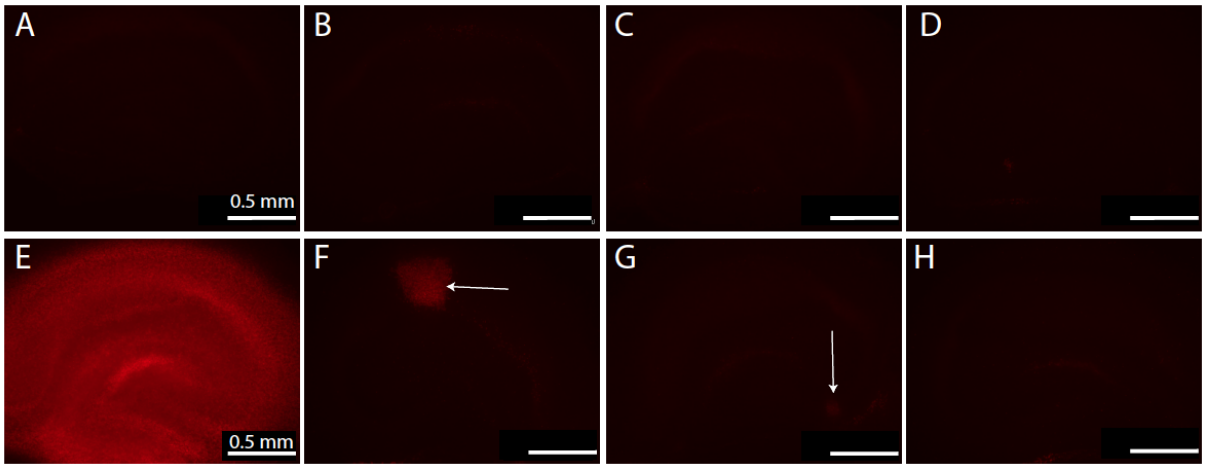

Figure 20. PI-stained OHSC images following push-pull electroosmotic sampling

Scale bars = 0.5 mm. (A) Negative control; (B)-(D) are the CA1, CA3, and infrapyramidal blade of the dentate gyrus (DG-IP) of the dentate gyrus (DG), respectively, sampled at 300 V using a 200 µm i.d. capillary pulled to 25 µm, inserted 60 µm below the surface and collected with a 75 µm i.d. capillary 25 µm above the surface of the tissue for 5 minutes. (E) MeOH-treated tissue (positive control). (F) – (H) are the CA1, CA3, and DG-IP, respectively sampled in the same geometry and time as (B)-(D) but at 500 V. Arrows in (F) and (G) point to areas of tissue damage.

Total damage was calculated the same as single capillary electroosmotic sampling ('Quantifying Tissue Damage', Chapter 3). Damage studies for push-pull electroosmotic sampling were primarily done in the CA3 region.

4.2.5 Preventing Action Potential – Calcium Imaging

A loading solution was prepared by mixing equal volumes of 20% pluronic acid and 1 mM Fluo-4, AM. HBSS buffer solution was then added to bring the final concentration of Fluo-4 AM to 5 µM (and pluronic acid to 0.1%). Pre-mixing the dye and the pluronic acid before adding HBSS increases the solubility of the dye and facilitates loading into the cells. The medium below each insert membrane containing cultures was replaced with 1 mL of the Fluo-4 AM loading solution. One milliliter of loading solution was also placed on top of the inserts/cultures. Slices were incubated at 36.5ºC, 5% CO2 for 90 minutes. All loading solution was then aspirated out and

replaced with pre-warmed (37ºC) HBSS buffer solution, placing 1 mL above and 1 mL below each insert membrane. Cultures were incubated in this rinsing solution for 15 minutes. Rinsing HBSS was then aspirated away and 1.2 mL of HBSS was put below the insert membrane. After incubation for 15 more minutes, HBSS was exchanged once more for fresh, warmed HBSS, and the cultures were removed from the incubator for experimental use. Sampling set-up and capillary placement occurred in the same way as in 4.2.2. General Sampling Procedure. The source capillary barrel was 200 μm i.d. pulled to a 20 μm tip inserted at a depth of 60 μm. The collection capillary was 75 μm i.d. and the capillary-to-tissue distance was 25 μm. Fluo-4 fluorescence was visualized during sampling on the IX-71 microscope using a 4x objective lens, a 494 nm excitation filter (FF01-494/20-25, from Semrock, Lake Forest, IL) with the dichroic mirror and 535 nm emission filter from the U-MWIBA2 filter set (Olympus).

After the capillaries were situated and the voltage was turned on, a wave of increased fluorescence was sometimes observed. This wave, if present, always originated at the source capillary. Sometimes there was no increase in fluorescence following application of the voltage to the tissue. In both cases, after the first calcium response finished or when no response was seen, the collection capillary was then moved over the tissue to attempt to invoke depolarization in other locations, stopping periodically to let the capillary sit in a single location for a few seconds. The source capillary remained at its original location. Second waves never originated at the source capillary. However, in some cases waves did occur near the collection capillary. Assessing a response under the collection capillary is more difficult because the fluorescence image is altered by the presence of the capillary. This is why the collection capillary had to be moved -- to see fluorescence under it. If calcium influx was seen as originating from the source at any time (which only occurred if there was no response immediately upon application of the voltage), the collection capillary was stopped to allow that depolarization event to conclude. Each region in each tissue was swept completely by the collection capillary to attempt to evoke action potential and calcium influx; this process took at least 4 minutes.

To ensure a negative response was not due to poor dye loading, a high voltage was always applied after the lower voltage was investigated. A response at a higher voltage indicated proper dye loading.

4.2.6 Finite Element Modeling

As in single capillary electroosmotic sampling, we used COMSOL (v. 4.3) to model push-pull electroosmotic sampling. A 2D sketch of the devised model is shown in panel A of Figure 21. Panel B of Figure 21 shows the model as seen in the 3D COMSOL space. We used three different physics modules. Numerical solutions of the Laplace equation were used to calculate the electric field distributions and voltage values within the model (Electric Currents). A modified Brinkman equation (see Appendix B: 'Discussion of Equations used in Comsol' for modifications) was used to model electroosmotic flow (Free and Porous Media Flow). Both modules were solved first as stationary or steady state equations. Tables 1 and 2 list relevant boundary conditions and properties of the material that makes up each subdomain listed in Figure 21. For a discussion of the equations used and justification of constants in Table 1, see Appendix B: 'Discussion of Equations Used in COMSOL'.

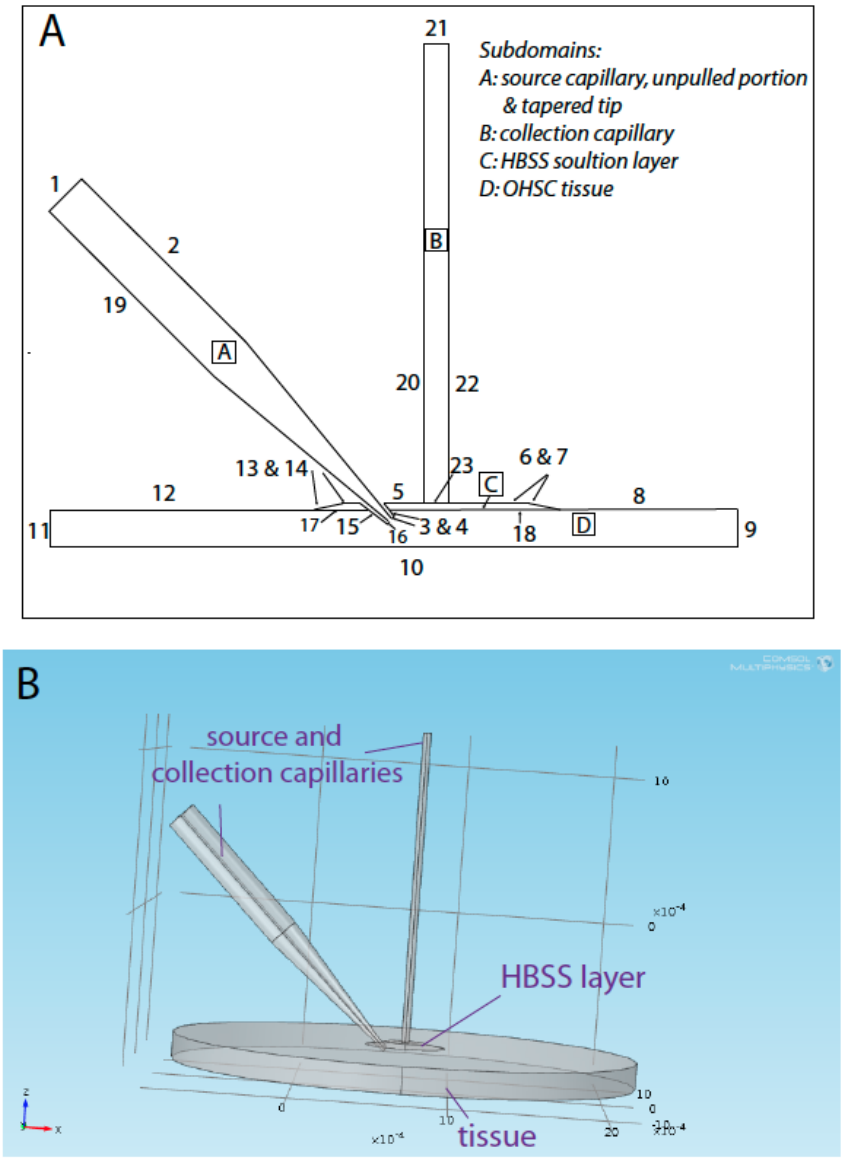

Figure 21. COMSOL model of push-pull electroosmotic sampling design

(A) Schematic of the model. This model was constructed with shortened capillaries (1 mm, subdomains A and C) of the correct ID that represent the full-length capillaries. The pulled tip of the source capillary is 1 mm and is inserted into the tissue at a 45° angle, measured from the tissue surface to central axis of the capillary (not shown). The thickness of the HBSS buffer layer is as thick as the experimental capillary-to-tissue distance and is represented as a truncated cone to avoid sharp corners where it meets the tissue surface. The tissue is represented by a disk of thickness is 168.5 μm with the capillaries placed in the center. The distance of the collection capillary from the source capillary is calculated mathematically according to the logic presented in Figure 18. Table 1 and 2 show the subdomain and boundary conditions specified in the model. The single capillary COMSOL model included two additional domains: the insert membrane and the buffer solution in which the insert membrane sat. These subdomains are not included here because they are not part of the current or fluid path and make the model more complex than necessary. (B) shows a 3-D representation in the COMSOL workspace.

Property	Meaning	HBSS	Tissue
σ^*	Conductivity	1.43 S/m	0.292 S/m*
ϵ	Porosity	1	0.41
τ (λ^2)	Tortuosity	1	1.39
K	Permeability*	1	$3.99\text{x}10^{-13}\text{m}^2$
ε_w	Permittivity	$7.1\text{x}10^{-10}$ F/m	
η	Viscosity	$8.9\text{x}10^{-4}\ Pa \cdot s$	
ζ	Zeta potential	0	- 21.3 mV
ρ_{eff}	Effective Charge Density	0	9.29 C/m3*

*Justification in Appendix B

Table 1. Material properties of HBSS and tissue for use in the COMSOL model of sampling

Boundary	Condition in 'Electric Currents'	Condition in 'Free and Porous Media'
1	Ground	Inlet
2-6, 14-16, 19, 20, 22	Insulation	Velocity, moving wall $V_x = \frac{\varepsilon_w \zeta_{wall}}{\eta} \cdot \vec{E}_x$ $V_y = \frac{\varepsilon_w \zeta_{wall}}{\eta} \cdot \vec{E}_y$ $V_z = \frac{\varepsilon_w \zeta_{wall}}{\eta} \cdot \vec{E}_z$ ζ_{wall} =-50 mV
7-13	Insulation	Wall, no slip
17, 18, 23	Continuity	Continuity
21	J_o	Outlet

Table 2. Boundary conditions of the push-pull electroosmotic sampling COSMOL model

$\vec{E}_x$, $\vec{E}_y$, and $\vec{E}_z$ represent the electric field in the x, y, and z directions respectively, calculated by the Electric Currents module.

Two models of flow rate can be calculated. In 'Free and Porous Media', electroosmotic volume flow is calculated on a surface by integrating the flux (m^3/s) at the surface that interfaces between the collection capillary and the plug of HBSS between the collection capillary and the tissue.

4.3 RESULTS AND DISCUSSION

4.3.1 Quantifying Flow Rate

Before experimental results are discussed, we estimate flow rate based on Equation 7 and 8.

$$\vec{E} = {}^{J}/_{\sigma} \quad (7)$$

$$V_{eo} = \vec{E}\mu_{total} \quad (8)$$

$\vec{E}$ is the electric field, J is current density, V_{eo} is the electroosmotic velocity, and μ_{total} is the sum of electroosmotic and electrophoretic mobilities. σ is conductivity. We solve Equation 8 for electric field, substitute into Equation 7, along with the relationship $= {}^{i}/_{\pi r^2}$, where r is the radius of the cross-sectional area through which current is passing, to get Equation 9.

$$V_{eo} = \frac{i\mu_{total}}{\sigma\pi r^2} \quad (9)$$

Velocity is a one-dimensional value. To convert to 3D to get a volume flow rate (U_{eo}) we substitute in $U_{eo} = V_{eo}\pi r^2$ (volume flow rate is the velocity times the cross-sectional area) to get Equation 10.

$$U_{eo} = \frac{i\mu_{total}}{\sigma} \quad (10)$$

The total mobility is a summation of the electrophoretic (μ_{ep}) and electroosmotic mobilities ($\mu_{eo} = {}^{\varepsilon\zeta}/_{\eta}$) times a hindrance factor, f, which accounts for the size of the molecule. ε, ζ, and η are the permittivity of water, the zeta potential of the material, and the viscosity, respectively. The conductivity of HBSS is 1.43 S/m, the electroosmotic mobility of the tissue is 1.7×10^{-8} m^2/Vs, and the internal standard is small (500 Da) and uncharged, so we assume f is 1 and μ_{ep} is negligible. Flow rates are calculated as shown in Table 3, using the currents induced when sampling with a 100 μm i.d. collection capillary and a 200 μm i.d. source barrel. We have previously been reporting data with respect to different applied fields; however, current directly

dictates flow rate. Thus, data relating to flow rates will also be related to the current induced in the system.

Applied Field V/cm	Current (μA)	Flow Rate (nL/min)
3.33	7	4.99
5	11	7.84
6.66	13	9.27
8.33	16	11.4

Table 3. Mathematical estimation of flow rate in push-pull electroosmotic sampling

4.3.1.1 Measurements with TR3

Figure 22 shows ‘mean grey’ or average fluorescence intensity TR3 in the collection lumen plotted against sampling time for several different applied fields.

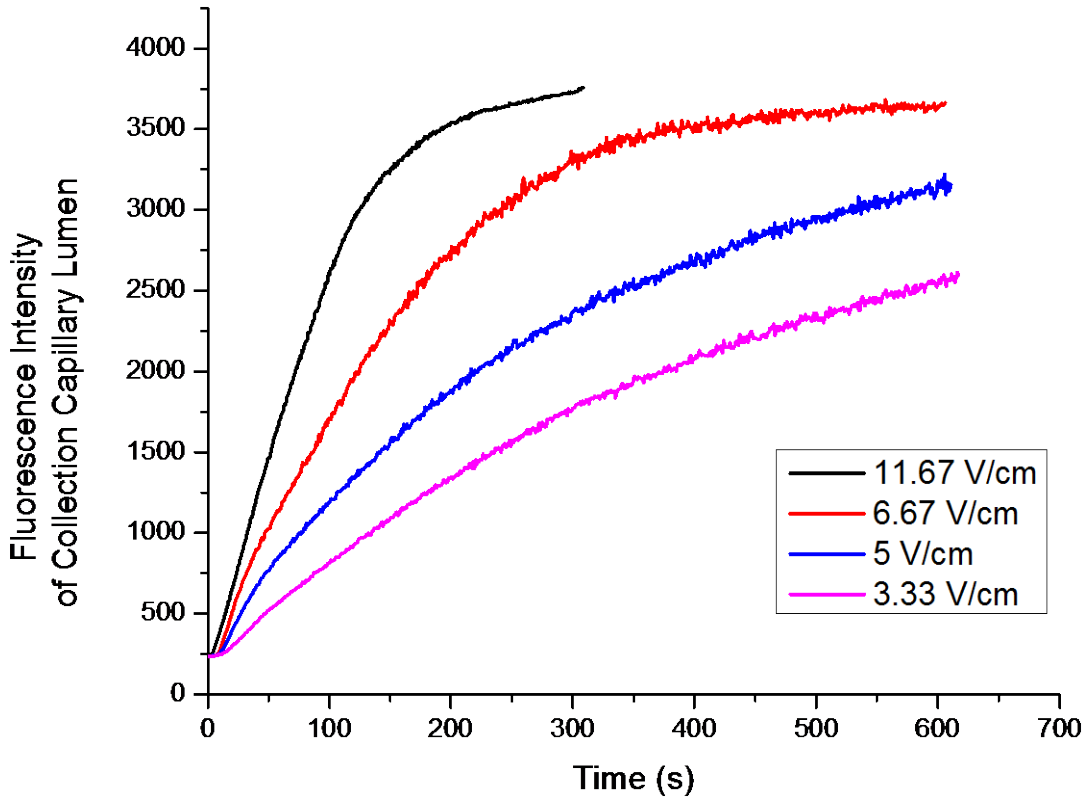

Figure 22. Fluorescence intensity of TR3 as it accumulates in the collection capillary over time

Plot of fluorescence intensity in the collection capillary vs. time for a variety of voltages applied using a 100 μm ID collection capillary and a 200 μm ID source capillary pulled to 20 μm. The first six frames (5.58 s) are baseline where no voltage has yet been applied. After the 6th frame captures, the voltage is immediately turned on and the fluorescence intensity is monitored in the lumen of the collection capillary.

As fluorescence intensity increases, particularly in the higher applied fields, the curve flattens. This falsely implies that flow rate decreases over time. In reality, the volume of TR3 increases linearly with time in the collection capillary. However, the optics of the microscope convolute reality into what is seen in Figure 22. This phenomenon is described in detail by Nicholson & Tao[69], who state that what is seen optically is a convolution of a square function (or linear increase with time) and a sinc function, which describes detection capabilities of a particular objective lens. In short, there is a discrete cylindrical zone centered at the focal plane where sensitivity decreases as vertical distance from the focal plane increases. The height of this zone depends on the particular objective lens. For the 4x air objective lens, this distance is 46

μm. If we fit curves like those seen in Figure 22 to curves predicted by the Nicholson Tao model (see 'Fitting Fluorescence Curves to Model' in Appendix C), we calculate sub-nL/min flow rates for the fields shown in Figure 22. In the next section, we discuss results derived from measuring peptide concentration in the collection capillary, where we calculate faster flow rates. The discontinuity between fitting the Nicholson Tao model to Figure 22 and experimental results has several potential origins. When the microscope objective lens is focused on the surface of the tissue, and the collection capillary is 25 μm above the surface, only 21 μm of the collection capillary lies in the detection zone. Under the tissue surface, TR3 can be detected to a depth of 46 μm, but the volume in the tissue that is 'filled' with TR3 is poorly defined, as is the area 'filled' in the 25 μm of HBSS solution above the tissue. Closer examination of Figure 18 shows that there is some optical distortion of the area around the lumen: when the capillary is in place, it seems void of TR3 fluorescence, but when capillaries are removed there is no such void. A 2D visualization from under the tissue helps verify fluid movement, helps identify if any aspect of sampling has gone awry, but does not give a complete picture of fluid flow dynamics in push-pull electroosmotic sampling.

4.3.1.2 Measurements with a Peptide Internal Standard

The volume of $^{D}Y^{D}AG^{D}F^{D}L$ collected during sampling with a variety of source capillary lumen sizes under a variety of applied fields is shown in Figure 23. The source barrel i.d. was 200 μm, the collection i.d. was 100 μm, the capillary-to-tissue distance was 25 μm, and the source tip was inserted into the tissue 60 μm. The fit shown is a linear regression for the points with a 20 μm source lumen. We calculate the total flow rate for these points using this size source lumen, but as COMSOL calculations will show, changing the source lumen will affect the flow rate slightly.

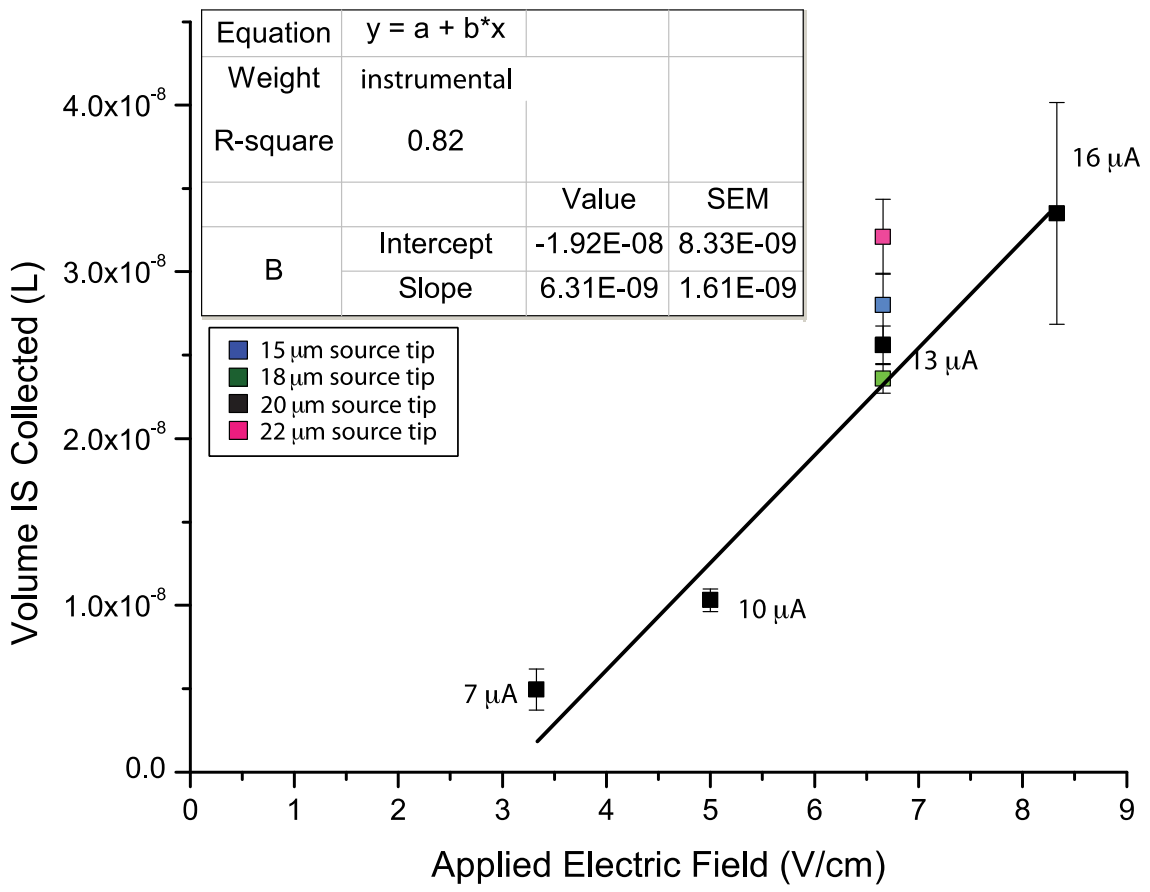

Figure 23. Volume of internal standard collected versus applied electric field

For all points, the source barrel i.d. was 200 μm, the collection i.d. was 100 μm, the CTD was 25 μm, and the DBS was 60 μm. Total n = 217. The regression fit with weighted error, calculated as the reciprocal of the square of the error of each individual data point.

Flow rates can be calculated by dividing the volume collected by the sampling time, 10 minutes. The total volume sampled is the volume of extracellular fluid drawn into the collection capillary plus the volume of internal standard collected. This is described by Equation 11, where the subscripts 'total', 'ECF', and 'IS' refer to the total volume sampled, the volume of extracellular fluid that's sampled, and the volume of internal standard that is collected. Equation 12 describes sampling in term of the applied electric field. The volume collected is directly proportional to the applied electric field and the time sampled.

$$V_{total} = V_{ECF} + V_{IS} \quad (11)$$

$$V_{total} = c\vec{E}t_s \quad (12)$$

We substitute Equation 12 into Equation 11 for V_{total} and rearrange to get Equation 13.

$$V_{IS} = c\vec{E}t_s - V_{ECF} \quad (13)$$

We fit Equation 13 to the linear regression in Figure 23 and find that constant, c, is the slope, 6.31×10^{-9} L $V^{-1}cm^{-1}$ and the collected volume of extracellular fluid is 19.2 nL. Dividing this constant by 10 sampling minutes gives a value - 6.31×10^{-10} L cm $V^{-1}min^{-1}$ – that when multiplied by the applied electric field will give the overall electroosmotic flow rate. Table 4 below calculates the overall flow rate for each of the conditions in Figure 23.

Applied Field (V/cm)	Flow Rate (nL/min)	Error (nL/min)
3.33	2.10	0.53
5	3.15	0.81
6.66	4.2	1.07
8.33	5.25	1.34

Table 4. Push-pull electroosmotic sampling rates calculated by HPLC analysis of samples

Flow rates are estimated by equation in Figure 23 and Equations 11-13, using a linear regression for the data in Figure 23 obtained with a 20 μm source capillary lumen.

The values shown in Table 4 are much lower than those predicted in Table 3. We attribute this to collection efficiency and loss of analyte (internal standard) by diffusion to the rest of the tissue.

4.3.1.3 Measurements through COMSOL modeling

We used COMSOL to calculate overall electroosmotic flow under when applying a variety of fields under a variety of sampling conditions. Figure 24 below shows how flow rate changes for various sampling parameters when holding either current or applied field constant. In the COMSOL model, we specify an applied field, scaled appropriately for the shortened capillaries, as the boundary condition of the collection capillary. However, calculating the total current in this shortened model required further calculations. The resistance of the each capillary component (full length, 30 cm collection, 29.9 cm source, 1 mm source tip) was calculated according to Appendix D: ‘A Simple Model of Resistance’. The resistance of the tissue/HBSS layer was found by determining the voltage drop between the source tip and the collection lumen and dividing by the current in the (shortened) model. The total voltage applied divided by the

total resistance, or the sum of each capillary resistance and the resistance of tissue and HBSS, gave the total current for the full system with 30 cm source and collection capillaries. In Figure 24, the blue bar in each cluster is 200 μm source barrel, 20 μm source lumen inserted 40 μm into the tissue (DBS). The collection capillary was 75 μm i.d., and was 25 μm above the surface of the tissue (CTD). The other bars represent changing that parameter to the dimension shown on the bar (in μm). The biggest change is seen when changing the collection capillary i.d. When holding field constant, increasing capillary i.d. will decrease resistance, increase current, and thus increase flow rate, according to Equation 10. When holding current constant, increasing capillary i.d. will decrease resistance, decrease the field in the tissue, thus decreasing the electroosmotic flow velocity, according to Equation 8. Increasing the capillary-to-tissue distance and source insertion depth increases the distance between source and collection lumen, and thus decrease flow rate. Decreasing source tip diameter decreases flow rate.

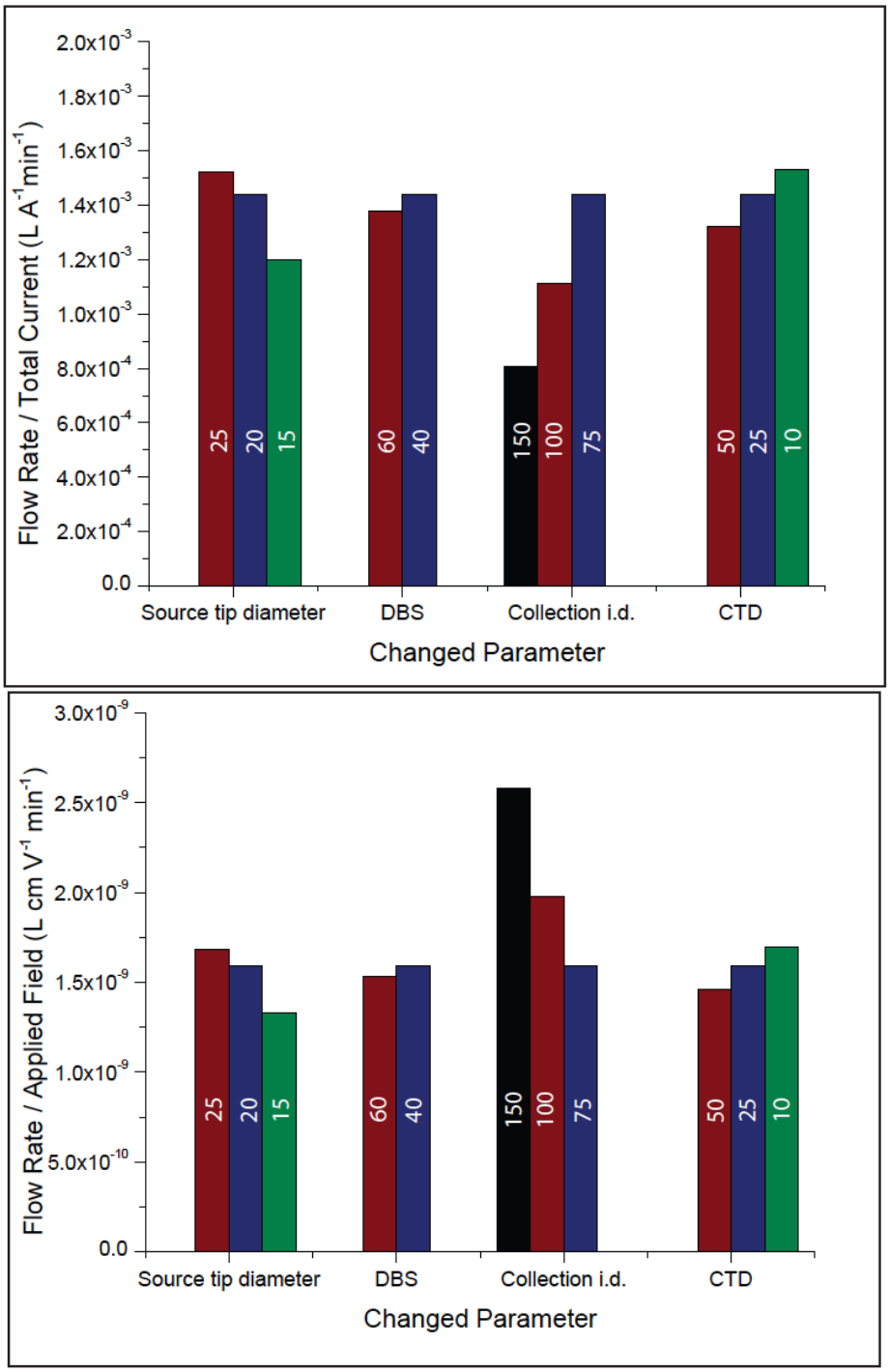

Figure 24. The effect of changing sampling geometry on electroosmotic flow rate

(TOP) Trends when holding current constant. (BOTTOM) Trends when holding applied field constant. In both, the blue bar in each case corresponds to 200 μm source i.d. with a 20 μm tip inserted 40 μm into the tissue and a 75 μm collection i.d. with a capillary-to-tissue distance of 25 μm. The blue, red, and black bars represent changing the indicated parameter to the size listed on the bar (listed in μm). Abbreviations: DBS = insertion depth, CTD = capillary-to-tissue distance.

Table 5 below compares COMSOL predictions to experimental values found in Table 4.

Applied Field (V/cm)	Flow Rate (nL/min)
3.33	6.39
5	9.60
6.66	12.8
8.33	16.0

Table 5. COMSOL-predicted electroosmotic flow rates in push-pull electroosmotic sampling

Push-pull electroosmotic sampling was simulated with a 20 μm tip inserted 40 μm into the tissue and a 100 μm collection i.d. with a capillary-to-tissue distance of 25 μm. The flow rate is calculated by integrating the flux (m^3/s) through the collection capillary lumen.

The two tables (4 and 5) are not in very close agreement with each other – Table 5 reports values three times greater than Table 4. When defining the COMSOL model, we made several assumptions, including homogeneity of the tissue, porosity and tortuosity values based on literature reported values, and a mathematical model of permeability, assuming tetrahedral and uniform cell shapes and sizes. Further development of the COMSOL model will be required to bring it closer to experimental results. This disagreement, however, doesn't preclude using the current COMSOL model as an accurate simulation of push-pull electroosmotic sampling. Because each value is off by a factor of 3, it can still be useful in predicting flow dynamics future experiments.

All-in-all, from experimentally-determined values, we that found flow rates in push-pull electroosmotic sampling are less than those routinely used in low-flow push pull perfusion[20, 21]. Furthermore, we show that all experimental flow rates are less than 10 nL/min, a threshold value determined by Kennedy, who noted that flow rates greater than 10 nL/min deplete the sampled area of analyte before it can be replenished[12].

4.3.2 Quantifying Tissue Damage

The CA1 was found to be more vulnerable to the sampling conditions in single capillary sampling than the CA3. This holds true for the push-pull model as well. Figure 25 shows the damage caused in each hippocampal region using two different collection capillary i.d.s. The CA1 is most vulnerable while the DG-IP is the least vulnerable. Figure 25 also shows that

smaller collection capillaries result in less damage, which also agrees with results found in the single capillary sampling studies. We focused primarily on the CA3, as it middles in vulnerability, for further damage studies.

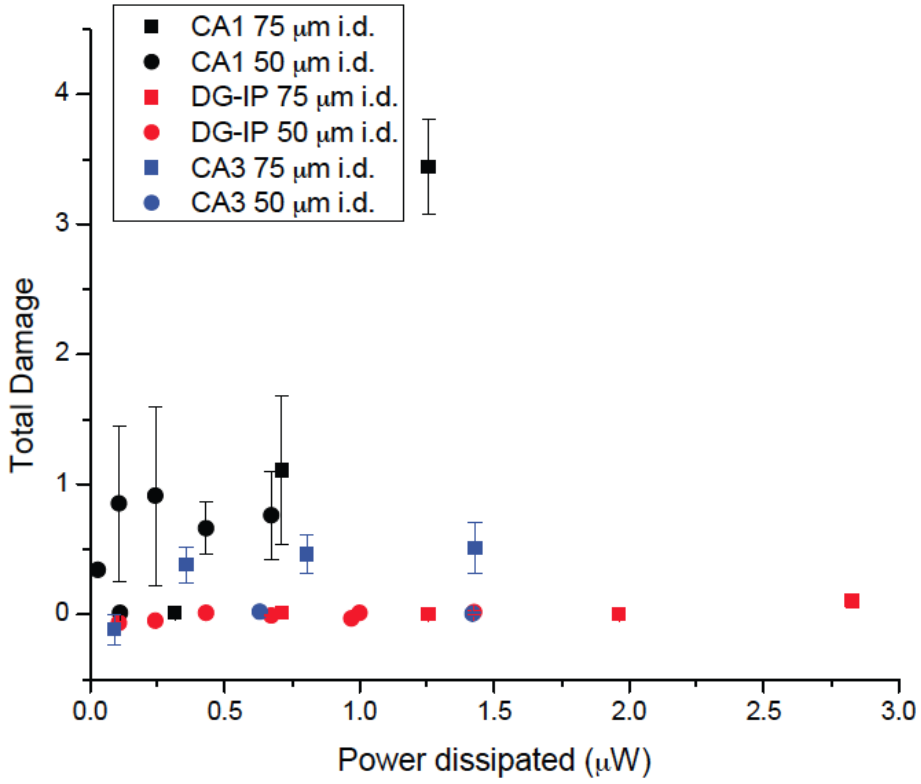

Figure 25. Tissue damage in the CA3, CA1 and DG-IP after push-pull electroosmotic sampling

In each case, the source barrel i.d. was 200 μm, the source tip was 25 μm, inserted 60 μm into the tissue. The capillary-to-tissue distance was 25 μm and the i.d. of the collection capillary was either 50 μm or 75 μm.

Similar to the single capillary sampling, we examined a wide variety of sampling geometries (capillary diameters, distance between capillaries, and capillary-tip distance) to determine a power threshold for the CA3 region. Figure 26 shows the regional damage associated in the CA3 region of the hippocampus with respect to power. The inset shows the lower power range. There was an obvious threshold in single capillary electroosmotic sampling, where damage was near zero at lower power values and increased to larger values above 20 μW. However, there is no such obvious threshold in Figure 26, but a gradual trend. Power values below 2 μW are low (below 1) and values above 3.5 μW tend to cause more damage. In the

middling power ranges, the points representing larger damage values are from larger collection capillaries.

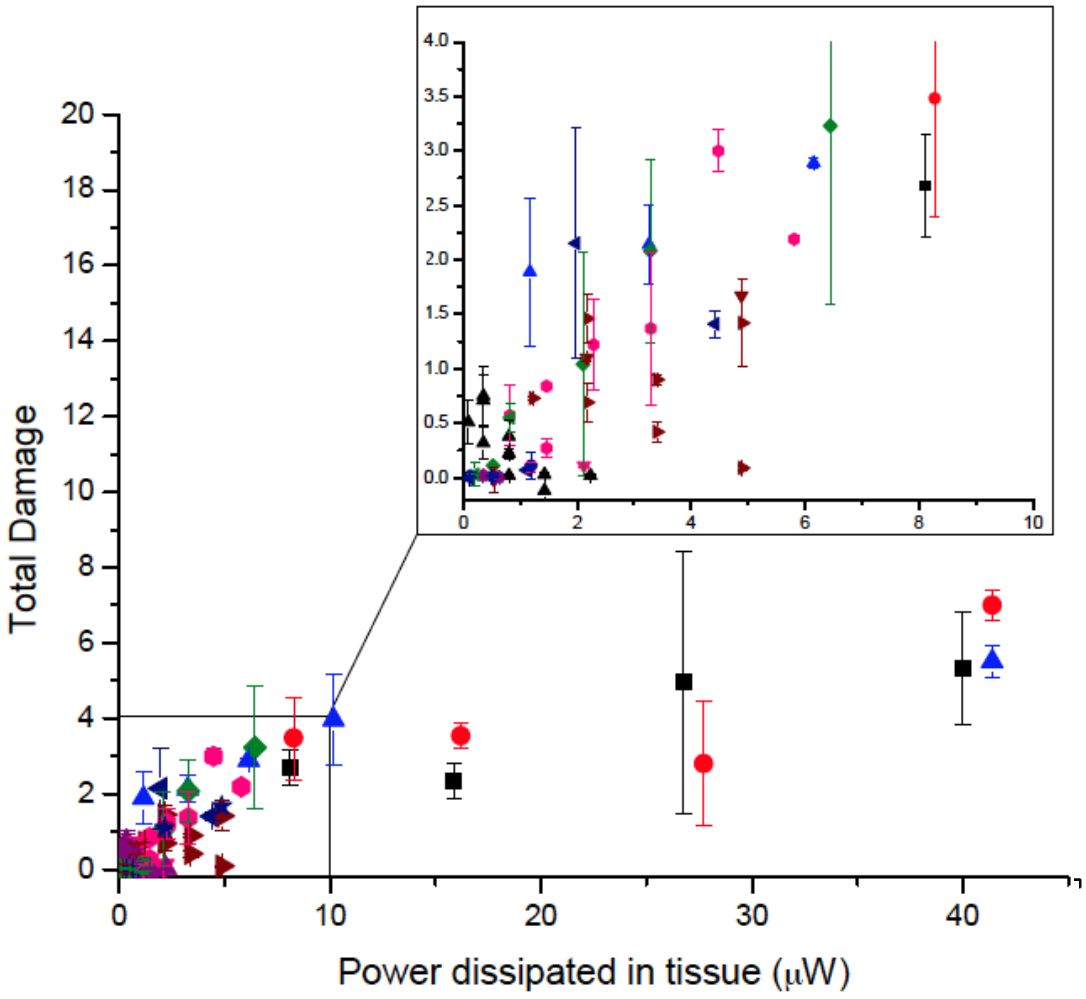

Figure 26. Damage in CA3 versus power dissipated during push-pull electroosmotic sampling

Damage in CA3 (error bars are SEM) from electroosmotic sampling of the CA3 using 13 different sampling geometries, as a function of power dissipated within the tissue. COMSOL was used to calculate dissipated power. Legend is source barrel i.d./source lumen i.d./collection capillary i.d./capillary-to-tissue distance/source insertion depth (all in μm); total n=170.

The 20 μW power threshold for single capillary sampling in the CA3 disagrees with the threshold for the push-pull arrangement (see Figure A-3 for a graph of both data sets plotted with respect to power). Power is voltage drop multiplied by current. Both models exhibit similar trends when damage is plotted against voltage drop between capillaries (not shown). However, the current within the single capillary model is 10-20 times larger than in push-pull

electroosmotic sampling, which results in the overall higher power values. This observation suggests that voltage drop rather than power may dictate damage trends. We then modeled both sets of data (single capillary and push-pull) with respect to average electric field in the tissue. Average electric field was calculated by dividing the COMSOL-calculated voltage drop within the tissue by the distance over which this drop occurred. Figure 27 shows the relationship between average electric field and damage. The single capillary data are represented as a single separate symbol (black star).

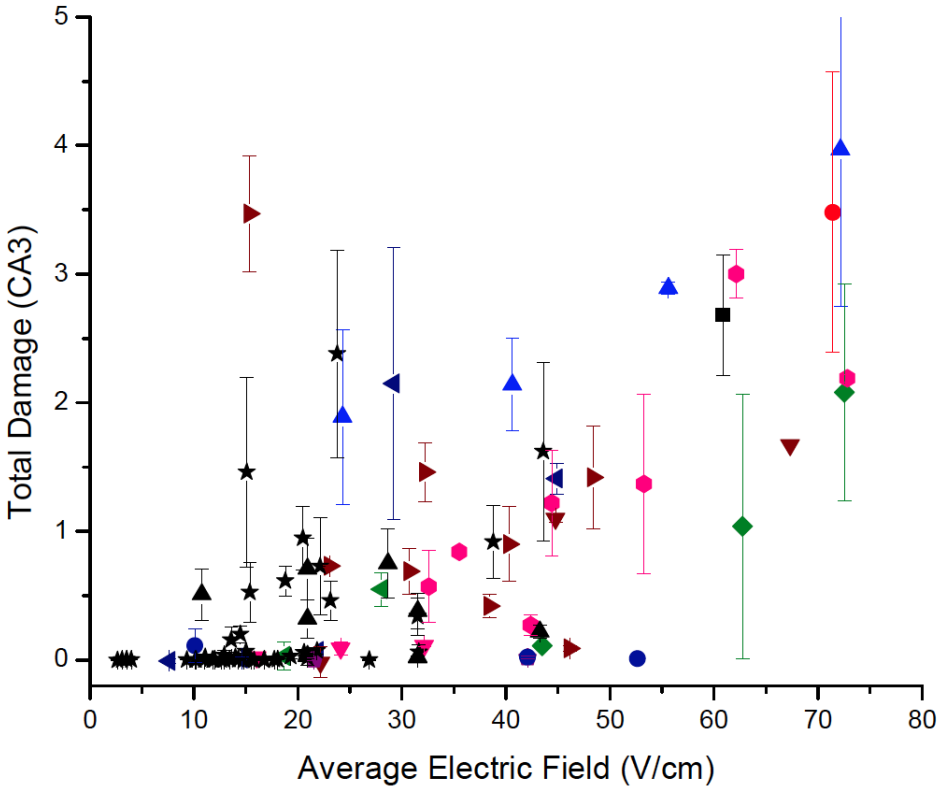

Figure 27. Total damage versus average electric field in sampled tissue

For push-pull electroosmotic sampling, this is the difference in voltage between source capillary and tissue surface under the collection capillary divided by the distance between these two points. For the single capillary arrangement, this is the difference between the surface and bottom of the tissue. Legend: same as Figure 26, black stars – single capillary sampling data.

Figure 27 gives one relationship for two different electroosmotic sampling experiments. For both sampling geometries, there is minimal damage when the voltage drop within the tissue is less than about 25 V/cm. Similar to the power trend, there is an area where damage is middling. This occurs in the area of 25-60 V/cm. It should be noted that most of these points (i.e. the blue triangle) have larger collection capillary i.d.s, which could contribute to a larger overall

area of damage. Figure 27 shows the lower field range to better visualize a damage threshold. See Figure A-4 for the same data with the full range of fields on the x-axis.

Figure 28 shows the ratio of the average electric field in the tissue (E) to the applied voltage (E_{app}) for a variety of sampling parameters to illustrate how changing the dimensions of each sampling component has an effect on the field within the tissue. These particular dimensions were chosen for sampling efficiency and tissue health. A larger source capillary will create a substantial reservoir to sample for long periods of time without having to refill the capillary. The collection capillary should be big enough to collect sample but small enough to minimize damage. Source tips should be large enough to deliver sample, but not cause physical damage when inserted into the tissue. Estimates of parameters outside this range can be calculated based on a simple resistance model with a correction for non-exact measurements of tissue dimensions. These calculations can be found in Appendix D: "A Simple Model of Resistance".

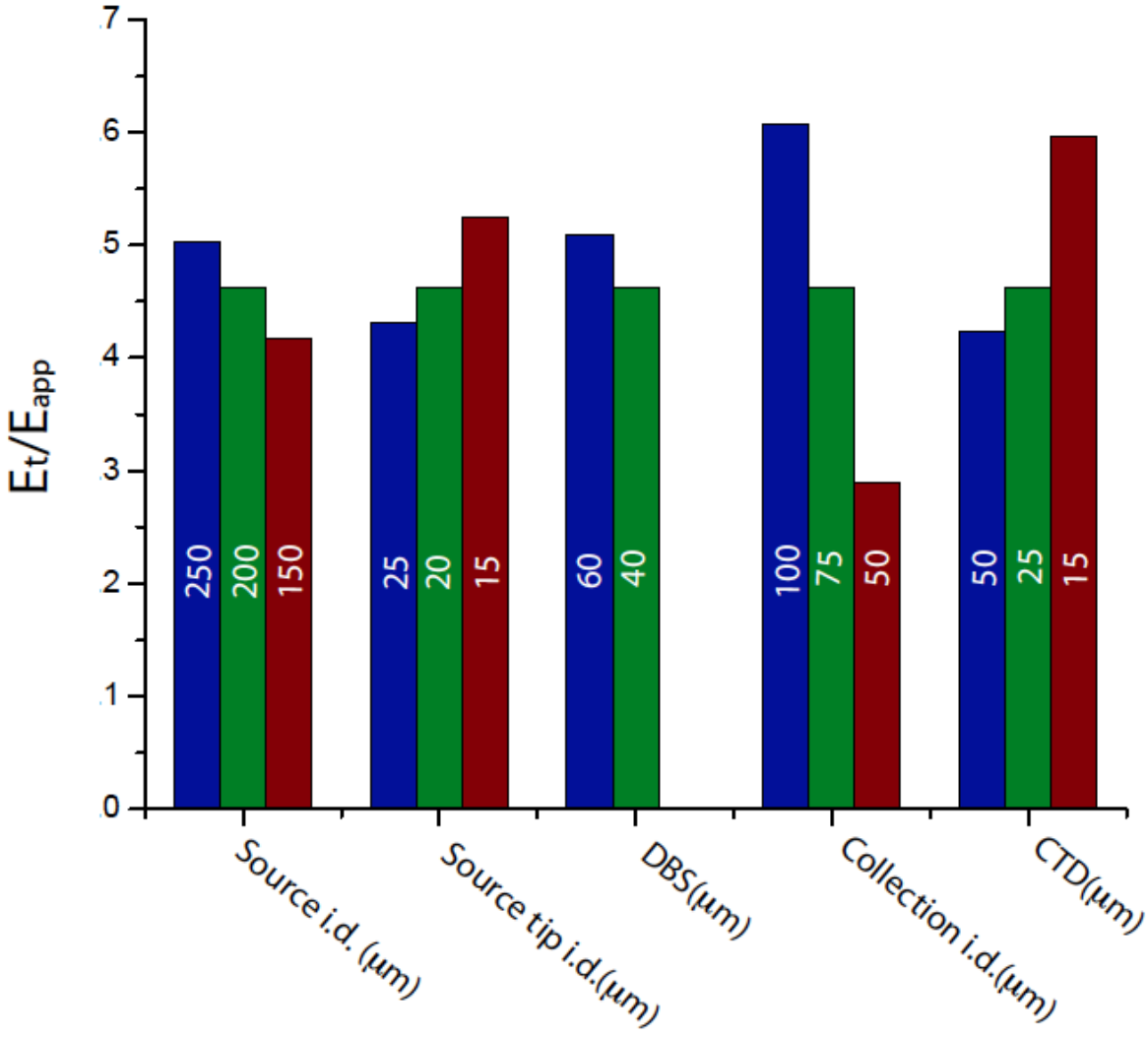

Figure 28. COMSOL-calculated effect of various sampling geometries on average electric field

The green bar in each case corresponds to 200 µm source i.d. with a 20 µm tip inserted 40 µm into the tissue and a 75 µm collection i.d. with a capillary-to-tissue distance of 25 µm. The blue and red bars represent changing the indicated parameter to the size listed on the bar (listed in µm).

In the single capillary design, we found that decreasing the collection capillary i.d. and increasing the collection capillary-to-tissue distance minimized the damage associated with sampling. These trends hold true for push-pull electroosmotic sampling as well. The tissue and capillary have mismatched zeta potentials and COMSOL models indicate a slight contribution of pressure to fluid flow between capillaries. Having some distance between the tissue surface and the collection capillary lumen might relieve some negative pressure on the tissue at this interface,

minimizing damage from physical stress. We also investigated the role of source lumen and insertion depth on damage and found neither had any significant effect on decreasing damage. Graphs illustrating this fact can be found in 'Appendix A: Additional Figures' as Figure A-5 and A-6. The source barrel size was not investigated, however, we can predict based on the trends seen for the collection capillary. Increasing the i.d. of either capillary decreases the resistance and thus decreases the contribution of the capillary to the overall resistance. When the applied voltage is constant, there will be a greater voltage drop within the tissue, and thus an overall higher average electric field. (See Appendix D: 'A Simple Model of Resistance' for basic ideas behind this conjecture).

4.3.3 Preventing Action Potential

Exposing neurons to a DC electric field makes a portion of the exposed cells' transmembrane potential less negative[70] and could depolarize neurons, triggering an action potential[71]. The effects of electroosmotic sampling on the transmembrane potential by way of calcium imaging were investigated to find conditions that did not result in a detectable influx of calcium.

The source capillary was placed. The collection capillary was moved to different places across the tissue to see if depolarization could be induced by the sampling conditions. To determine if calcium influx had occurred, regions of interest were drawn along the hippocampal formation, as shown in panel B, Figure 28. The fluorescence intensity of each region of interest was plotted against time (Figure 29, panel A). The CA1 area has the most pronounced waves, while waves of the CA3 are smaller. Images corresponding to different times are in panels B-F. Qualitatively, depolarization and calcium influx manifested in two varieties. Waves originating from the source capillary were seen immediately upon applying voltage with the collection capillary place in its initial location or not at all, regardless of where the collection capillary was moved. These waves moved along the cell body layer. In the CA1 they were one-directional moving either clockwise or counter clockwise but not both. This type of wave was never seen in any dentate gyrus region. Initiation of this event from source capillary is shown in Figure 29 B-F.

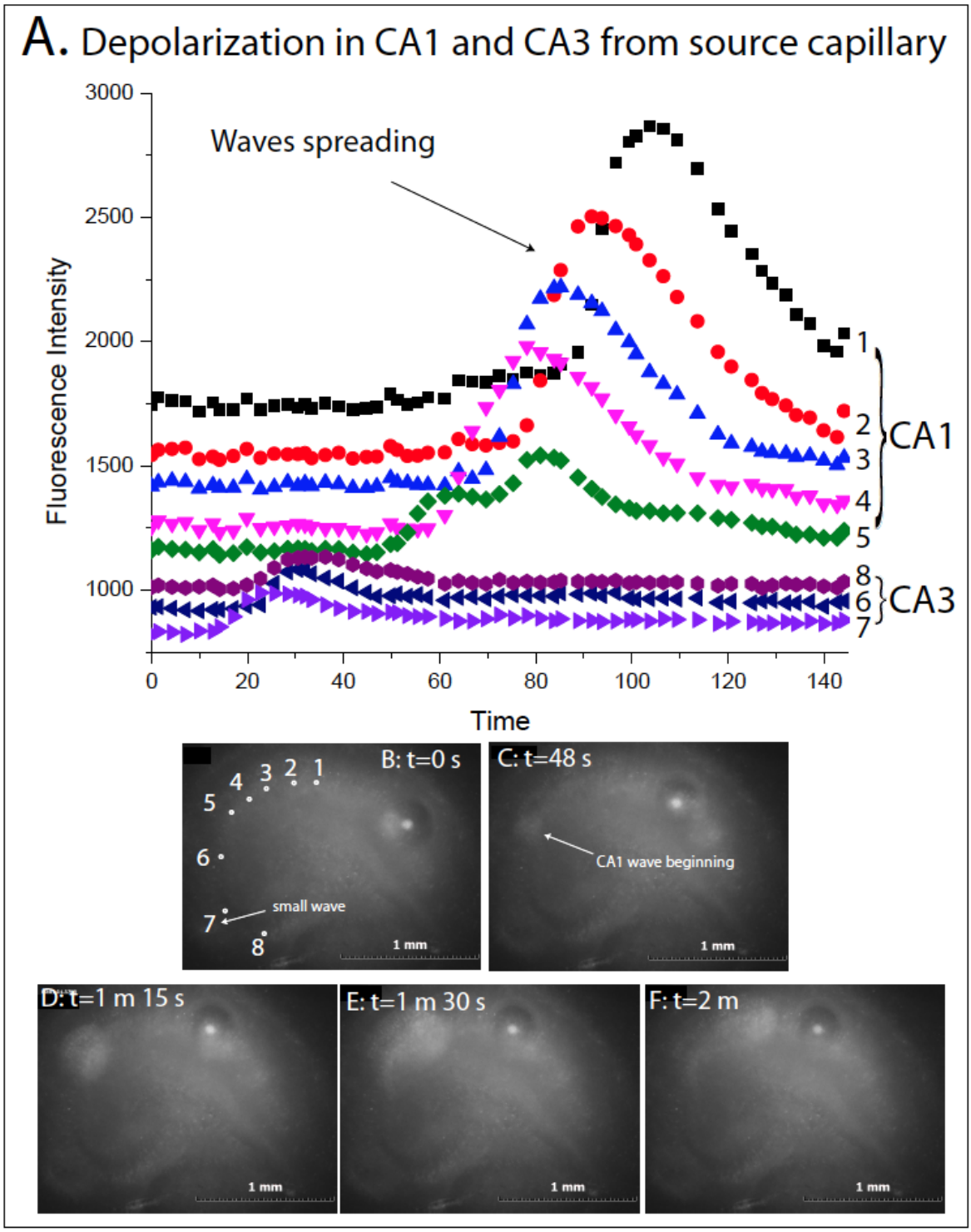

Figure 29. 'Spreading wave' depolarization of OHSC during push-pull electroosmotic sampling

(A) The fluorescence intensity various regions of interest in the CA1 and CA3 regions indicated in (B) with respect to time. Underneath, (B)-(F) show time-lapsed images of a spreading wave originating from the CA1.

In order to determine whether depolarization was also induced at the collection capillary it is necessary to apply a field and then move the capillary in order to visualize the calcium transient if it was present. Movement was necessary to see this as the capillary perturbed the image. Thus, we applied a field and periodically moved the capillary to a new position while recording continuously. The capillary was always in contact with the tissue through a thin layer of electrolyte. There was no evidence of the capillary physically touching the surface, although certainly the superficial cells in the tissue were subjected to a viscous stress. As the collection capillary was swept across the tissue in cases where the applied field was high enough, depolarization manifested itself as spreading of bursts of fluorescent intensity radiating outward from the collection capillary and trailing behind as the capillary moves. This type of depolarization becomes a truncated localized wave. These transients were more intense in CA1 than in the CA3 and DG. Figure 30 shows 6 images from depolarization created at the collection capillary. The electric field applied here was 10 V/cm.

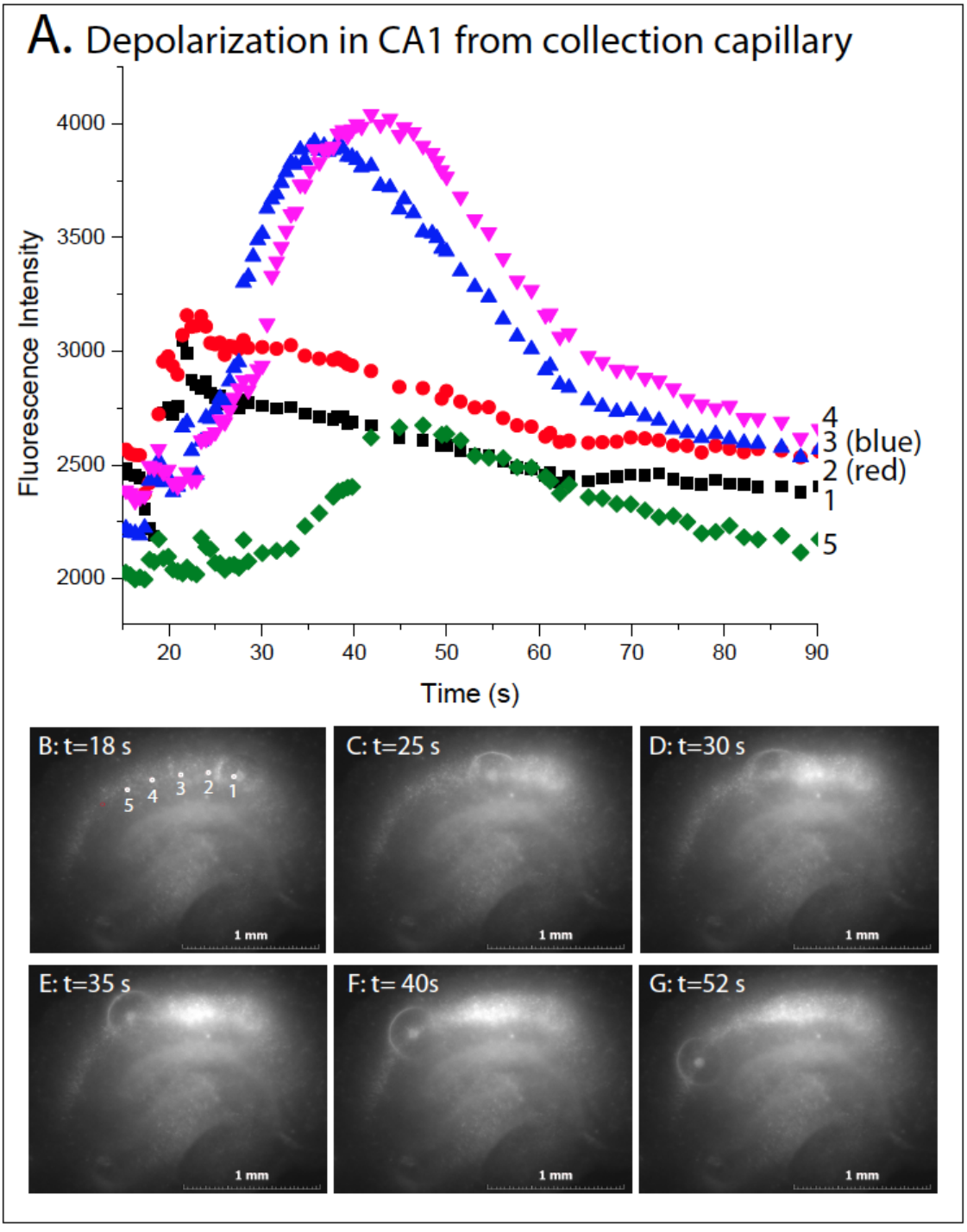

Figure 30. 'Trailing burst' depolarization of OHSC during push-pull electroosmotic sampling

(A) The fluorescence intensity various regions of interest in the CA1 indicated in (B) with respect to time. Underneath, (B)-(F) show time-lapsed images of depolarization evoked in the CA1 as the collection capillary passes by.

Figure 31 shows the percentage of attempts that invoked a calcium influx response at the collection capillary in four different regions of the tissue. The last bar in each cluster, marked with diagonal lines represents responses from the source capillary. Since the source capillary was placed just once per tissue, the reported percentage is the total number of cultures tested that resulted in a positive response from the source capillary. Overlaid on the bar graph data is a scatter plot of damage data from the CA1, CA3, and DG-IP. Table 5 tabulates the data shown in Figure 31.

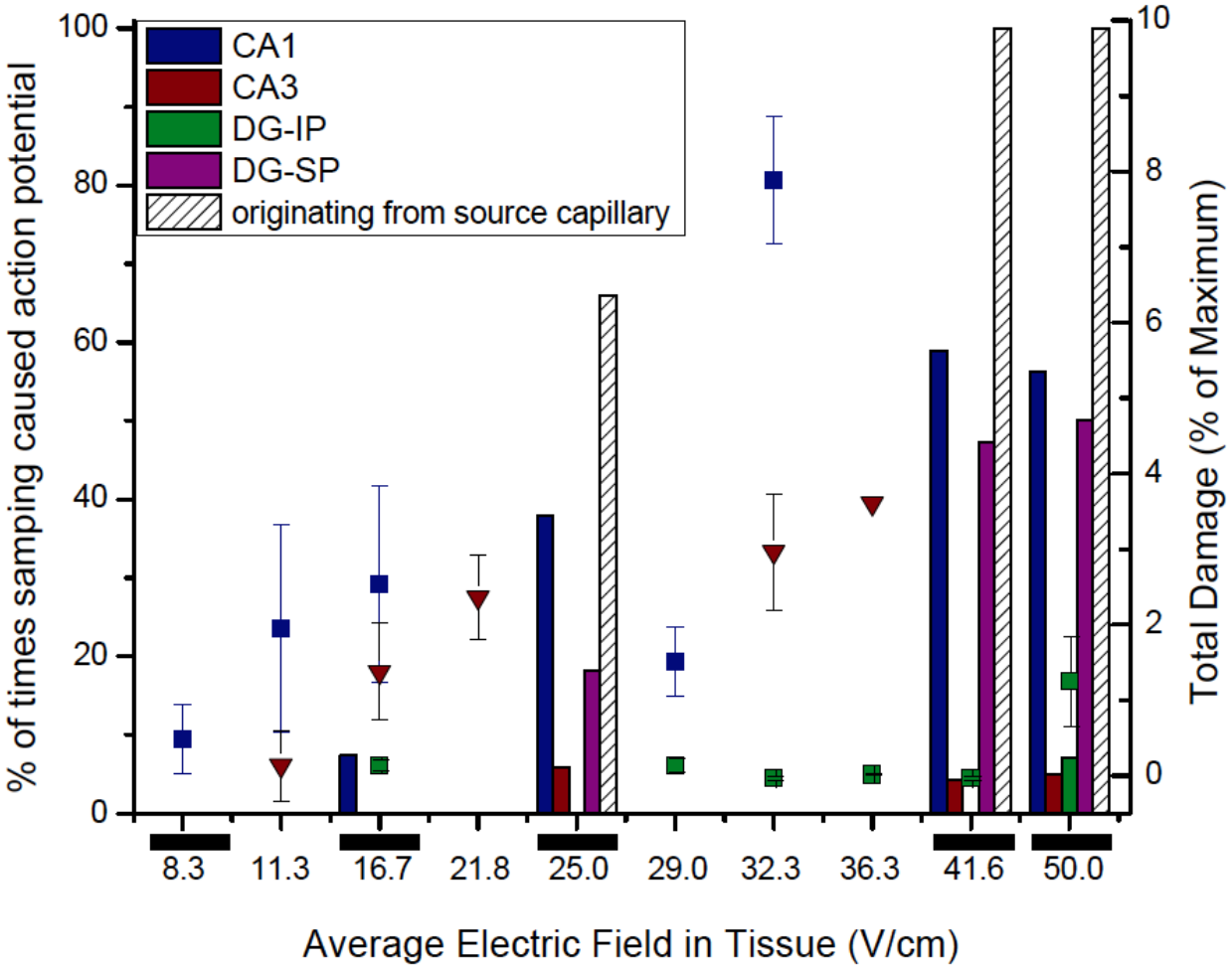

Figure 31. Action potential probability and total damage vs. average electric field

The bar graph, which denotes the percentage of cultures where calcium influx resulted from sampling conditions that create the indicated average electric field in the tissue, uses the left y-axis. Black bars under the x-axis indicate the location of each cluster of bars. Sampling at 8.3 V/cm did not invoke any calcium influx in any region of the OHSC. The scatter data shows the total damage at each average electric field, and uses the right y-axis. The colored bars represent calcium influx that originated from the collection lumen, as seen in Figure 30 in the CA1, CA3, DG-IP, and DG-SP. The bar with diagonal lines represents calcium influx that originated from the source capillary as seen in Figure 31 in the CA1. The total 'n' for the collection capillary is the number of times the capillary was paused while sweeping the tissue. The 'n' for the source capillary is the total number of cultures. The two lowest tested fields (0.09 and 0.014 V) did not evoke any calcium influx of any type in any region. Table 6 shows the numerical data represented here.

Applied Field (V/cm)	Average Field in Tissue (V/cm)	Area Tested	n (collection capillary)	Collection capillary positive responses	n (source capillary)	Source capillary positive responses
10	50	CA1	32	18	4	2
		CA3	8	0		2
		DG-SP	6	3		n/a
		DG-IP	5	0		n/a
8.33	41.67	CA1	56	33	4	2
		CA3	24	1		2
		DG-SP	17	8		n/a
		DG-IP	11	0		n/a
5	2	CA1	29	11	3	2
		CA3	17	1		n/a
		DG-SP	11	2		n/a
		DG-IP	11	0		n/a
3.33	16.7	CA1	27	2	2	0
		CA3	6	0		n/a
		DG-SP	5	0		n/a
		DG-IP	1	0		n/a
1.66	8.3	CA1	10	0	2	0
		CA3	6	0		0
		DG-SP	7	0		n/a
		DG-IP	4	0		n/a

Table 6. Action potential responses from source and collection capillary during sampling

The table above shows each applied field and each hippocampal region tested. Calcium influx manifested as waves from the source capillary or radiating bursts from the collection capillary. The 'n' for each type is listed along with the positive responses from each attempt.

The overlaid scatter data in Figure 31 shows a strong correlation between damage and the likelihood of causing action potential by sampling. The CA1, which is the most vulnerable to damage, is depolarized more often at smaller fields/voltage drops while little to no calcium influx was seen in the infrapyramidal blade at any voltage drop.

Prolonged weak DC fields have been used in a variety of applications, from modulating neuronal excitability in hippocampal slice cultures[72, 73] to treating stroke patients through transcranial direct current stimulation[74]. It is thus not surprising that the prolonged weak fields utilized in electroosmotic sampling that are minimally damaging also do not impose a

transmembrane potential higher than the action potential threshold. When the transmembrane potential rises above a certain threshold, an action potential is triggered. This typically lasts only milliseconds and the membrane returns to its resting potential quickly. When a cell is held at transmembrane potentials greater than the resting potential for longer periods of time, such as during exposure to high concentrations of potassium, these conditions can compromise the cell membrane and health of the cell[44]. Likewise, during electroosmotic sampling at higher applied fields, neurons may not be able to recover from the prolonged rise in transmembrane potential induced by the field. Less stressful conditions never invoke action potential as evidenced by the lack of calcium influx using smaller fields. The differences in vulnerability to the sampling electric field between CA3, DG, and CA1 neurons could be explained by each cell type's electrophysiological characteristics. In CA1 and CA3 neurons, the resting transmembrane potential is -67 ± 2 mV[75] for CA3 neurons 13-15 days post natal. For dentate gyrus granule neurons, the resting potential is much more hyperpolarized (-84 mV). In all three cell types, the action potential threshold is about -45 mV[55]. The larger difference between resting potential and threshold of granule cells could explain the increased resistance to damage by electroosmotic sampling of the infrapyramidal granular neurons illustrated in Figure 24.

Damage from action potential wave originating at the source and damage from the collection capillaries likely occur differently. We modeled the electric field drop outside of the source capillary using COMSOL. The electric field at the tip of the source capillary is very high but decays rapidly to 10% of the field at the tip within 20 μm. At the most, one or two 30 μm pyramidal neurons will have a portion of their cell membranes in this zone of high field, but the portion of the membrane closest to the source capillary will actually be hyperpolarized. The opposite side of the cell, a distance of 30 μm away, will be the portion that is depolarized by the source capillary. Because the field decays rapidly within 20 μm, the portion of the cell that can be depolarized experiences a much lower field. Even so, if conditions are right to depolarize the few cells near the source capillary, it could invoke action potential that moves to other cells. This is likely what we see in the wave that originates from the source capillary. However, it is only the few cells near the tip that experience the high field for an extended period of time. Distant cells that receive action potential through the wave return to normal conditions after that impulse passes. The cells can recover and likely do not suffer any damage. The effects of depolarization

at the collection capillary are different. The i.d. of the collection capillary is large and the field does not decay nearly as rapidly here. Thus many cells are exposed to the field.

A subtler source of depolarization may stem from the increased potassium ion at the source capillary. Current in the system is carried by ions; thus, there will be a higher concentration of positive ions at the source capillary and a higher concentration of negative ions at the collection capillary. These ionic imbalances are by diffusion when the source and collection capillaries are close. However, overall, this likely has a smaller effect than the depolarizing effects of the electric field.

We have investigated flow rate dynamics, and the resulting damage and perturbation of the tissue under a variety of sampling parameters. From damage studies in push-pull electroosmotic sampling, we found that damage increases with power dissipated in the tissue and with the average electric field in the tissue. Experimentally, decreasing the inner diameter of the collection capillary can minimize damage. Decreasing source capillary i.d. likely will have the same results. While the COMSOL model shows that the size of the source tip creates a larger voltage drop between capillaries, this does not influence the overall damage seen experimentally. The insertion depth of the source capillary also had no noticeable effect in both damage nor in voltage drop and likely plays only a small role in that it dictates how much of the tissue is between the two capillaries. To link damage and flow rate studies, we used conditions minimized total damage below 1 to sample $^{D}Y^{D}AG^{D}F^{D}L$. Applied fields of 6.66 V/cm in 100 μm i.d. or smaller collection capillaries have little damage, create flow rates that are below the 10 nL/min threshold, but are fast enough to collect a detectable quantity of source analyte, even when diluting nearly 5-fold during sample preparation. The flow rate and damage trends outlined in these studies serve to guide experiment. One must balance detection limits and desired flow rates with the necessity to minimize damage. This will change with individual application and experiment.

5.0 GALANIN HYDROLYSIS IN THE EXTRACELLULAR SPACE

5.1 INTRODUCTION

The efficacy of a neurotransmitter ultimately relies on its arrival at and binding to a target receptor. In wired transmission, the molecule will easily arrive at its target on the other side of the 25 nm synaptic cleft. However, the majority of transmitters must enter the extracellular space, where the path from release to receptor is perilous. A variety of events can interfere with the journey, including reuptake by the release cell or other cells, crossover into the blood system, diffusion away from the target cell, or hydrolysis by ectopeptidase, if the molecule is a peptide or a protein.

Ectopeptidases, membrane-bound outward facing enzymes, typically inactivate endogenous peptides in the extracellular space to control their efficacy[76]. This has been illustrated by decreased peptide effects when ectopeptidase activity is pharmaceutical inhibited or genetically knocked down[4]. Changes in peptidase activity occur following various types of stress and injury. Heat stress alters substance P endopeptidase activity[32] and immobilization stress changes enkephalinase and oxytocinase activities in several brain regions[29]. Water maze training changes regulation of a stress hormone (TRH) and degrading enzymes[32]. After ischemia/reperfusion, the activity of enzymes that degrade β-amyloid peptide decreased as well[35]. The notion peptide activity can be indirectly controlled by modulating peptidase activity has even aided development of analgesic treatment[7].

Cerebral ischemia is the reduction or blockage of blood flow to the brain, which often results in neuronal damage. This damage is caused by the lack of oxygen and glucose (oxygen glucose deprivation, OGD), normally supplied by the blood and essential for energy production (ATP) in a cell. Typically, the hippocampus is most severely affected by ischemic insult[77] and the damage caused in this area results in loss of memory, language skills and motor function. The series of events that results in damage is quite complex, but essentially results in the failure of

transmembrane ion and voltage pumps requiring ATP, followed by the free transfer of ions across the membrane and subsequent depolarization of the cell membrane. Ion imbalances spur an excitotoxic release of glutamate resulting in osmotic lysis (necrotic cell death) or mitochondrial dysfunction and induction of apoptosis. An oxygen-free cellular environment also damages DNA, signaling the mitochondria to initiate apoptosis. The signaling involved in the ischemic cascade and subsequent cell death is a complex web of neurotransmitters, transcription factors, receptor binding/activation and a host of enzymes, which is well understood. Less understood, however, are ways to prevent and/or mitigate and repair damage that occurs during ischemia. Researchers strive to understand these endogenous neuroprotective mechanisms and use them to develop therapies to alleviate ischemic damage.

Ischemic preconditioning creates resistance of neurons to cell death arising from ischemic injury[78] and was first discovered to be a viable method in the heart in 1986[79]. It is achieved by depriving tissue of oxygen/glucose for a short period of time before a second deprivation with a longer duration. After the second episode, ischemic preconditioned tissues do not suffer as much damage as those that were not conditioned. Neuroprotection has two windows of efficacy: 4-6 hours post ischemic preconditioning and 24-72 hours post ischemic preconditioning. The latter phase typically involves de novo protein synthesis to mediate the protective effects of ischemic preconditioning[78]. Similar to previously discussed models of injury, ischemic preconditioning increases expression of several enzymes including heat shock proteins and nitric oxide synthase[80] and also activate nuclear transcription factor-*k*B[81], which is required for DNA synthesis. However ischemia and ischemic preconditioning are complex and it is likely that there are additional enzyme systems altered in ischemic preconditioning. We investigate one such system here.

Galanin is a C-terminus amidated 29 amino acid peptide in rat (human is 30 amino acids, not amidated) involved in a large variety of neuronal signaling pathways[82-88], including neuroprotection. Galanin has pro-survival actigity in Alzhiemer's disease[14] and in excitotoxic injury, a primary component of ischemic injury[89, 90]. There are only two reports on the half-life (degradation rate by peptidases) of galanin, which have been studied only in hypothalamus and spinal cord preparations[91, 92]. This same study identified specific galanin-degrading peptidases in these two areas using inhibitors, showing that zinc chelators such as *o*-phenanthroline, EGTA, and EDTA decreased hydrolysis of galanin by metalloproteases[93]. In hypothalamus preparations,

bacitracin inhibited the degradation of galanin to a greater extent than metalloprotease inhibitors, which indicates greater activity of non-metalloenzymes. Another study a few years later confirmed inhibition of galanin-degrading peptidases by metal chelators and calculated K_m and V_{max} values for a galanin-degrading 70 kDa enzyme in bovine spinal cord preparations[94]. However, these studies homogenized the samples, destroying any spatial information. Furthermore, galanin hydrolysis following stress or injury has not been studied nor has it been investigated in the hippocampus.

Ectopeptidase activity is typically considered inactivating, however, this is not always the case. Peptides may also be converted into fragments that retain or may even have completely different biological actions than the parent peptide[76]. Studies in the late 1990s investigated the binding of galanin fragments to receptors *in vitro* to identify what fragments retain residues required for binding to galanin receptors. The deletion of the gly^1 residue decreased binding of Gal 2-29 for the GalR1 receptor; however, the GalR2 retains binding activity with this modification[95, 96]. Peptides with the gly^1 intact (galanin (rat) 1-29, and fragments 1-12, 1-15, 1-16, 1-20) have K_i values (for rat or human GalR2) ranging from 0.6 nM to 13 nM, depending on the cell line studied. Residues retaining the second amino acid, but not the first, such as 2-29 and 2-11, have K_i values ranging from 1.9 nM to 88 nM. Loss of the first two residues, resulting in Gal 3-29, inhibits displacement of isotopically-labeled galanin 1-29 in a variety of cell lines studied[88]. However, residues in the C-terminus may still contribute some binding activity. Smaller C-terminal fragments, such as synthetically prepared Gal 12-29, 18-29, and both synthetic and tryptic Gal 21-29 partially displace isotopically-labeled galanin bound to the galanin receptor[97].

Galanin exerts neuroprotection through binding to the GalR2 receptor[89]. As galanin is an inhibitory (rather than excitatory) molecule, protective effects are thought to be mediated through attenuating glutamate toxicity[90, 98]. PKC and MAPK pathways are also initiated upon GalR2 activation and contribute to subsequent tropic activity[89, 99, 100]. The hippocampal formation has a high density of galanin, GalR2 receptor, and receptor mRNA[64, 101, 102]. Extracellular galanin increases in the CA1, CA3 and dentate gyrus hilar regions in the hippocampus following ischemia. Galanin immunoreactivity in the CA1/CA3 peaks at 12 hours after ischemia and lasts for 2 days[103, 104]. The duration of increased expression coincides with initiation of de novo protein synthesis after ischemic preconditioning. Increased galanin

synthesis, increased synaptic release, or increased lifetime in the extracellular space could all cause increased extracellular galanin. We focus on the third possibility, hypothesizing that peptidase activity is altered in the hippocampus following ischemic preconditioning to promote increased extracellular galanin concentrations. To our knowledge, there have been no studies conducted on galanin degrading peptidase activity in the hippocampus.

5.2 EXPERIMENTAL

We used push-pull electroosmotic sampling to introduce exogenous galanin into OHSCs that were ischemically preconditioned and those that were not. In each case, galanin was transported through the extracellular space, exposed to and degraded in part by endogenous ectopeptidases. Fragments and intact peptide were collected and analyzed offline via HPLC to quantify extent of hydrolysis, which is indicative of ectopeptidase activity. We also attempted to identify galanin-degrading peptidases by using MALDI-MS to elucidate patterns of galanin fragmentation. We also used various peptidases inhibitors to detect any changes in galanin-degradation following inhibitor treatment.

5.2.1 Solutions and Reagents

HBSS solutions, TR3 solutions, diluent, HPLC mobile phases, and the $^{D}Y^{D}AG^{D}F^{D}L$ internal standard were prepared identical as described in 'Solutions and Reagents', Chapter 4. Galanin (rat) 1-29 (Abbiotec, San Diego, CA, USA) solutions were prepared by dissolving 1 mg of the galanin solid in 1 mL HBSS (Life Technologies). Solutions were frozen until use. The MALDI matrix, α-Cyano-4-hydroxycinnamic acid (CHCA) was prepared by dissolving 10 mg CHCA (Sigma) in 2 mL 50:50 H_20/ACN + 0.1% triflouroacetic acid (Sigma), filtered after preparation through a 0.45 μm syringe filter (final concentration 5 mg/mL. To equilibrate zip-tips, water supplemented with 0.1% TFA and acetonitrile supplemented with 0.1% TFA were prepared and passed through 0.45 μm syringe filters. Glucose-free HBSS was prepared for ischemic pre-conditioning experiments by dissolving NaCl (134 mM), KCl (5.40 mM), $MgSO_4$ (1.20 mM), NaH_2PO_4 (1.38 mM), $CaCl_2$ (2.65 mM), HEPES (5.00 mM, all from Sigma) in purified Millipore

water (Synthesis A10). The pH of the buffer solution was adjusted to 7.40 with NaOH solution then vacuum filtered through a 0.45 μm PTFE membrane. Inhibitors were prepared in stock solutions of either DMSO or HBSS according to their solubility. Final treatment solutions were diluted at least 1000 fold to the following concentrations: *o*-phenanthroline: 0.2 mM; puromycin: 20 μM; bestatin: 145 μM; amastatin: 10 μM; phosphoramidon: 920 μM; pepstatin A: 22 μM; E-64: 56 μM; and thiorphan: 5 μM. All inhibitors were obtained from Sigma. EDTA (Sigma) was dissolved directly in medium solution by constantly stirring while raising the pH to 9.0 with NaOH. After the EDTA dissolved, the final pH was 7.4 and the concentration of EDTA was 10 mM. This was then diluted with fresh medium for a final EDTA concentration of 0.5 mM.

5.2.2 Qualitative Studies – Identification of Galanin Fragments

The source capillary fill solution consisted of 50% stock galanin solution (0.31 mM) and 50% TR3 solution to aid in the verification that electroosmotic flow was occurring. After voltage was applied for 5 minutes, the collection capillary contents were pushed into a polypropylene vials containing 10 μL of a 0.1% TFA aqueous solution with air. Each sample was de-salted and concentrated using ZipTips (μ-C18, Millipore). The ZipTips were equilibrated with 2 10 μL aliquots of acetonitrile (ACN) + 0.1% TFA and water + 0.1% TFA solutions prior to sample capture. De-salting occurred by washing the captured sample with 10 μL water + 0.1% TFA solution prior to elution onto the MALDI plate with 0.8 μL 50:50 H_20:ACN + 0.1% TFA. CHCA matrix (5 mg/mL, 0.6 μ□)was immediately spotted on the dried sample spot.

Mass spectral analysis was performed on a 4800 MALDI-TOF/TOF with from Applied Biosystems (subsidiary of Life Technologies). Calibration spots consisted of the mass standard kit for calibration of ABSciex TOF/TOF (ABSciex), mixed with CHCA (10 mg/mL).

Spectra were viewed using the Data Explorer program (Applied Biosystems). Peak lists for each sample were compiled using a S/N threshold of 20. The list was input into the 'findpept' program (http://web.expasy.org/findpept/), using galanin, GWTLNSAYLLGPHAIHNRSFSDK-HGLT-NH_2, as the parent peptide. The resultant matches to possible galanin fragments were confirmed through MS-MS analysis and de novo sequencing. Since biological samples are complex, outright de novo sequencing was difficult. I then used the fragment ion calculator (http://db.systemsbiology.net:8080/proteomicsToolkit/index.html) from the Institute for Systems

Biology. The suspected sequence of the galanin fragment (including the amidation of the c-terminus if the c-terminus was part of the fragment) was the program input. The output was a list of b and y ions, which was compared to the spectrum of the suspect fragment. Typically, it was very clear if the spectrum matched the list or not. The b ion peak corresponding to the break between D^{17} and K^{18}, if these residues were present in the galanin metabolite, was the strongest peak. As the first and last few fragment ions, of both b and y type are sometimes missing, spectra that matched 70% of the listed peaks were considered a positive match. Those that matched less were considered a negative match or inconclusive. Periodically, MS/MS spectra were obtained to verify that a particular m/z was still the galanin fragment to which it was assigned identity.

5.2.3 Oxygen Glucose Deprivation – Ischemic Preconditioning

All cultures were treated with PI and screed prior use to ensure viability, identically to procedures outlined in 'Assessment of Viability', Chapter 3. Ischemia typically refers to the blockages of blood, which then reduces oxygen and glucose supply to neurons. Since OHSC do not have a blood supply, we induce oxygen glucose deprivation (OGD) by submersion in an oxygen and glucose free buffer solution. A timeline of experiments is shown in Figure 32.

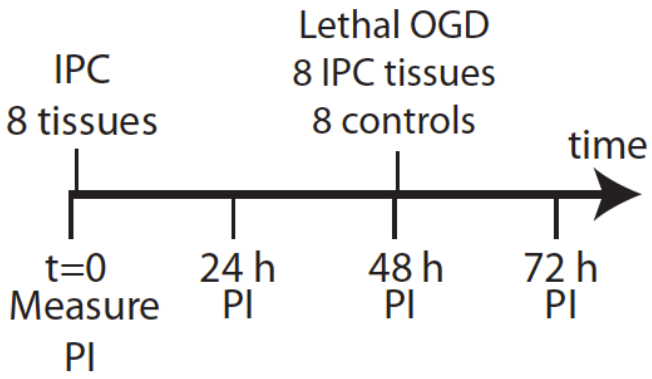

Figure 32. Experimental timeline for inducing and verifying ischemic preconditioning

Cultures are first checked for viability then immediately exposed to 30 minutes of ischemic preconditioning. PI fluorescence is measured 24 and 48 hours later. If cultures were still viable after ischemic preconditioning, Ischemically preconditioned cultures and a set of control, non-ischemically preconditioned cultures were subjected to 45 minutes of lethal OGD. PI of both sets and a third set that had remained in culture the whole time was measured at 72 hours, 24 hours after lethal OGD.

A submersion box chamber was fabricated in-house which allowed for perfusion of solution and a closed environment to prevent re-oxygenation of solution. Glucose-free HBSS was warmed to 36 °C before use and bubbled with N_2. Solution was circulated in the submersion chamber using a variable-flow peristaltic pump (Fisher Scientific) and dissolved O_2 levels were monitored using a DO 110 portable dissolved O_2 meter (Oakton Instruments, Vernon Hills, IL). All components were contained within a humidified CO_2 incubator, to keep solution temperature constant. Once O_2 levels dropped below 5%, OHSCs were securely submerged in the glucose-free HBSS for 30 minutes. Four insert membranes, or 8 cultures were submerged at a time. Nitrogen was bubbled throughout tissue submersion and oxygen levels were monitored. After 30 minutes, the cultures were immediately returned to a 5% CO_2, 95% air environment, and placed back in their original 6-well plate containing warmed medium solution. Within 3 hours, PI was added to the medium of cultures that had undergone OGD, two sets of 8 cultures that had remained in culture (negative controls), as well as two cultures that were treated with MeOH to serve as a positive control.

PI fluorescence was imaged identically as in 'Assessment of Viability', Chapter 3. If no damage was found at 48 hours, the pre-conditioned set and one set of negative controls were subjected to 45 minutes of submersion OGD. The second negative control set remained in normoxic conditions. Cultures were returned to normal culturing conditions immediately following OGD. PI was added to all tissues, including the remaining negative control group. PI fluorescence was imaged 24 hours later (at 72 hours, according to Figure 32) in all cultures. Tissue damage was quantified as outlined previously in 'Quantifying Tissue Damage', Chapter 3.

5.2.4 Sampling from Ischemically Preconditioned Cultures

In parallel sampling experiments, cultures were pre-conditioned according to the above-described protocol. Twenty-four hours later, PI was imaged to verify mild OGD did not cause damage. If cultures were still viable, exogenous galanin was passed through the extracellular space of ischemically preconditioned cultures and non-ischemically preconditioned cultures using push-pull electroosmotic sampling. Two to three insert membranes (4-6 tissues) were removed at a time for sampling. Tissues remained outside of the incubator for no longer than forty minutes before sampling. The source capillary was filled with 2.73 mM internal standard,

0.155 mM galanin, and 2-10 mM TR3 to visualize fluid movement. Sampling was performed identically as outlined in 'General Sampling Procedures', Chapter 4, using a 100 μm i.d. collection capillary, a 200 μm i.d. source capillary, a capillary-to-tissue distance of 25 μm, and a DBS of 60 μm. The lumen of the source capillary ranged from 15-22 μm. The applied electric field was 6.66 V/cm and was applied for 10 minutes. The CA1, CA3, and DG (either blade) were targeted sampling areas. All samples were collected (pushed out of the collection capillary by air) in 10 mL diluent (9.5 μM GGFL + 0.1% TFA) and immediately injected onto an analytical column for separation. Internal standard and galanin standard solutions were prepared identically as 'Solutions and Reagents', Chapter 4 by diluting the fill solution, which contained 27.25 mM internal standard, 0.155 mM Galanin (and TR3) in to 1 mL with 0.1% TFA. This solution was further diluted down in acid to make several standards, each with GGFL concentration of 6.65 μM (to act as HPLC injection standard). All standards and samples that contained galanin required immediate injection, as we found that the concentration of galanin in a sample decreased over time when in the HPLC vial, indicating either degradation or adsorption to the vial. For this reason, all standards included in any calibration regression were also injected immediately after preparation, before sampling commenced.

5.2.5 Quantifying Relative Rates of Galanin Hydrolysis

Calibration curves were constructed for galanin and the $^{D}Y^{D}AG^{D}F^{D}L$ internal standard. The concentration of internal standard in the sample was calculated identically as outlined in 'Quantifying Electroosmotic Flow', Chapter 4. Calculating the concentration of galanin was also carried out in identical fashion, using the equation for the linear regression line when plotting GGFL-corrected galanin peak area against galanin concentration. Galanin regression lines were forced to go through the origin. Figure 33 shows calibration curves for the internal standard and galanin. All calibration points and sample peak areas were corrected for injection volume with the peak area of GGFL, according to Equation 4, as shown previously.

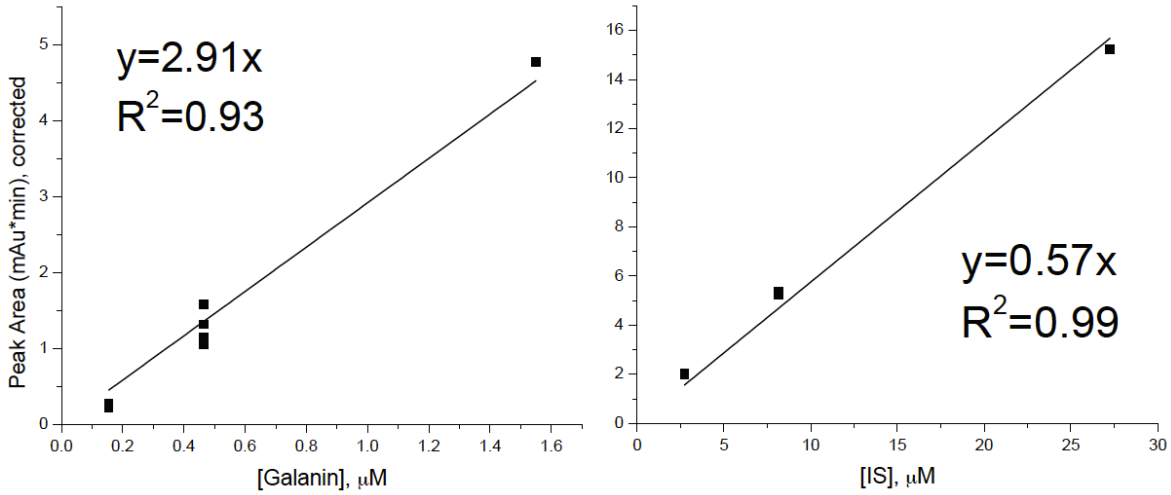

Figure 33. Galanin and internal standard calibration curves for HPLC analysis

Each point was corrected according to Equation 4 for variability in injection volume by the HPLC auto sampler. This calibration curve was used to quantify the concentration of galanin and internal standard (IS = ^{D}Y^{D}AG^{D}F^{D}L) in each sample collected to calculate the relative rate of galanin hydrolysis in an OHSC after various treatments.

The relative rate of galanin hydrolysis can be calculated by assuming a first order enzyme rates according to Equation 14.

$$moles_{Gal,collected} = U_{gal} t_s [Gal]_{source} - U_{IS} t_s [Gal]_{source} e^{-kt_{exposure}} \quad (14)$$

U_{gal} is the flow rate of galanin, t_s is sampling time, $[Gal]_{source}$ is the concentration of galanin in the source capillary, k is the enzyme rate, and $t_{exposure}$ is the exposure time of the galanin to the tissue. We cannot directly measure the flow rate of galanin, so we use the flow rate of the internal standard, U_{IS} instead. By using the internal standard as a measure of flow rate, we are assuming that ^{D}Y^{D}AG^{D}F^{D}L and galanin have the same flow rate during sampling. This is actually not true. Galanin has a +1 charge at pH 7.4 and the internal standard is neutral. Thus, galanin will move faster toward the anode. Furthermore, the internal standard is smaller than galanin, and will diffuse away from the sampling site faster. However, the flow rate of galanin is proportional to that of the internal standard regardless of flow rate. U_{gal} is simply U_{IS} times a constant (α). We can define the flow rate mathematically by Equation 15.

$$U_{gal} = \alpha U_{IS} = \alpha \frac{moles_{IS,collected}}{[IS]_{source} t_s} \quad (15)$$

Substituting the flow rate into Equation 14, we get Equation 16 rearranged into Equation 17.

$$moles_{Gal,collected} = \alpha \frac{[Gal]_{source}}{[IS]_{source}} moles_{IS,collected} - \alpha \frac{[Gal]_{source}}{[IS]_{source}} moles_{IS,collected} e^{-kt_{exposure}} \quad (16)$$

$$\frac{moles_{Gal,collected}}{moles_{IS,collected}} = \alpha \frac{[Gal]_{source}}{[IS]_{source}} \left(1 - e^{-kt_{exposure}}\right) \quad (17)$$

By experimental design, the ratio of galanin to internal standard in the source is constant, and α is a constant. We can then say that the moles or concentration (since both are collected in the same capillary volume and diluted equally) of galanin to internal standard in the collection capillary are proportional to the enzyme rate. We used this ratio to compare enzyme rates in cultures with different treatments to decide if the rate of galanin hydrolysis changes following ischemic pre-conditioning.

5.2.6 Inhibitor Treatment

All inhibitors were added to the culture medium 16-24 hours prior to sampling. Sampling, sample collection, and analysis occurred identically to procedures outlined in 'Experimental', Chapter 4, except that cultures remained over inhibitor-containing medium instead of HBSS to prevent washing away of inhibitor.

5.3 RESULTS & CONCLUSIONS

5.3.1 Galanin Fragment Identification

Table 7 shows a list of positive matches and the calculated molecular weight (C^{12}).

Confirmed Fragments	Molecular weight (g/mol), monoisotopic	Confirmed Fragments	Molecular weight (g/mol), monoisotopic
Gal 21-29	990.48	Gal 11-29	2102.03
Gal 20-29	1147.56	Gal 1-20	2191.09
Gal 19-29	1283.64	Gal 10-29	2215.11
Gal 18-29	1398.66	Gal 1-21	2278.12
Gal 17-29	1513.69	Gal 1-22	2425.19
Gal 16-29	1626.78	Gal 8-29	2435.20
Gal 15-29	1697.81	Gal 7-29	2506.24
Gal 14-29	1833.88	Gal 5-29	2606.32
Gal 13-29	1931.92	Gal 3-29	2920.46
Gal 12-29	1988.95	Gal 1-27	2949.43
Gal 1-19	2034.99		

Table 7. Galanin fragments found after push-pull electroosmotic sampling with galanin peptide

All fragments were confirmed with MS/MS analysis and comparing expected b and y ions of the particular fragment to the experimental spectrum.

5.3.2 Patterns of Hydrolysis

Even though many peptidases are non-specific and will degrade a wide variety of peptides, many exhibit specific patterns of cleavage which may be helpful in identifying the activity of some peptidases[76]. We compiled a list of fragments found in each hippocampal area sampled in Table 8. The largest peak in all sample spectra was that of intact galanin. Other fragments varied in intensity with respect to one another. The fragment 1-19 was the most frequently found among all samples. In experiments where the source capillary contained no galanin, the spectra were blank, indicating that we are not detecting endogenous galanin, but only galanin and fragments formed by the galanin introduced by the source capillary. According to Table 8, under similar sampling conditions, a fewer number of fragments are found in CA1 samples when compared to those collected from DG or CA3. The pattern of hydrolysis shows sequential cleavage from the c-terminus, suggesting aminopeptidase activity[12]. There are several also have shown binding affinity to the galanin receptor: those that retain the n-terminus and several that retain the c-terminus (3-29, 12-29, and 18-29)[97]

	Area & time sampled (min)	DG 5	DG 5	DG 5	CA3 5	CA3 5	CA3 5	CA3 10	CA3 5	CA1 5	CA1 5	CA1 5	CA1 10	CA1 10
	Relative residence time*	1	1.4	2	1	1.4	2	2.5	3.33	1	1.4	2	3.33	5
Galanin Fragment	1-29	x	x	x	x	x	x	x	x	x	x	x	x	x
	1-19	x	x	x	x	x	x	x	x	x	x	x	x	x
	1-27	x	x	x		x		x		x			x	x
	3-29		x		x	x								x
	5-29	x	x		x	x								
	7-29	x	x	x	x	x	x	x			x		x	x
	8-29		x		x	x	x	x		x	x			
	10-29	x	x	x	x	x	x	x					x	x
	11-29	x	x	x	x	x	x	x	x		x	x	x	x
	12-29	x	x	x	x	x	x	x	x		x	x	x	x
	15-29	x	x	x	x	x	x	x	x				x	x
	16-29	x	x	x	x	x	x	x	x		x	x	x	
	18-29	x	x	x	x	x	x	x	x	x	x			
	19-29	x	x	x	x	x	x							
	20-29	x	x	x	x	x	x	x	x		x	x		

Table 8. Galanin fragments created in CA1, CA3, and DG regions of the OHSC

Relative residence time correlates to the applied voltage and current. For example, a value of 1 is the highest current and fastest flow, and corresponds to an applied field of 16.6 V/cm and 56 μA. A value of 5 corresponds to a field of 5 V/cm and 12 μA. Bold lines separate different hippocampal regions.

Figure 34 below summarizes Table 8 and indicates those fragments found in CA1 versus those found in the CA3 and DG areas. There is a smaller variety of fragments found in the CA1, when compared to the other two areas.

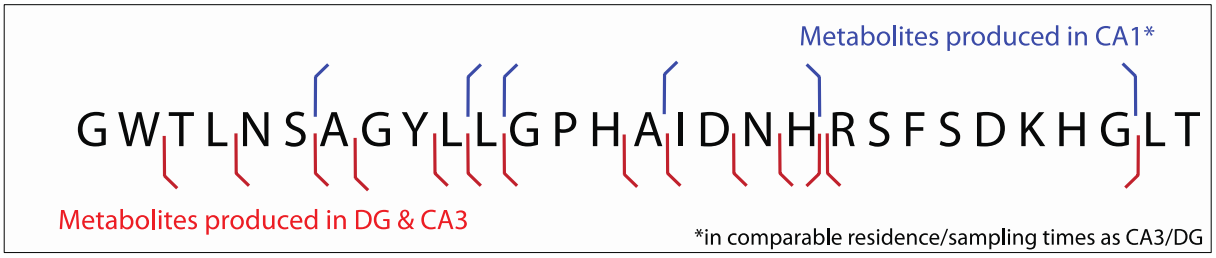

Figure 34. Galanin hydrolysis products found in the CA1, DG, and CA3 areas of the hippocampus

The diagonal portion of each line points towards the retained terminus in that fragment. Red lines represent galanin fragments found after sampling from the CA3 or DG areas. Blue lines represent fragments found after sampling from the CA1.

5.3.3 Ischemic Pre-conditioning

We verified that 30 minutes of OGD followed by 45 minutes of OGD 48 hours later initiates pre-conditioning through PI studies and will now call this treatment ischemic preconditioning. Figure 34 below shows images of non-treated controls and OHSCs that had been pre-conditioned.

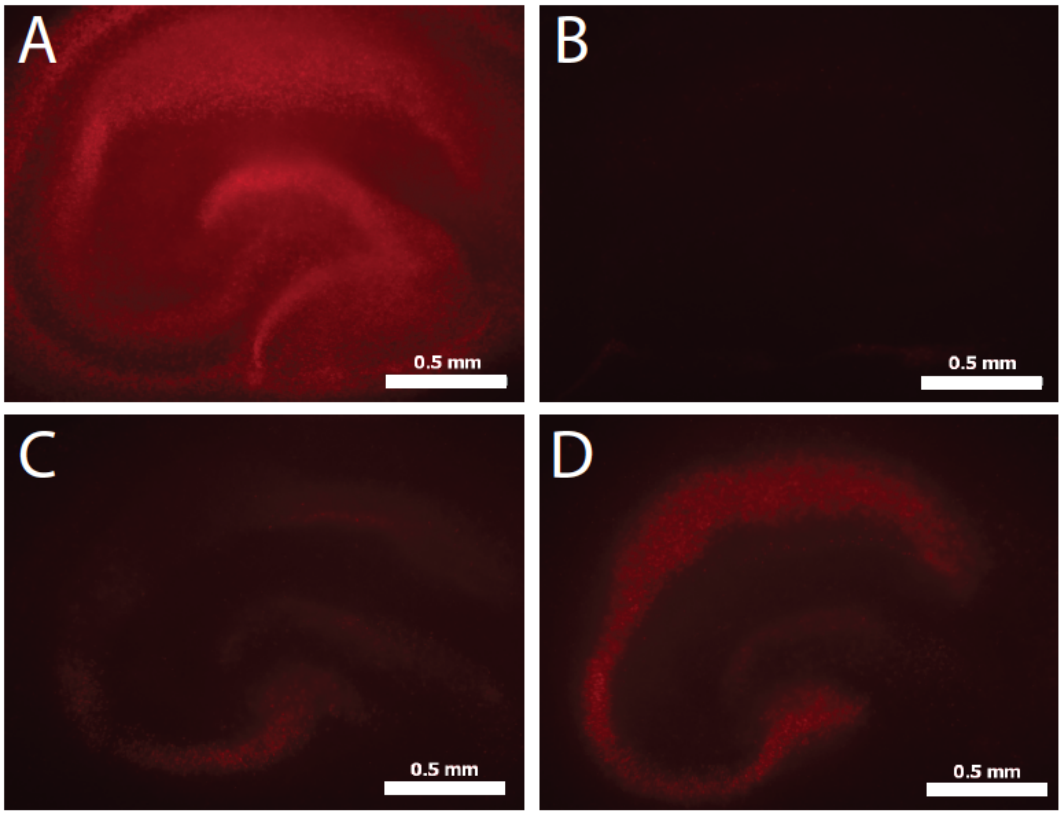

Figure 35. Ischemic pre-conditioned and non-conditioned tissues treated stained with PI

Tissues were stained with PI. (A) and (B) are positive and negative controls, respectively. (C) and (D) are pre-conditioned and non-treated OHSCs after 45 minutes of lethal OGD (48 hours after the first OGD exposure, at 72 hours, in Figure 32). Scales bars = 0.5 mm

Figure 36 below shows damage results in the CA1 and entire OHSC after lethal OGD. Ischemic preconditioning caused little damage (1.29 ± 0.57). Damage to the ischemically pre-conditioned CA1 after lethal OGD was 9.2 ± 1.2, and those that had not been pre-conditioned had a damage value of 19.3 ± 1.2. Thus, we conclude that by subjecting these OHSCs 30 minutes of submersion OGD, we are invoking mechanisms that protect the tissue when OGD is longer.

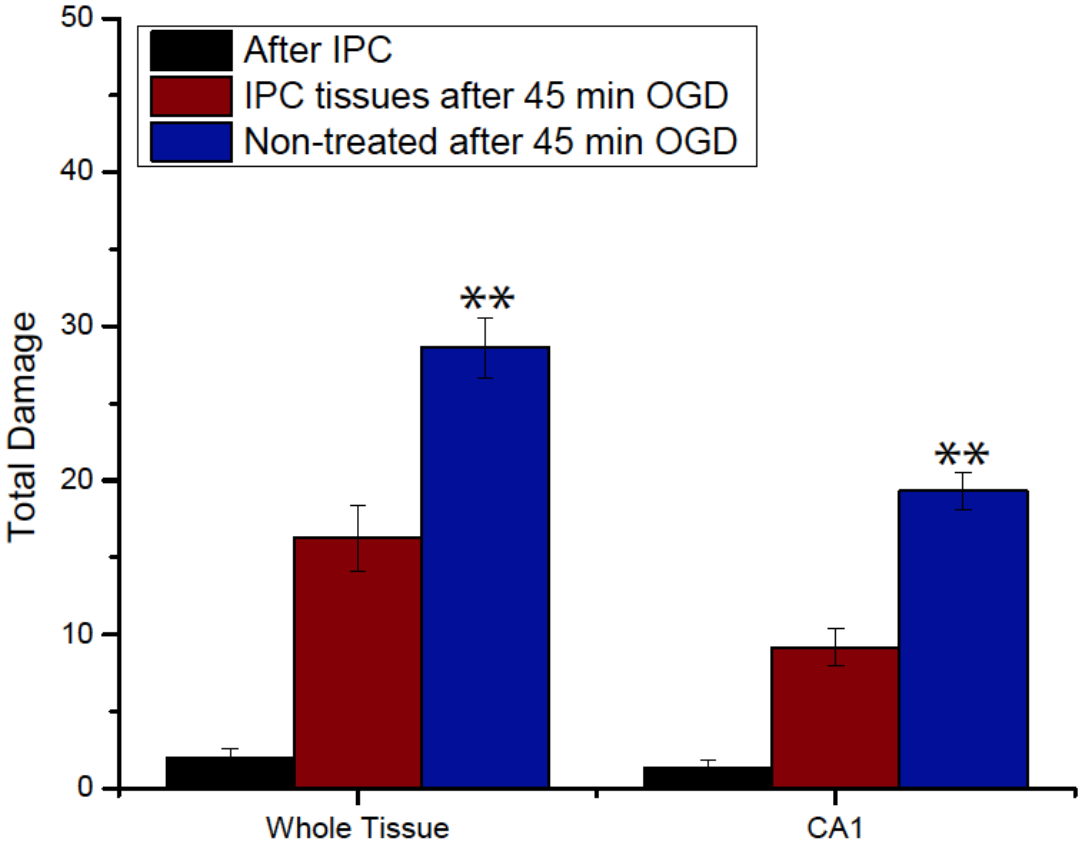

Figure 36. Total damage in ischemic pre-conditioning and non-treated tissues

Black bars represents total damage incurred from ischemic preconditioning, which was minimal. Pre-conditioned cultures (red bar) sustained less damage than non-ischemically preconditioned cultures (blue bar) after lethal OGD.

HPLC data revealed that galanin hydrolysis changes 24 hours after ischemic pre-conditioning. Figure 37 below shows the ratio of galanin to internal standard in the collection capillary for each of three target areas. We use $^{D}Y^{D}AG^{D}F^{D}L$ as an indicator of flow rate (see 'Quantifying Flow Rate', Chapter 4), show that the ratio of galanin to internal standard, [Gal]/[IS], is proportional to relative enzyme rates (Eqs. 11-13). Data was obtained over the course of three months, in optimization of the HPLC changed run times from 45 minutes to 15 minutes. Earlier experiments had a lower sample throughput, typically of control non-OGD cultures. In cases where statistical significance between treated and non-treated cultures was borderline ($0.05<p<0.15$), data from controls of other sets were combined with a particular set if ANOVA analysis verified that the two sets were not significantly different ($p > 0.5$). Figure 37

shows five data sets: 2 from CA3, 2 from DG, and one from CA1. The data from CA1 is actually two data sets that were combined. However, controls from the other two were not similar enough allow such treatment.

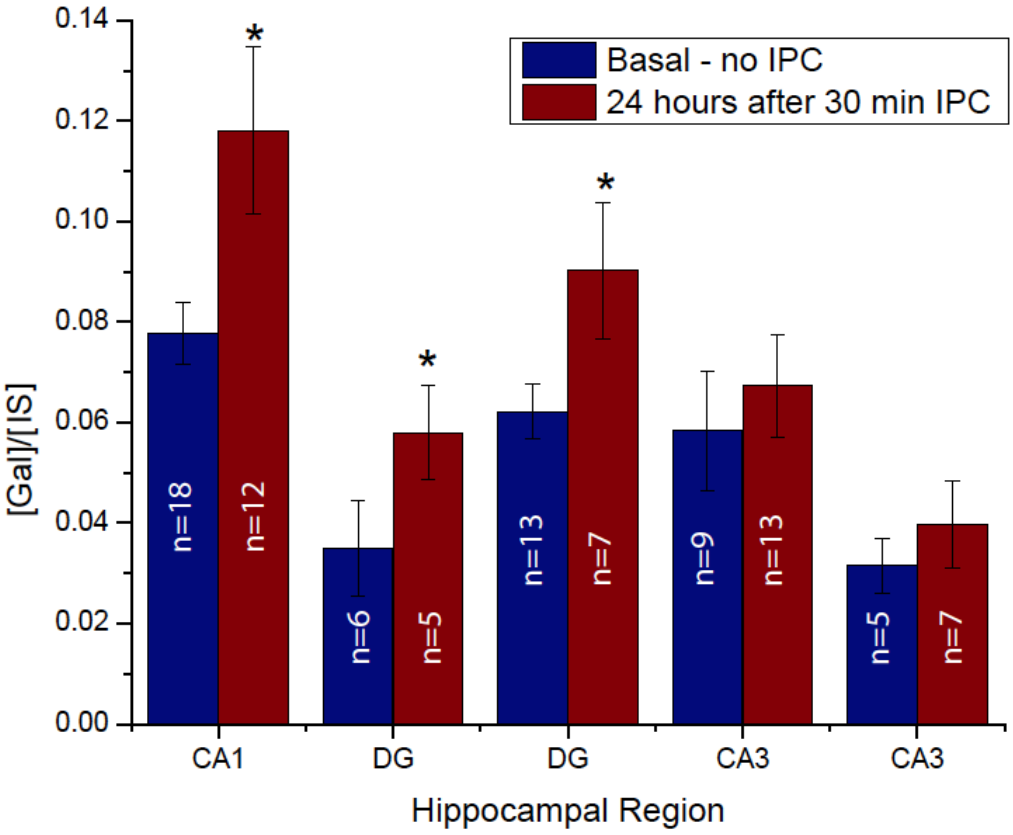

Figure 37. Ischemic-preconditioning decreases galanin hydrolysis in OHSC

Enzymatic rates are inversely proportional to the concentration of galanin to internal standard in the sample. Blue bars represent control non-ischemically preconditioned cultures and red bars are ratios in ischemically preconditioned cultures. Two CA1 data sets were combined, as controls were not significantly different from each other. Data from the DG and CA3 represent two different data sets each.

The increase in [Gal]/[IS] is significant in CA1 and DG samples, but not in those collected from the CA3. The variability in baseline enzymatic rates will be discussed at the end of this chapter.

5.3.4 Inhibitor Treatment

The chosen inhibitors were chosen based on previous enzymatic studies by us[54] and others[91]. Figure 38 below shows the results of all inhibitor studies.

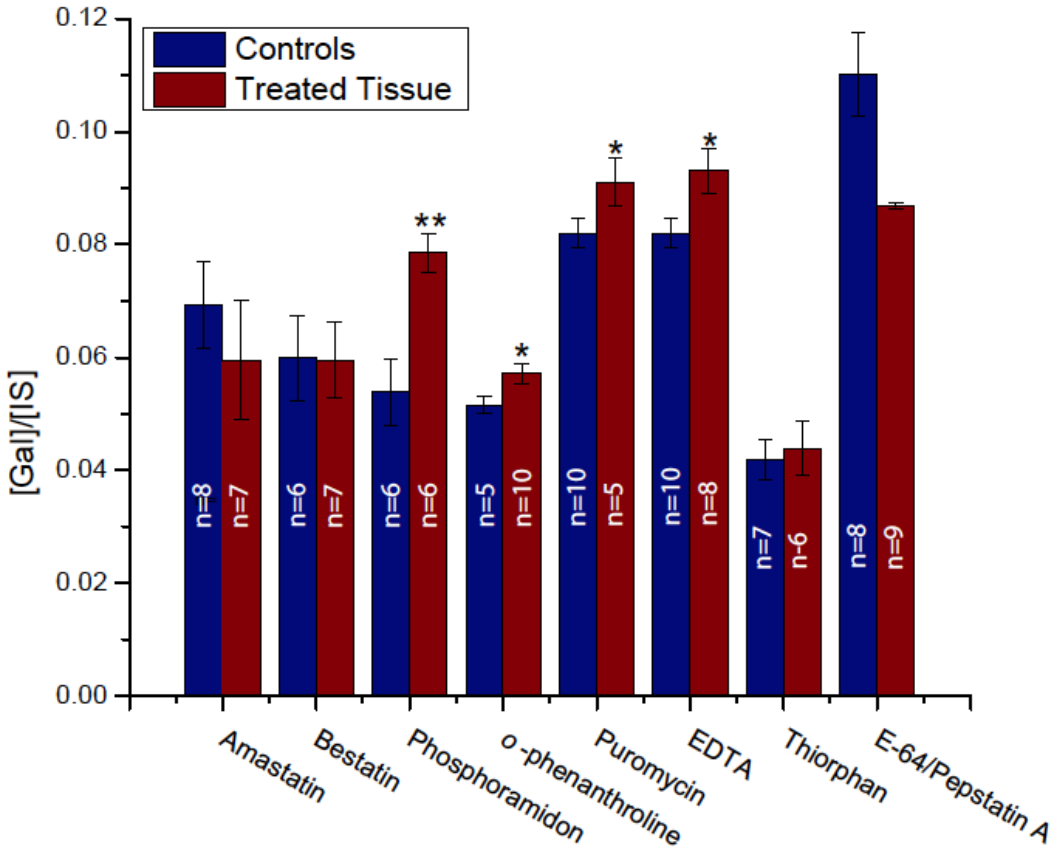

Figure 38. Galanin hydrolysis is inhibited by metal chelators and metalloenzymes inhibitors

Blue bars represent control non-treated cultures and red bars are ratios in cultures treated with the indicated inhibitor.

From Figure 38, we conclude that some galanin-degrading ectopeptidase activity in the OHSC CA1 region is that of metallopeptidases. Treatment with *o*-phenanthroline, a zinc chelator and EDTA, another metal ion chelator, both increased [Gal]/[IS]. Phosphoramidon also increased this ratio. Phosphoramidon is an inhibitor of neutral endopeptidase (3.4.24.11, NEP) and to a lesser extent, other metallopeptidases. However, thiorphan also inhibits NEP and had no effect. Thus, the effects seen in phosphoramidon treatment were likely from inhibition of

metallopeptidases. This inhibitor data agrees with the qualitative data obtained by MALDI-MS, which suggested that galanin-degrading enzymes were aminopeptidases. Many aminopeptidases are actually zinc metalloenzymes[12]. Aminopeptidase N/M (3.4.11.2) is inhibited by bestatin, as is aminopeptidase B (3.4.11.6). Aminopeptidase A (3.4.11.7) is inhibited by amastatin. Cysteine (3.4.21) and aspartic (3.4.23) proteases are inhibited by E-64 and pepstatin A, respectively. None of these treatments increased [Gal]/[IS]. Puromycin most notably inhibits puromycin-sensitive aminopeptidase N (APN, 3.4.11.14), however APN is primarily found in the cytosol (all inhibitor/peptidase information found on Merops Peptide Database, merops.sanger.ac.uk). However, a puromycin-sensitive neuron specific aminopeptidase (NAP), has been recently discovered in the CNS, and is most active in the rat hippocampus. One study shows it may protect neurons against the central cause of death in AD[105]. Perhaps the tropic activity of this galanin-degrading peptidase has some link to galanin neuroprotective activity.

The data presented in Figures 36 and 37 show variability in the baseline enzymatic rates from sample set to sample set. For example, the [Gal]/[IS] ratio in the 'amastatin' controls is about 0.07, where it is 0.11 in the 'E-64/pepstatin A' set. This variability is puzzling, and likely comes from the natural variability of biological samples. However, the variability does not undermine results. All cultures utilized in a single set were dissected, prepared, and cultured in tandem to one another under identical conditions.

6.0 CONCLUSION AND FUTURE DIRECTIONS

We have developed a novel method for sampling the extracellular space tissue culture type samples to fulfill a need for a spatially resolved sophisticated sampling technique these type of samples require. A primary advantage over push-pull perfusion is the fact probes can be positioned independently of each other and do not have to be inserted into the tissue (single capillary electroosmotic sampling) or use very small probes inserted into the tissue (push-pull electroosmotic sampling). We have extensively studied ways to minimize damage and perturbation of the tissue and illustrated the use of single capillary electroosmotic sampling and push-pull electroosmotic sampling to study enzymatic reactions in the hippocampus. In particular, we report for the first time on the activity of galanin-degrading enzymes in the hippocampus, showing that ischemic preconditioning involves mechanisms that decrease the rate of galanin hydrolysis in the extracellular space. Furthermore, we used inhibitors of various peptidases and fragmentation patterns to show that galanin-degrading enzymes in the hippocampus are likely aminopeptidases requiring metals (Zn) for catalysis.

As in push-pull perfusion and microdialysis, there is the drawback of sample bias. As in capillary electrophoresis (CE), analytes with a positive charge will; move faster through the extracellular space into the capillary and those with a negative charge will move away. Collection efficiencies will depend on the relative electrophoretic mobilities of the analyte, and the electric field strength overlap of each capillary in the tissue.

Push-pull electroosmotic sampling is just the start of routine use of electroosmotic sampling. Coupling the collection capillary to online analysis methods, for example, CE, would greatly decrease sample handling and throughput. If online analysis was available, the collection and source capillaries could conceivably be tapered and inserted into the tissue sampling only the neuronal layer instead of passing the sample through the glial cell layer in the push-pull electroosmotic sampling design presented here. Changes in galanin hydrolysis were measured 24 hours after ischemic preconditioning; however, full neuroprotective effects were measured 48 hours after ischemic preconditioning. Further studies should be conducted to see if the effects seen after 24 hours are strengthened as time goes on. Additionally, coupling ischemic

preconditioning with inhibitor studies may help identify those metallopeptidases that are responsible for the effects of ischemic preconditioning. To address the identity of the fragments, coupling MALDI or another mass spectrometric detection system could help identify and quantify peaks in a chromatogram that may be fragments of galanin. Finally, it would be interesting to see if the mRNA or expression of metallopeptidases is decreased following ischemic preconditioning.

APPENDIX A: ADDITIONAL FIGURES

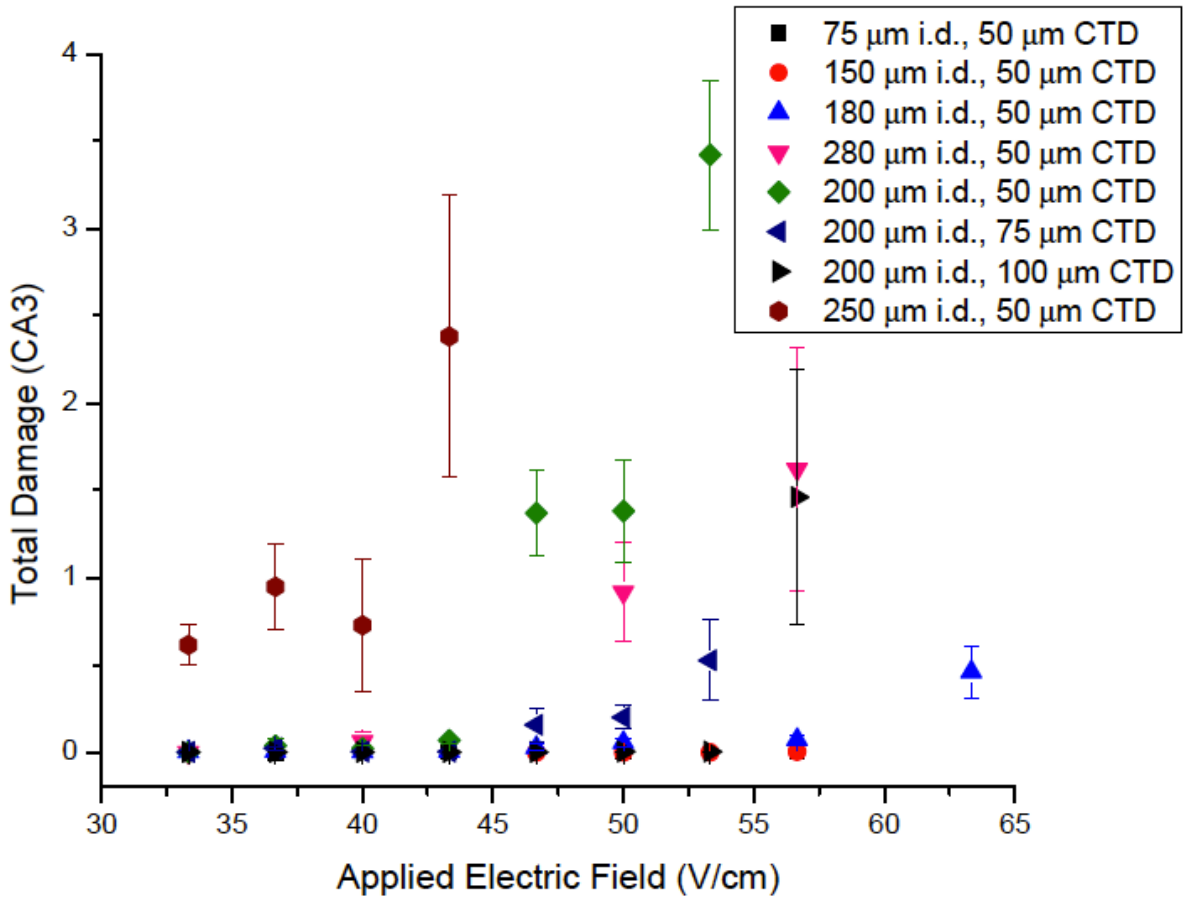

Figure A- 1. Total damage vs. applied electric field in single capillary electroosmotic sampling

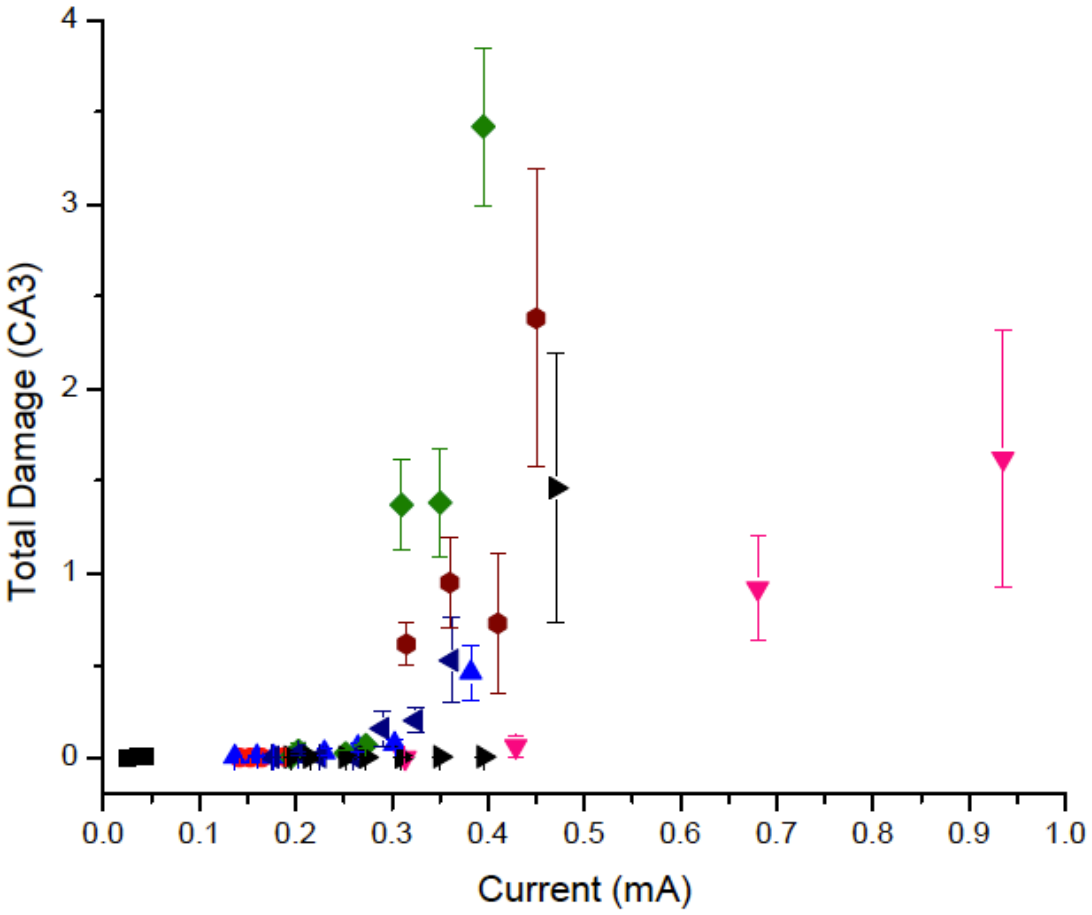

Figure A- 2. Total damage vs. induced current in single capillary electroosmotic sampling

Legend is the same as Figure A-1.

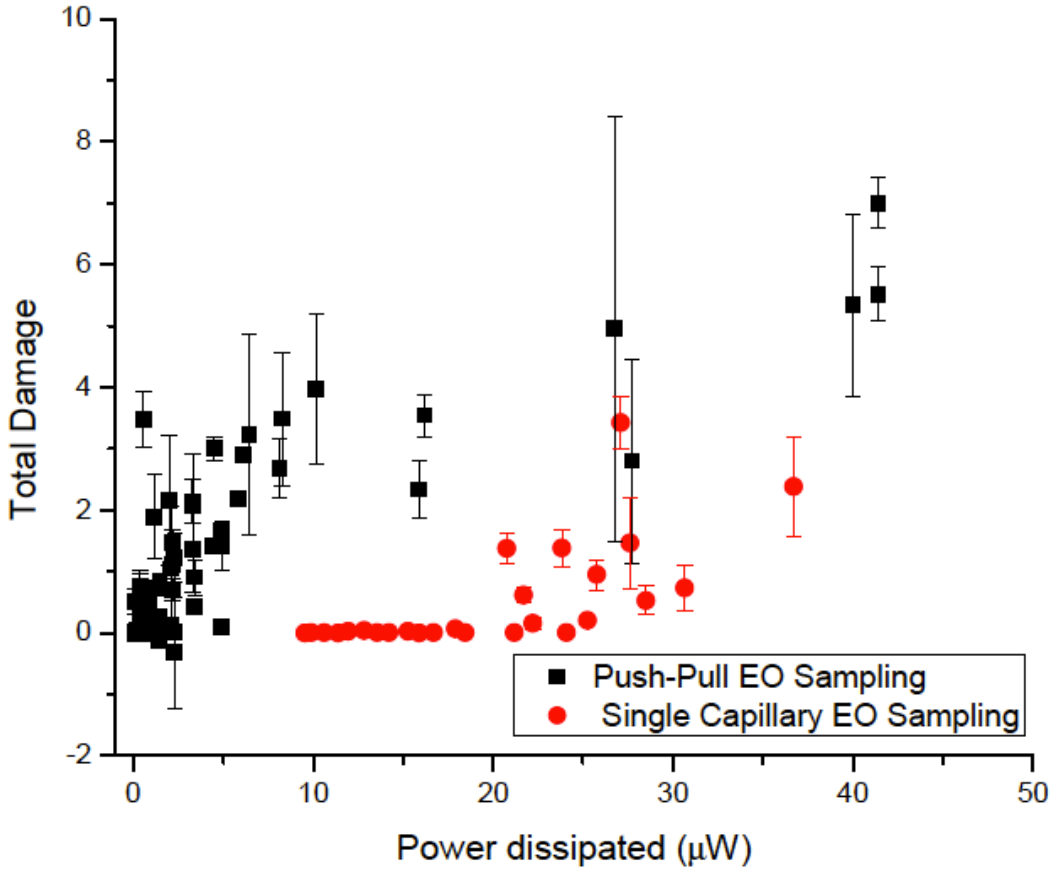

Figure A- 3. Total damage in the CA3 of a sampled OHSC with respect to power dissipated

Both push-pull electroosmotic sampling and single capillary electroosmotic sampling are shown here, and it is clear that while power has good correlation to damage within each geometry, it does not have correlation between both.

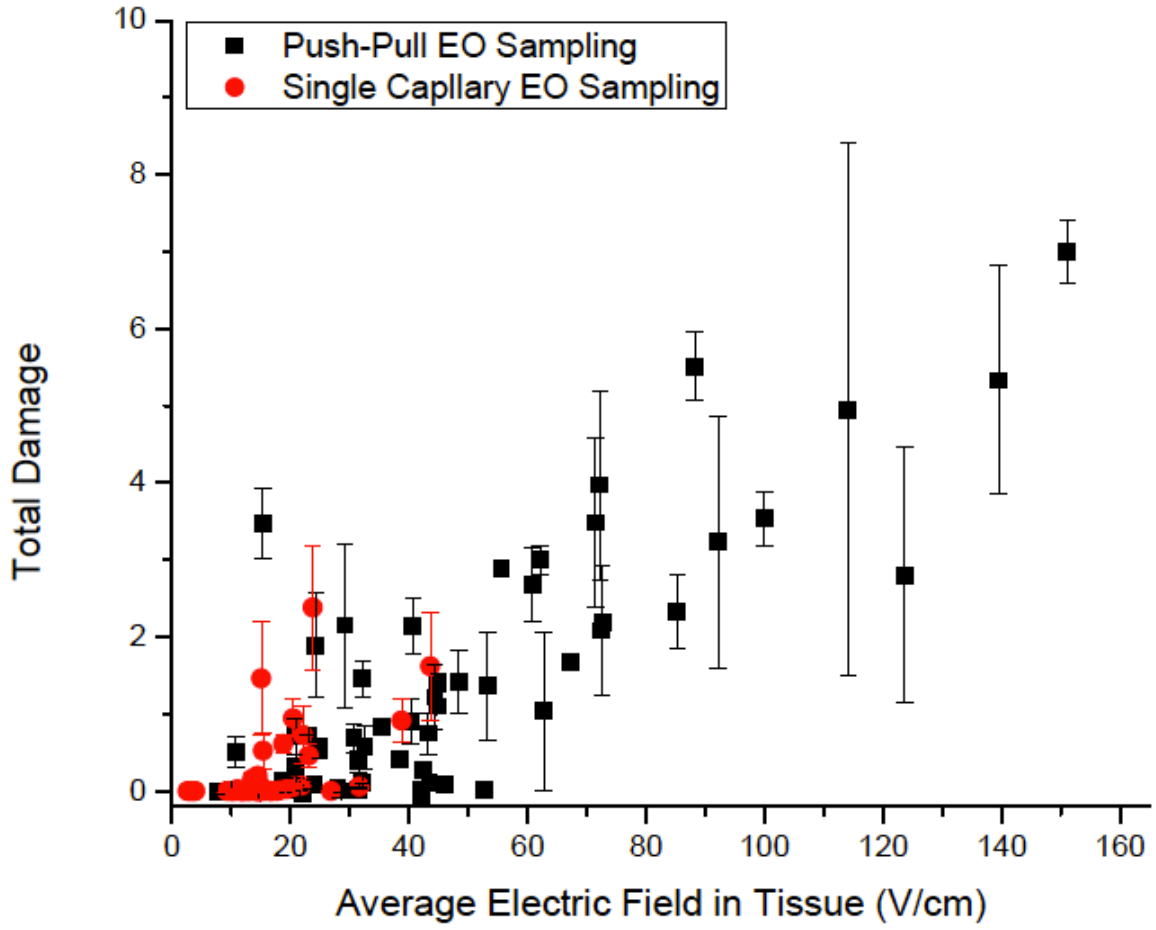

Figure A- 4. Total damage in the CA3 after electroosmotic sampling with respect to average electric field

Field in the tissue was calculated by dividing the voltage drop within the tissue by the distance. Values from both push-pull electroosmotic sampling and single capillary electroosmotic sampling are shown here.

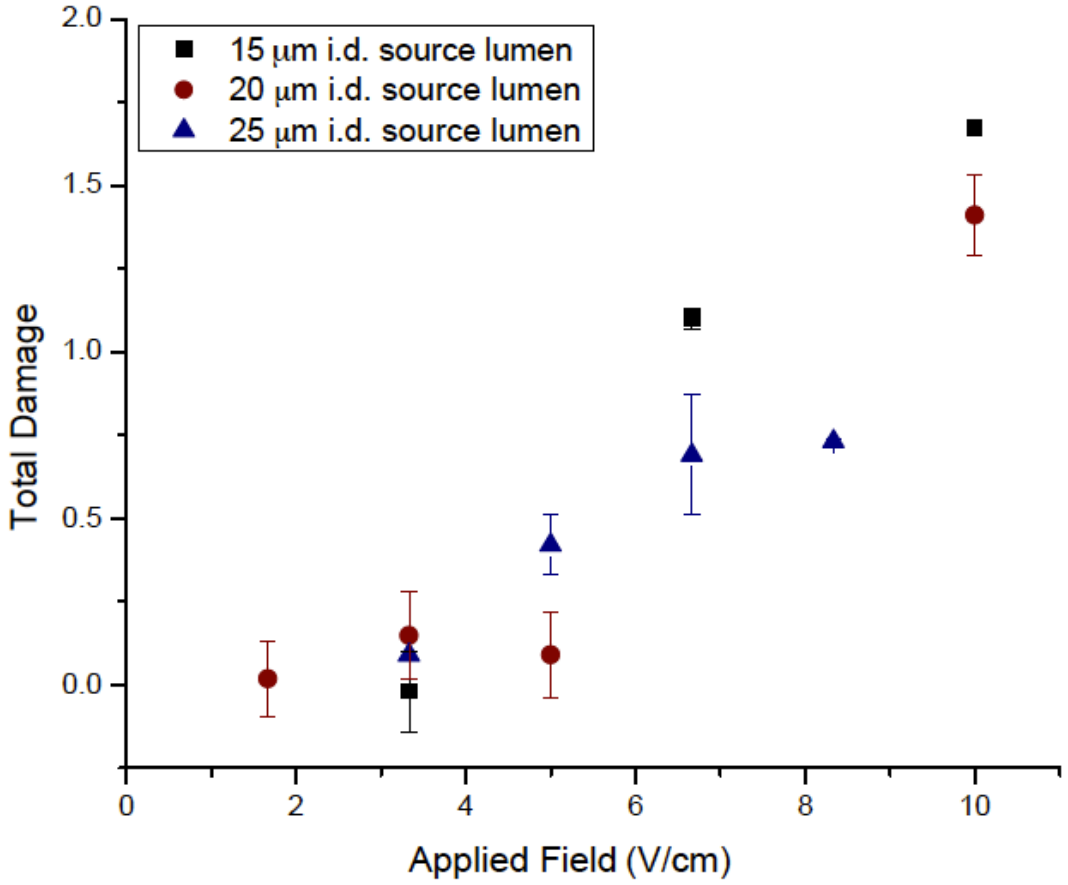

Figure A- 5. Damage versus applied voltage for three different source lumen inner diameters

The source barrel is 200 μm with the lumen (of above indicated size) inserted 40 μm below the surface. The collection capillary was 75 μm i.d. raised off the surface of the tissue 25 μm.

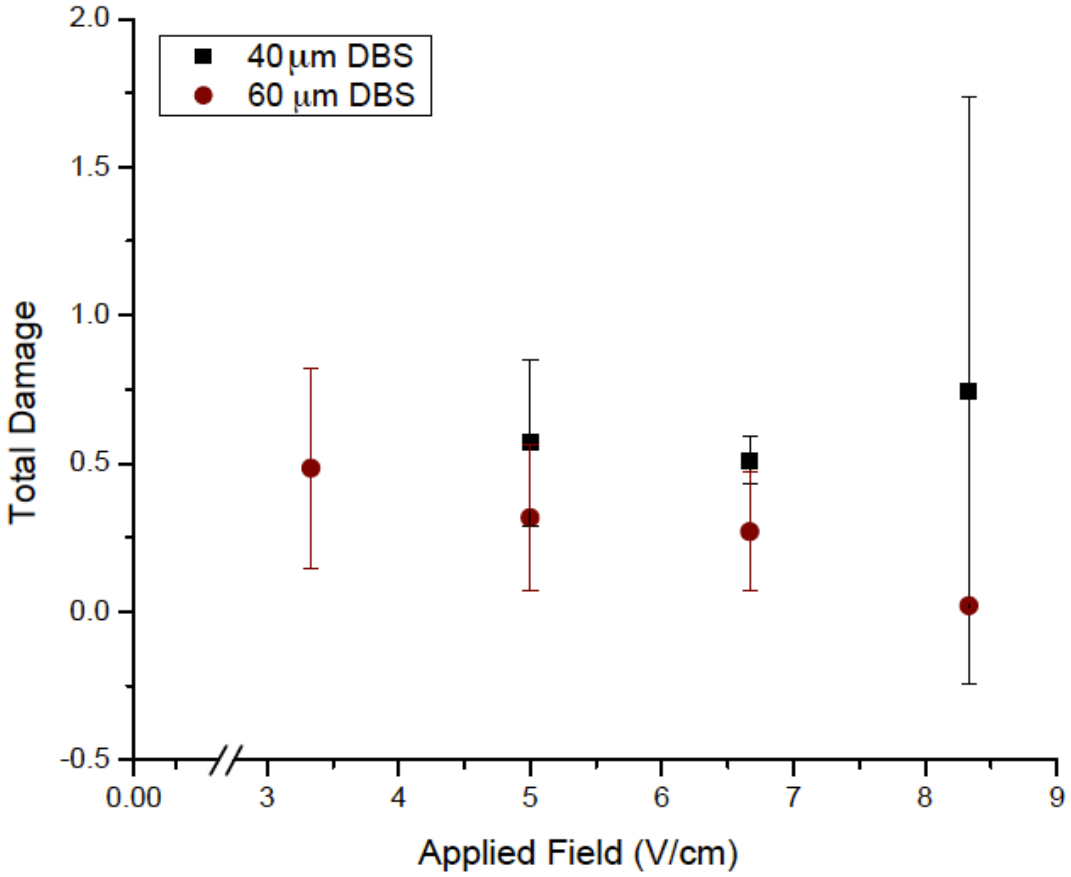

Figure A- 6. Damage versus applied voltage for two source capillary insertion depths

The source barrel is 200 µm with a 20 µm lumen inserted the indicated distance below the surface. The collection capillary was 75 µm i.d. raised off the surface of the tissue 25 µm.

APPENDIX B: DISCUSSION OF EQUATIONS USED IN COMSOL

COMSOL solves for the electric fields and voltage values for the push-pull 3D model identically as the single capillary, utilizing the differential equation $-\nabla(\sigma V) = Q$. The conductivity, σ, is likewise scaled with the same form factor, $\frac{\epsilon}{\lambda^2}$. COMSOL utilizes the Navier-Stokes equation to describe fluid flow in free solution and modifies it to the Brinkman equation when describing fluid flow in porous material (i.e. the tissue). These equations are valid only with respect to pressure driven flow, however, COMSOL allows modification of the Navier-Stokes to account for electroosmotic velocity in free solution (i.e. the capillaries). A preset option allows the walls of each capillary to be set as moving walls that support electroosmotic flow with a x-velocity of $\frac{\epsilon_w \zeta}{\eta} \cdot \vec{E}_x$, a y-velocity of $\frac{\epsilon_w \zeta}{\eta} \cdot \vec{E}_y$, and a z-velocity of $\frac{\epsilon_w \zeta}{\eta} \cdot \vec{E}_z$, where $\vec{E}_x$, $\vec{E}_y$ and $\vec{E}_z$ are the x, y, and z components of the electric field calculated in the 'Electric Currents' module. However, the module does not have a clear way to specify that the walls of the pores in a porous media like the tissue have a zeta potential. Thus, we turned to equations published by Scales, et al.[106], which described the transformation of the Navier-stokes equation (Equation A-1) into a form of the Brinkman equation valid for electroosmotic flow in porous media (Equation A-2).

$$\frac{\partial u}{\partial t} + u \cdot \nabla u = -\frac{\nabla P}{\rho_w} + \eta_e \nabla^2 u \quad \text{(A-1)}$$

$$\frac{\eta_e}{\sqrt{\tau}} \nabla^2 \frac{\bar{u}}{\varepsilon} - \frac{\eta_e \bar{u}}{K} = \frac{1}{\sqrt{\tau}\rho_w} (\nabla P + \rho_{eff} \nabla \phi) \quad \text{(A-2)}$$

Essentially, each spatial derivative in Equation A-2 was adjusted for tortuosity by the relationship $dx = \sqrt{\tau} dX$, where x is the actual winding distance a particle must travel to go through a pore, X is the thickness of the porous media, and τ is a dimensionless tortuosity equal to λ^2. The velocity that results from this conversion is u_{ave} or the adjusted linear velocity on a macroscopic scale. Then, to adjust for a 3-D matrix of pores, the substitution $u_{ave} = \bar{u}\frac{\sqrt{\tau}}{\epsilon}$ is made, where ϵ is porosity, and ū is the fluid flow in m/s. The del operator, ∇, can be rewritten as $\frac{d}{dX}$ and an electroosmotic term, $-\frac{\rho_{eff}\nabla\phi}{\rho_w\sqrt{\tau}}$, is added where ρ_w is the density of the solution (g/cm^3).

The tortuosity term appears as an adjustment of the spatial component of electric field from $\frac{dV}{dx}$ to $\frac{dV}{dX}$. In these equations, η_e is the kinematic viscosity (cm^2/s), κ is the permeability (m^2), P is pressure (Pa), ρ_{eff} is the effective charge density of the tissue, and ϕ is applied voltage (V). All of the constants in this equation are definable as follows: η is the dynamic viscosity of water, $4.9x10^{-4}$ Pa s. The tortuosity, τ, is 1.39 and the porosity (or volume fraction), ε , of immature rat brain is 0.41[63]. The kinematic viscosity is the dynamic viscosity, η, divided by the density, ρ_w, of water, 1 g/cm^2. Arifin, et al. defined a permeability of an adult rat brain using a porosity of 0.2[107]. We verified their calculated permeability by solving both Darcy's law (Equation A-3) and the Karman-Cozeny equation (Equation A-4) for pressure, setting them equal (Equation A-5) and solving for permeability (K, Equation A-6) for 10 μm round cell bodies.

$$\Delta P = v_o \frac{\eta \Delta x}{K} \text{ (A-3)}$$

$$\Delta P = \frac{180 v_o \eta \Delta x}{\phi_s^2 D_p^2} \frac{(1-\epsilon)^2}{\epsilon^3} \text{ (A-4)}$$

$$v_o \frac{\eta \Delta x}{K} = \frac{180 v_o \eta}{\phi_s^2 D_p^2} \frac{(1-\epsilon)^2}{\epsilon^3} \text{ (A-5)}$$

$$K = \frac{\phi_s^2 D_p^2}{180} \frac{\epsilon^3}{(1-\epsilon)^2} \text{ (A-6)}$$

Here, v_o is the superficial fluid velocity, ϕ_s is the shape factor, and D_p is the particle (or cell) radius. Once we were satisfied that this was a valid equation, we then found a permeability of tissue with 0.4 porosity and 30 μm pyramidal cells (shape factor 0.67) as $3.99x10^{-13}$ m^2. The voltage and pressure terms were computed by COMSOL. The only variable left undefined is the effective charge density.

Electroosmotic velocity can be generally defined according to Equation A-7.

$$v_{eo} = \frac{\varepsilon_w \zeta}{\eta} \nabla \phi \text{ (A-7)}$$

where ε_w is the permittivity of the solution in farad meters and ζ is the zeta potential in volts. If we transform this equation in the same fashion as the Navier-Stokes to reach an equation valid for fluid flow through porous media in a macroscopic 3-D scale, we change each *dx* to $dX\sqrt{\tau}$ and multiply v_{eo} by $\frac{\sqrt{\tau}}{\varepsilon}$, which we can then call ū. Thus we arrive at Equation A-8, solved for ū.

$$\bar{u} = \frac{\varepsilon \varepsilon_w \zeta}{\tau \eta} \nabla \phi \text{ (A-8)}$$

Returning to the modified Brinkman equation, Equation A-2, we solve for ū, assuming steady state, ignoring the pressure component (∇P), and changing the kinematic viscosity, η_e to dynamic viscosity, η.

$$\bar{u} = -\frac{K}{\eta\sqrt{\tau}}\rho_{eff}\nabla\phi \text{ (A-9)}$$

By setting Equation A-8 and Equation A-9 equal to each other, the effective charge density can be defined in terms of known variables, Equation A-10.

$$\rho_{eff} = \frac{-\varepsilon\varepsilon_w\zeta}{\sqrt{\tau}K} \text{ (A-10)}$$

Here, we can further define the zeta potential as -22.4 mV[53, 61]. This Brinkman equation reverts back to the Navier-stokes equation when the porosity and tortuosity are defined as 1 and zeta potential set to zero.

COMSOL utilizes the Brinkman equation in the format according to Equation A-11.

$$\left(\frac{\eta}{K} + Q\right)\bar{u} = \nabla\cdot\left[-pI + \left(\frac{1}{\varepsilon}\right)\left\{\eta(\nabla\bar{u} + (\nabla\bar{u})^T) - \left(\frac{2\eta}{3} - k_{dv}\right)(\nabla\cdot\bar{u})I\right\}\right] + F \text{ (A-11)}$$

If you multiply Equation A-11 by $\rho_w\sqrt{\tau}$, all the constants in Equation A-11 match correctly to Scales' derived Brinkman equation except for permeability, K, which differs by a factor of $K_{eqA-2} = \frac{K_{eqA-11}}{\sqrt{\tau}}$. The force term, F, has an x, y and z component which we have defined as $-\rho_{eff}\cdot\vec{\mathrm{E}}_x$ and $-\rho_{eff}\cdot\vec{\mathrm{E}}_y$, and $-\rho_{eff}\cdot\vec{\mathrm{E}}_z$ respectively.

In the capillaries (subdomain A, B, and C) and HBSS plug under the collection capillary (subdomain D) in Figure 21, the Navier-Stokes equation is used. In subdomain E, the tissue, the Brinkman equation is used.

APPENDIX C: FITTING FLUORESCENCE CURVES TO A MODEL

Nicholson & Tao[69] report that optical detection of fluorescence by any objective lens is a convolution of a square function (or linear increase with time) and a sinc function (Equation A-17).

$$S(r` = 0; z') = \frac{\sin(\frac{kaz'}{2})}{\frac{Mkaz'}{2}} \text{ (A-17)}$$

where $k = \frac{2\pi}{\lambda_w}$, $a = \frac{M^2}{2n}\sin^2\Theta'$, $\Theta' = \tan^{-1}\frac{nL(M+1)\tan\Theta}{L(M+1)}$, $z' = \frac{LM^2z}{(nL+M^2z)}$, $\Theta = \sin^{-1}\frac{NA}{n}$, and n is the refractive index, M is the magnification, L is the optical tube length of the microscope, NA is the numerical aperture, z is the distance above the focal plane and λ_w is the wavelength of the light in vacuum.

Figure A-7 shows S(r`=0; z)M^2, tailored to our image capturing parameters (λ_w=620nm, NA=0.16, n=1 (air), L=160 mm, M=4).

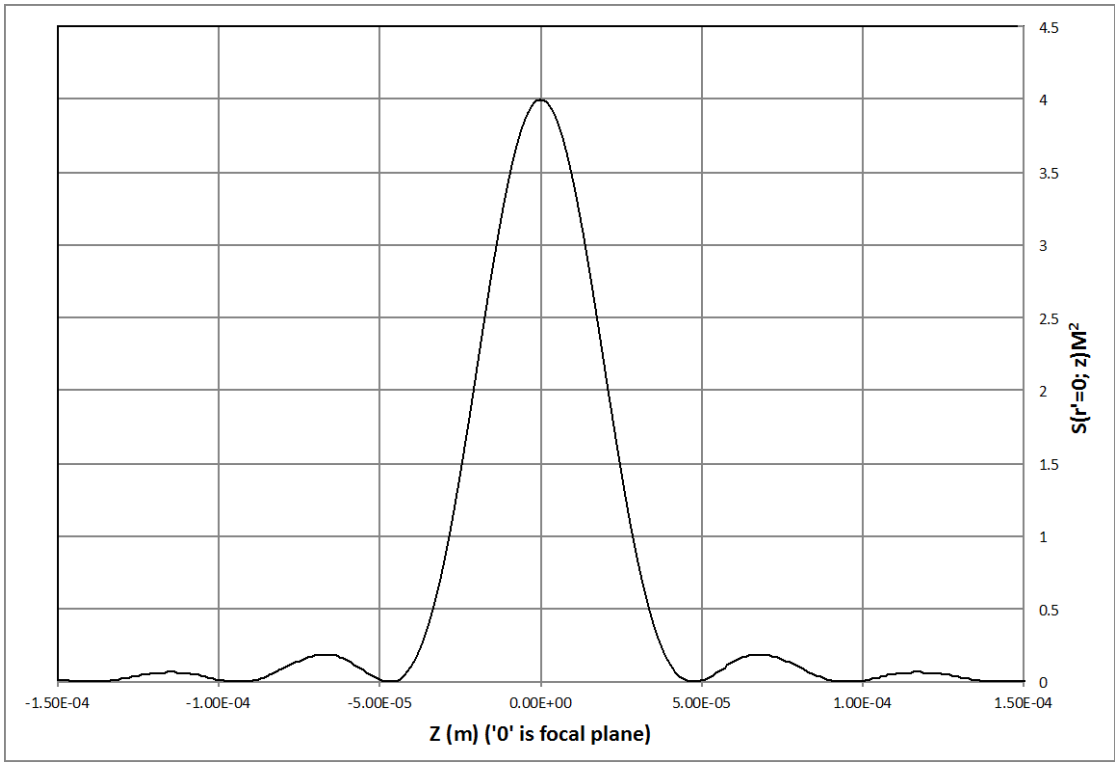

Figure A- 7. Sinc Function to Describe Detection Range of 4x Objective Lens

The z-axis corresponds to the distance above and below the focal plane (z=0). By multiplying the sinc function with a simple square function, a curve, shown in Figure A-6, emerges similar to those seen in Figure 22.

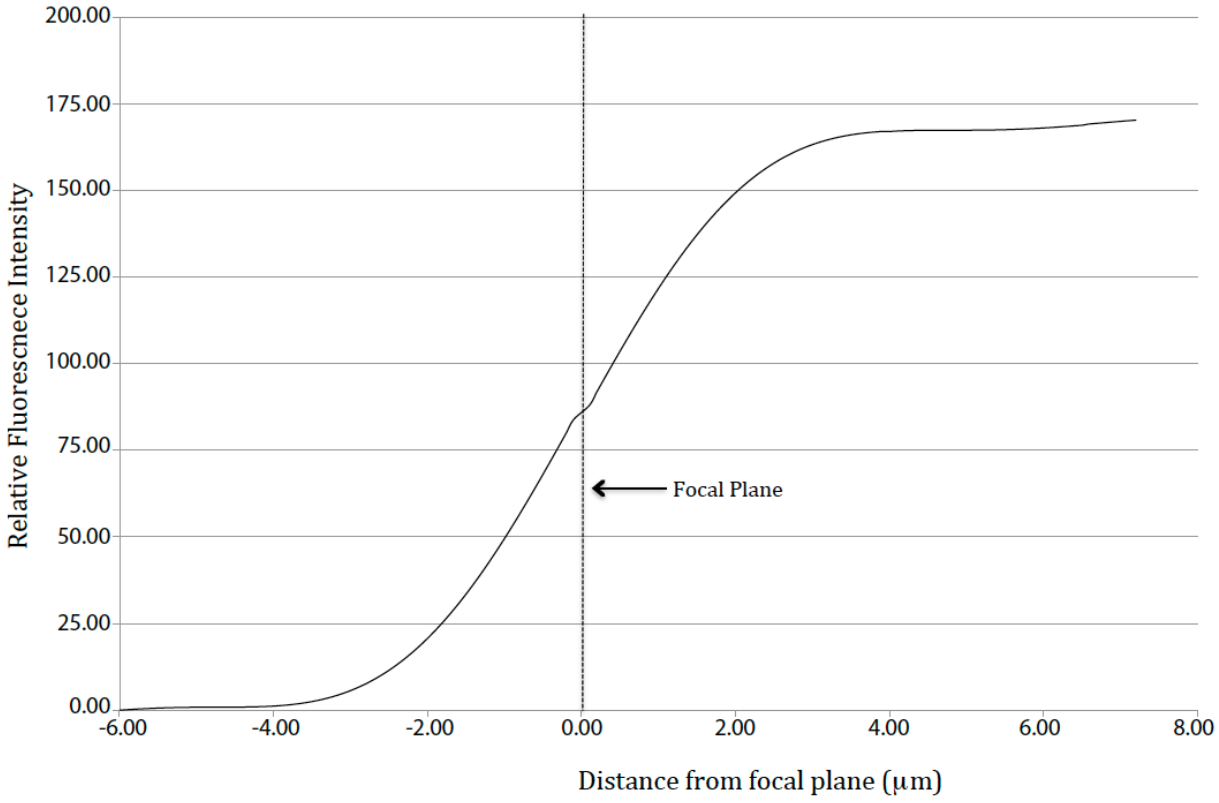

Figure A- 8. Modeled increase in TR3 fluorescence intensity in lumen of the collection capillary

Equation A-17 is multiplied by a step function for a 4x air objective with an NA of 0.016 and L of 180 mm detecting an emission λ of 620 nm. This is strikingly similar to the experimentally acquired curves in Figure 22, except that the initial delay in fluorescence is a bit shorter. By fitting the distance at half maximum on this curve to the time at half maximum of the experimental curves, the flow rate of the fluophore as it fills up the collection capillary can be determined.

Experimental curves, such as the one shown in Figure 22, can be fit to the template curve in Figure A-8. Half maximum intensity of the template curve occurs at z=0, or 46 µm into the 'cylinder of maximum detection'. To fit, we divide this distance, which corresponds to a volume of 0.36 nL in a 100 µm i.d. collection capillary, by the time at half maximum intensity of the experimental curves. If it took 30 seconds, for example, the flow rate would be 0.72 nL/min. However, in order for this calculation to work, the time vs. fluorescence intensity curve must plateau before the end of sampling (10 minutes). This was not always the case – rather most curves did not plateau and were similar to those shown in Figure A-9.

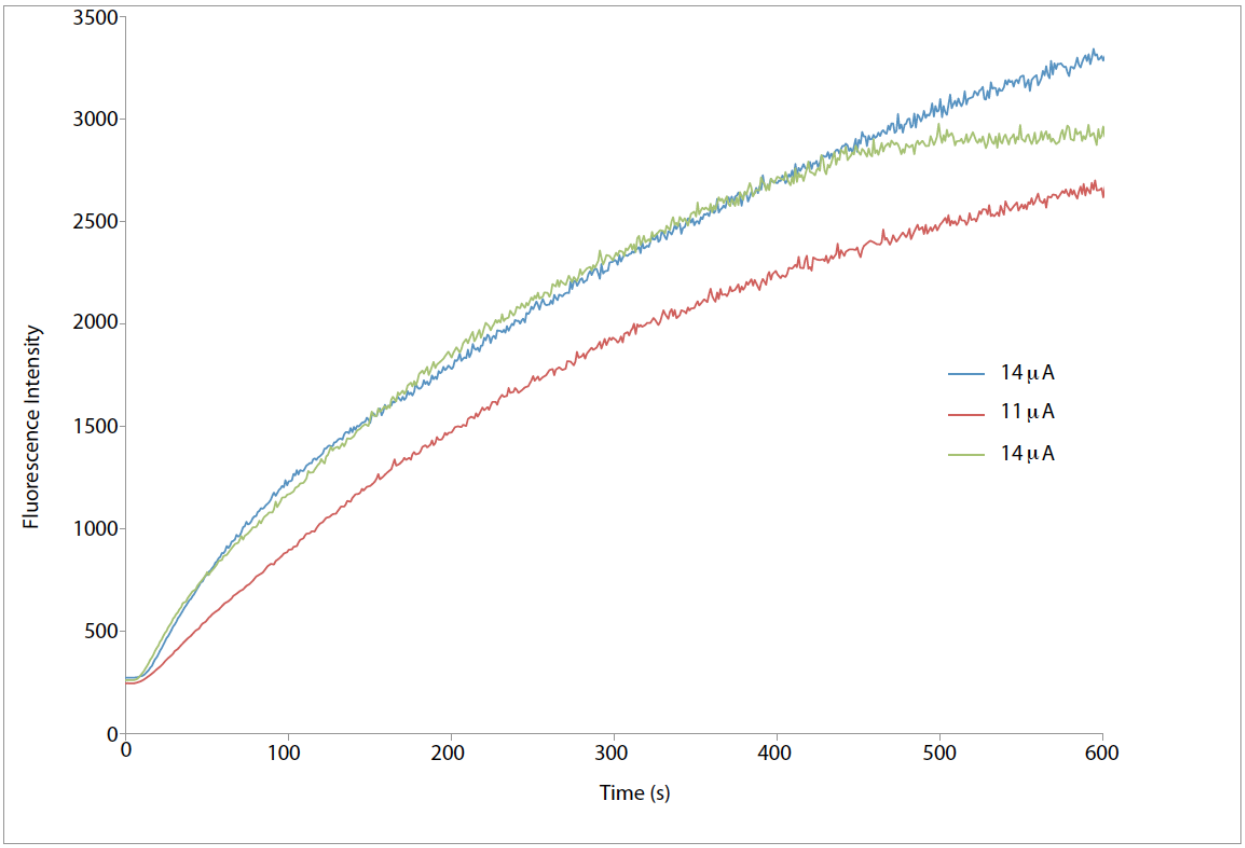

Figure A- 9. Fluorescence accumulation in collection capillary with respect to time sampled

Sampling was done with a 200 µm source barrel with a 22 µm tip, and a 100 µm collection capillary. The capillary-to-tissue distance was 25 µm and the DBS was 60 µm. The red and blue lines represent two different sampling fields where the fluorescence never plateaued, where in similar sampling conditions (green line) a plateau in florescence was reached. The accumulation as detected from below by TR3 migration is quite variable and difficult to analyze via the Nicholson and Tao model.

If a plateau is never reached, 92 µm of the 100 µm cylinder of detection, or 0.72 nL was not yet fully filled with TR3 at the end of 10 minutes. This calculates to a flow rate of less than 0.07 nL/min, and much lower than what is calculated by actual capillary contents through HPLC. The green trace, which has a time and half maximum fluorescence of 112 seconds, indicates a flow rate of ~0.2 nL/min, still much lower than previous estimates. Thus analysis of TR3 fluorescence via the Nicholson and Tao model is not adequate to quantify flow rates.

APPENDIX D: A SIMPLE MODEL OF RESISTANCE

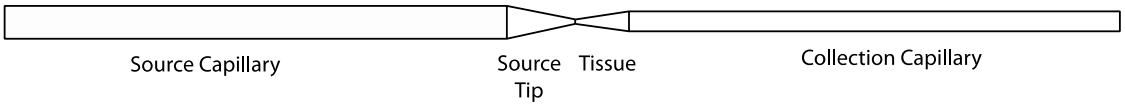

Figure A- 10. Simple resistance model for calculating voltage drop across the tissue

By treating these components like resistors in a series, we can calculate the percentage of the total voltage that is dropped across the tissue. This represents the path of the electroosmotic flow and current in push-pull electroosmotic sampling. We disregard the contribution of the HBSS layer between tissue and collection capillary, as this does not add any significant resistance to the overall resistance of the system.

The x-axis of Figure 27 is the average electric field within the tissue, calculated by dividing the COMSOL-calculated voltage drop by the distance in the tissue between the capillary lumen. Thus, using a simple resistance model, we can calculate an estimate of this value for parameters outside those specified in Figure 26 and Figure 27 according to the following equations.

$$R_{sourcecapillary} = \frac{1}{\sigma}\frac{l_{sourcecapillary}}{\pi r_{sourcecapillary}{}^2} \text{ (A-18)}$$

$$R_{sourcetip} = \frac{1}{\sigma}\frac{l_{sourcetip}}{\pi r_{sourcecapilary} r_{sourcetip}} \text{ (A-19)}$$

$$R_{tissue} = \beta\frac{1}{\sigma}\frac{l_{tissue}}{\pi r_{sourcetip} r_{collectioncapillary}} \text{ (A-20)}$$

$$R_{collectioncapillary} = \frac{1}{\sigma}\frac{l_{collectioncapillary}}{\pi r_{collectioncapilary}{}^2} \text{ (A-21)}$$

where σ is the conductivity of the electrolyte filling the capillaries, and the subscript of 'r' or 'l' specifies the radius or length (respectively) of that particular component of the model. The 'length' of the tissue can be calculated using the math in Figure 17. We are treating the source tip and the tissue like truncated cones. β is a correction factor that includes tissue dimensions and tissue properties. Current is actually not restricted to a cone, so the true resistance is lower than that of the cone approximation. The tissue's porosity and tortuosity increase resistivity, so the true resistivity of the tissue is higher (conductivity, σ, is lower) than expressed in equation A-20 without the β factor. These effects tend to counteract each other, so we expect β to be not too different from unity.

$$\frac{E_t}{E_{app}} = \frac{R_{tissue}}{(R_{sourcecapillary}+R_{sourcetip}+R_{tissue}+R_{collectioncapillary})l_{tissue}} \quad \text{(A-22)}$$

The factor β was found to be 0.6 by forcing calculated values (Equation A-22) to equal those in Figure 26 corresponding to the middle values of each radius ($\frac{E_t}{E_{app}} = 7.71 \times 10^{-5}$ for a 200 μm i.d. source barrel, 20 μm source tip, 75 μm i.d. collection capillary).

REFERENCES

1. Gaddum, J. H., *Journal of Physiology* **1958,** *155* (1), 1P-2P.
2. Ungerstedt, U.; Hallstrom, A., *Life sciences* **1987,** *41* (7), 861-4.
3. Redgrave, P., *Pharmacology, Biochemistry and Behavior* **1977,** *6* (4), 471-4.
4. Dluzen, D. E.; Ramirez, V. D., *Pharmacology Biochemical Behavior* **1986,** *24* (1), 147-50.
5. Delgado, J.; DeFeudis, F.; Roth, R.; Ryugo, D.; Mitruka, B., *Archives Internationales de Oharmacodynamie et de Therapie* **1972,** *198* (1), 9-21.
6. Delgado, J.; Lerma, J.; Martin del Rio, R.; Solis, J., *Journal of Neurochemistry* **1984,** *42* (5), 1218-28.
7. Zhang, X.; Myers, R. D.; Wooles, W. R., *Journal of neuroscience methods* **1990,** *32* (2), 93-104.
8. Zhang, X.; Wulfert, E.; Hanin, I., *Journal of Neuroscience Methods* **1992,** *42* (1-2), 139-47.
9. Westerink, B., *Trends Analytical Chemistry* **1992,** *11* (5), 176-82.
10. Wang, Y.; Wong, S. L.; Sawchuk, R. J., *Pharmaceutical Research* **1993,** *10* (10), 1411-19.
11. Myers, R.; Adell, A.; Lankford, M., *Neuroscience and Biobehavoral Reviews* **1998,** *22* (3), 371-87.
12. Kennedy, R. T.; Thompson, J. E.; Vickroy, T. W., *Journal of neuroscience methods* **2002,** *114* (1), 39-49.
13. Lonnroth, P.; Jansson, P. A.; Smith, U., *The American journal of physiology* **1987,** *253* (2 Pt 1), E228-31.
14. Trickler, W. J.; Miller, D. W., *Journal of Pharmaceutical Sciences* **2003,** *92* (7), 1419-1427.
15. Di Chiara, G., *Trends in Pharmacological Sciences* **1990,** *11* (3), 116-21.
16. Bowser, M.; Kennedy, R., *Electrophoresis* **2001,** *22* (17), 3668-3676.
17. Lada, M.; Vickroy, T.; Kennedy, R., *Analytical Chemistry* **1997,** *69* (22), 4560-5.
18. Humpel, C.; Ebendal, T.; Olson, L., *Journal of Molecular Medicine* **1996,** *74* (9), 523-526.
19. Lisi, T.; Westlund, K.; Sluka, K., *Journal of neuroscience methods* **2003,** *126* (2), 187-194.
20. Kottegoda, S.; Shaik, I.; Shippy Scott, A., *Journal of neuroscience methods* **2002,** *121* (1), 93-101.
21. Kottegoda, S.; Pulido, J.; Thongkhao-on, K.; Shippy, S., *Molecular Vision* **2007,** *13*, 2073-2082.
22. Thongkhao-on, K.; Wirtshafter, D.; Shippy, S., *Pharmacology, Biochemistry and Behavior* **2008,** *89* (4), 591-597.
23. Patterson, E.; Pritchett, J.; Shippy, S., *Analyst* **2009,** *134* (2), 401-406.

24. Duo, J.; Fletcher, H.; Stenken, J. A., *Biosensors and Bioelectronics* **2006,** *22* (3), 449-457.
25. Fletcher, H.; Stenken, J., *Analytica Chimica Acta* **2008,** *620* (1-2), 170-175.
26. Wang, Y.; Stenken, J., *Analytica Chimica Acta* **2009,** *651* (1), 105-111.
27. Roy, M.; Ikimura, K.; Nishino, H.; Naito, T., *Analytical Biochemistry* **2010,** *399* (2), 305-307.
28. Takeda, S.; Sato, N.; Ikimura, K.; Nishino, H.; Rakugi, H.; Morishita, R., *Neuroscience* **2011,** *186*, 110-119.
29. Wang, M.; Roman, G. T.; Schultz, K.; Jennings, C.; Kennedy, R. T., *Analytical Chemistry* **2008,** *80* (14), 5607-5615.
30. Slaney, T.; Nie, J.; Hershey, N.; Thwar, P.; Linderman, J.; Burns, M.; Kennedy, R., *Analytical Chemistry* **2011,** *83* (13), 5207-5213.
31. Fillenz, M., *Neuroscience Biobehavioral Reviews* **2005,** *29* (6), 949-962.
32. Olson, R. J.; Justice, J. B., Jr., *Analytical Chemistry* **1993,** *65* (8), 1017-22.
33. Menacherry, S.; Hubert, W.; Justice, J. B., Jr., *Analytical Chemistry* **1992,** *64* (6), 577-83.
34. Hopwood, S., E.; Parkin Mark, C.; Bezzina Elizabeth, L.; Boutelle Martyn, G.; Strong Anthony, J., *Journal of Cerebral Blood Flow Metabolism* **2005,** *25* (3), 391-401.
35. Yang, H.; Wang, Q.; Elmquist, W. F., *Pharmaceutical Research* **1996,** *13* (10), 1570-1575.
36. Stoppini, L.; Buchs, P.; Muller, D., *Journal of neuroscience methods* **1991,** *37* (2), 173-82.
37. Gahwiler, B.; Thompson, S.; Muller, D., *Current Protocols in Neuroscience* **2001,** *Chapter 6*, Unit 6 11.
38. Holopainen, I., *Neurochemical Research* **2005,** *30* (12), 1521-1528.
39. Del Turco, D.; Deller, T., *Methods in Molecular Biology* **2007,** *399* (Neuroprotection Methods and Protocols), 55-66.
40. Poulsen, F.; Blaabjerg, M.; Montero, M.; Zimmer, J., *Brain Research* **2005,** *1051* (1-2), 35-49.
41. Debanne, D.; Gahwiler, B. H.; Thompson, S. M., *Journal of Physiology* **1998,** *507* (1), 237-247.
42. Barth, A.; Nguyen, L.; Barth, L.; Newell, D., *Experimental Brain Research* **2005,** *161* (3), 351-357.
43. Noraberg, J., *Alternatives to Laboratory Animals* **2004,** *32* (4), 329-337.
44. Takahashi, M.; Liou, S.-Y.; Kunihara, M., *Brain Research* **1995,** *675* (1,2), 249-56.
45. Cimarosti, H.; Henley, J., *Neuroscientist* **2008,** *14* (6), 626-636.
46. Vornov, J.; Park, J.; Thomas, A., *Experimental Neurology* **1998,** *149* (1), 109-122.
47. Laake, J.; Haug, F.; Wieloch, T.; Ottersen, O., *Brain Research Protocols* **1999,** *4* (2), 173-84.
48. Simao, F.; Zamin Lauren, L.; Frozza, R.; Nassif, M.; Horn Ana, P.; Salbego Christianne, G., *Neurological Research* **2009,** *31* (10), 1044-8.
49. Holopainen, I.; Kukko-Lukjanov, T.; Lopez-Picon, F., *Trends in Neurochemistry Research* **2005**, 145-164.
50. Nakagami, Y.; Saito, H.; Matsuki, N., *Japanese Journal of Pharmacology* **1997,** *75* (4), 319-326.
51. Shiekhattar, R.; Bibbs, E.; Schowen, R.; Adams, R., *Neuroscience Letters* **1990,** *111* (1-2), 189-94.

52. Bradberry, C.; Sprouse, J.; Sheldon, P.; Aghajanian, G.; Roth, R., *Journal of neuroscience methods* **1991,** *36* (1), 85-90.
53. Guy, Y.; Muha, R.; Sandberg, M.; Weber, S., *Analytical Chemistry* **2009,** *81* (8), 3001-3007.
54. Xu, H.; Guy, Y.; Hamsher, A.; Shi, G.; Sandberg, M.; Weber, S., *Analytical Chemistry* **2010,** *82* (17), 7521.
55. *The hippocampus book*. Oxford University Press: New York, New York, U.S.A., 2007.
56. Fuller, L., *Cold Spring Harbor Protocols* **2007**.
57. Gahwiler, B.; Capogna, M.; Debanne, D.; McKinney, R.; Thompson, S., *Trends in Neuroscience* **1997,** *20* (10), 471-477.
58. Gogolla, N.; Galimberti, I.; DePaola, V.; Caroni, P., *Nature Protocols* **2006,** *1* (3), 1165-1171.
59. Hailer, N. P.; Jarhult, J. D.; Nitsch, R., *Glia* **1996,** *18* (4), 319-31.
60. Guy, Y.; Rupert Amy, E.; Sandberg, M.; Weber Stephen, G., *Journal of neuroscience methods* **2011,** *199* (1), 78-81.
61. Guy, Y.; Sandberg, M.; Weber, S., *Biophysical Journal* **2008,** *94* (11), 4561-4569.
62. Nolkrantz, K.; Farre, C.; Brederlau, A.; Karlsson, R.; Brennan, C.; Eriksson, P.; Weber, S.; Sandberg, M.; Orwar, O., *Analytical Chemistry* **2001,** *73* (18), 4469-4477.
63. Kilb, W.; Dierkes, P. W.; Sykova, E.; Vargova, L.; Luhmann, H. J., *Journal of Neuroscience Research* **2006,** *84* (1), 119-129.
64. Shen, P.-J.; Yuan, C.-G.; Ma, J.; Cheng, S.; Yao, M.; Turnley, A.; Gundlach, A., *Neuropeptides* **2005,** *39* (3), 201-205.
65. Butler, T.; Self, R.; Smith, K.; Sharrett-Field, L.; Berry, J.; Littleton, J.; Pauly, J.; Mulholland, P.; Prendergast, M., *Neuroscience* **2010,** *165* (2), 525-534.
66. Pugh, P. C.; Zhou, X.; Jayakar, S. S.; Margiotta, J. F., *Developmental Biology* **2006,** *291* (1), 182-191.
67. Hamsher, A.; Xu, H.; Guy, Y.; Sandberg, M.; Weber, S., *Analytical Chemistry* **2010,** *82* (15), 6370-6376.
68. Jaquins-Gerstl, A.; Shu, Z.; Zhang, J.; Liu, Y.; Weber, S. G.; Michael, A. C., *Analytical Chemistry* **2011,** *83* (20), 7662-7667.
69. Nicholson, C., *Reports on progress in Physics* **2001,** *64*, 815.
70. Jefferys, J.; Deans, J.; Bikson, M., *Radiation protection dosimetry* **2003,** *106* (4), 321-323.
71. Chan, C.; Hounsgaard, J.; Nicholson, C., *Journal of Physiology* **1988,** *402* (1), 751-771.
72. Gluckman, B.; Neel, E.; Netoff, T., *Journal of neurophysiology* **1996,** *76* (6), 4202-4205.
73. Bikson, M.; Inoue, M.; Akiyama, H., *Journal of Physiology* **2004,** *557* (1), 175-190.
74. Datta, A.; Baker, J. M.; Bikson, M.; Fridriksson, J., *Brain Stimulation* **2011,** *4* (3), 169-174.
75. Tyzio, R.; Ivanov, A.; Bernard, C.; Holmes Gregory, L.; Ben-Ari, Y.; Khazipov, R., *Journal of neurophysiology* **2003,** *90* (5), 2964-72.
76. Hallberg, M.; Nyberg, F., *Current Protein and Peptide Science* **2003,** *4* (1), 31-44.
77. Benveniste, H., *Anesthesiology* **2009,** *110* (2), 422-425.
78. Dirnagl, U.; Simon, R. P.; Hallenbeck, J. M., *Trends in Neuroscience* **2003,** *26* (5), 248-254.
79. Murry, C. E.; Jennings, R. B.; Reimer, K. A., *Circulation* **1986,** *74* (5), 1124-36.

80. Marber, M. S.; Latchman, D. S.; Walker, J. M.; Yellon, D. M., *Circulation* **1993,** *88* (3), 1264-72.
81. Maulik, N.; Goswami, S.; Galang, N.; Das, D. K., *FEBS Letters* **1999,** *443* (3), 331-336.
82. Bartfai, T.; Hokfelt, T.; Langel, U., *Critical Reviews in Neurobiology* **1993,** *7* (3-4), 229-74.
83. Counts, S.; McGuire, S.; Sortwell, C.; Crawley, J.; Collier, T.; Mufson, E., *Journal of Neurochemistry* **2002,** *83* (2), 442-451.
84. Hawes, J., J; Narasimhaiah, R.; Picciotto Marina, R., *European Journal of Neuroscience* **2006,** *23* (11), 2937-46.
85. Hawes, J.; Brunzell, D.; Narasimhaiah, R.; Langel, U.; Wynick, D.; Picciotto, M., *Neuropsychopharmacology* **2008,** *33* (8), 1864-1873.
86. Jacoby, A.; Hort, Y.; Constantinescu, G.; Shine, J.; Iismaa, T., *Molecular Brain Research* **2002,** *107* (2), 195-200.
87. Kokaia, M., *Advances in Behavioral Biology* **2005,** *55* (Kindling 6), 219-227.
88. Lang, R.; Gundlach, A.; Kofler, B., *Pharmacology and Therapeutics* **2007,** *115* (2), 177-207.
89. Elliott-Hunt, C.; Pope, R.; Vanderplank, P.; Wynick, D., *Journal of Neurochemistry* **2007,** *100* (3), 780-789.
90. Elliott-Hunt, C.; Marsh, B.; Bacon, A.; Pope, R.; Vanderplank, P.; Wynick, D., *Proceedings of the National Academy of Science, U. S. A.* **2004,** *101* (14), 5105-5110.
91. Bedecs, K.; Langel, U.; Bartfai, T., *Neuropeptides* **1995,** *29* (3), 137-43.
92. Land, T.; Langel, U.; Bartfai, T., *Brain Research* **1991,** *558* (2), 245-50.
93. Bedecs, K.; Berthold, M.; Bartfai, T., *The international journal of biochemistry & cell biology* **1995,** *27* (4), 337-49.
94. Jureus, A.; Lindgren, M.; Langel, U.; Bartfai, T., *Neuropeptides* **1998,** *32* (5), 453-460.
95. Wang, S.; Clemmons, A.; Strader, C.; Bayne, M., *Biochemistry* **1998,** *37* (26), 9528-9535.
96. Wang, S.; He, C.; Hashemi, T.; Bayne, M., *Journal of Biological Chemistry* **1997,** *272* (51), 31949-31952.
97. Fisone, G.; Langel, U.; Carlquist, M.; Bergman, T.; Consolo, S.; Hoekfelt, T.; Unden, A.; Andell, S.; Bartfai, T., *European Journal of Biochemistry* **1989,** *181* (1), 269-76.
98. Pirondi, S.; Fernandez, M.; Schmidt, R.; Hokfelt, T.; Giardino, L.; Calza, L., *Journal of Neurochemistry* **2005,** *95* (3), 821-833.
99. Wang, S.; Hashemi, T.; Fried, S.; Clemmons, A.; Hawes, B., *Biochemistry* **1998,** *37* (19), 6711-7.
100. Wittau, N.; Grosse, R.; Kalkbrenner, F.; Gohla, A.; Schultz, G.; Gudermann, T., *Oncogene* **2000,** *19* (37), 4199-4209.
101. Zhang, D.; Yang, C., *Zhongguo Shengwu Zhipinxue Zazhi* **2012,** *25* (1), 126-128.
102. Shen, P.-J.; Larm Jari, A.; Gundlach Andrew, L., *European Journal of Neuroscience* **2003,** *18* (6), 1362-76.
103. Hwang, I.; Yoo, K.-Y.; Kim, D.; Do, S.-G.; Oh, Y.-S.; Kang, T.-C.; Han, B.; Kim, J.; Won, M., *Brain Research* **2004,** *1023* (2), 193-199.
104. Lee, H.; Hwang, I.; Kim, D.; Kim, J.; Kim, C.; Lim, B.; Kang, T.-C.; Bang, K.; Seong, N.; Lee, H.; Kim, J.; Won, M., *Experimental Animals* **2005,** *54* (1), 21-27.
105. Hui, K.-S., *Neurochemical Research* **2007,** *32* (12), 2062-2071.
106. Scales, N.; Tait, R. N., *Journal of Chemical Physics* **2006,** *125*, 094714.

107. Arifin, D. Y.; Lee, K. Y. T.; Wang, C.-H.; Smith, K. A., *Pharmaceutical Research* **2009,** *26* (10), 2289-2302.